Phil. Trans. R. Soc. Lond. A **308**, 199–218 (1982) [199]
Printed in Great Britain

ON DOMINATING ELASTICO-VISCOUS RESPONSE IN SOME COMPLEX FLOWS

BY K. WALTERS AND M. F. WEBSTER
Department of Applied Mathematics, University College of Wales, Aberystwyth SY23 3BZ, U.K.

(*Communicated by Sir Granville Beynon, F.R.S. – Received* 13 *November* 1981)

[Plates 1–12]

CONTENTS

A laser flow-visualization technique is used to study the behaviour of Newtonian and non-Newtonian elastic liquids in complex flows involving abrupt changes in geometry. Particular attention is paid to those situations where dramatic elastico-viscous effects are in evidence and the flow characteristics for non-Newtonian liquids are *qualitatively* different from those for Newtonian liquids. Consideration is also given to the effect of 'rounding' sharp re-entrant corners.

Two basic types of geometry are studied in detail. The first is the so-called combined mixing-and-separating flow geometry introduced in an earlier study (Cochrane *et al.* 1981), while the second includes both planar and circular contractions.

Attempts to simulate numerically the observed flows are very satisfactory in the Newtonian case, but the elastico-viscous simulations can do no more than indicate trends in the right direction.

1. Introduction

In a previous paper (Cochrane *et al.* 1981) referred to in the following as part 1 for convenience, experimental results were presented that showed how the flow characteristics of Newtonian and non-Newtonian elastic liquids could be markedly different when such liquids are made to flow in complex geometries. Most of the geometries involved re-entrant corners and similar abrupt changes and one of the major interests concerned the interaction between these abrupt changes and the fluid memory possessed by the non-Newtonian test liquids. The study was facilitated by the use of the so-called Boger (1977/8) fluid as the solution in that it does not display the dramatic drop in viscosity with shear rate so characteristic of most polymer systems. The viscosity is in fact reasonably constant over a significant shear-rate range and it is therefore possible to define a meaningful Reynolds number R, which makes the comparison of flow characteristics for Newtonian and non-Newtonian liquids a reasonable proposition. Such a comparison is far more difficult when the non-Newtonian test liquids are 'shear-thinning'.

A further dimensionless *elasticity* number W was required for the Boger fluids and the experimental results were then compared by investigating the effect of varying W at a series of fixed Reynolds numbers. One noticeable feature in the experiments was the opposing influences of fluid inertia and fluid elasticity, in the sense that changes in the flow field brought about by increasing the Reynolds number R could often be counteracted by increasing the elasticity number W. Another feature worthy of comment was that the elastic liquids responded to geometrical asymmetries in a dramatically different manner from their Newtonian counterparts in that slight asymmetries in the geometry could result in major asymmetries in the flow field for the Boger fluids in marked contrast to the Newtonian situation.

Attempts were made to simulate numerically the observed flows, for both Newtonian and non-Newtonian cases, by using finite-difference techniques. In the former case, the agreement between theory and experiment was excellent. In the non-Newtonian case, the observed *trends* with increasing W were simulated but the numerical predictions were invariably hampered by instability problems as the value of W approached values that were relevant to the experimental programme. Such problems are now commonplace in all studies involving the numerical simulation of non-Newtonian flows (Crochet *et al.* 1983) and present the major challenge in future developments.

In the present paper, we give further consideration to the general study of Newtonian and non-Newtonian flows in complex geometries and the possibility of numerical predictions. Particular attention is paid to any dramatic changes in flow characteristics that can be directly associated with fluid elasticity effects. Special consideration is given to two particular types of geometry. The first, in §4, concerns the so-called combined mixing-and-separating geometry discussed in part 1. The second, in §5, involves both planar and circular contractions.

2. Experimental

(*a*) *Apparatus*

The apparatus was a simple adaptation of that used in part 1. The flow was created by a peristaltic pump and use was made of smoothing bottles to create a steady flow. The flow rate used in the calculation of the characteristic numbers R and W was determined by a simple catch-and-weigh technique and, for the range of viscosities employed in the present study, we were limited to Reynolds numbers below 40.

The geometries employed in the test section are shown schematically in figure 1. For the combined mixing-and-separating geometries 1*a–c*, the inserts DA and BG were made of aluminium and were 0.127 mm thick. As the total channel width was 10 mm, we felt that the test section approximated to a sufficient degree to one in which the inserts could be regarded as having zero thickness with 360° corners at A and B. This is relevant to the numerical simulation discussed in § 3.

Geometries 1*a–c* had a depth of 20 mm. The flow directions are given by the unlabelled arrows and their size gives an indication of the *relative* strengths of the flow in each arm. However, usually we have attempted to generate flows of equal magnitude in all the arms.

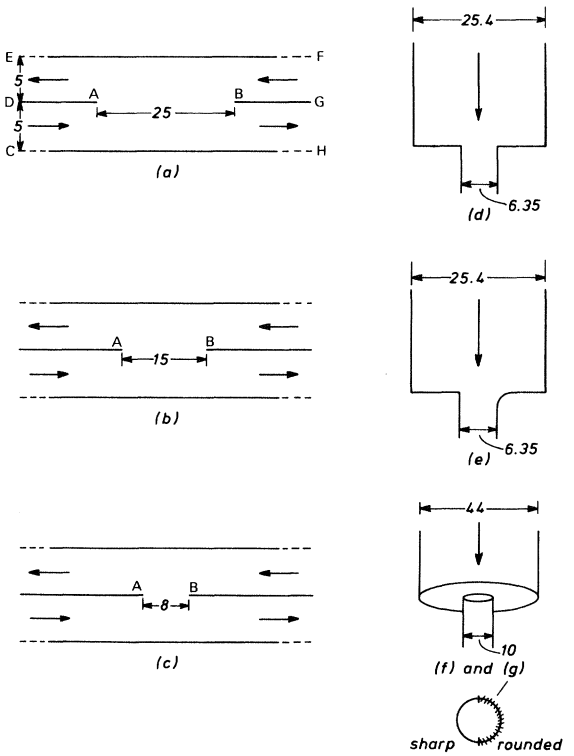

FIGURE 1. Schematic diagram of experimental geometries; all dimensions are in millimetres.

In many respects, geometries 1*a–c* are similar to the combined mixing-and-separating geometries reported in part 1, except that in the earlier experiments the inserts had a thickness of 1 mm in a channel of width 11 mm, and the ends were considered as consisting of two 90° re-entrant corners. By employing the modified geometries 1*a–c*, we have been able to follow up the experiments discussed in part 1 and at the same time consider any new features arising from the change of conditions at the ends of the inserted arms.

Geometry 1*d* is a conventional 4 : 1 planar contraction of depth 25.4 mm, while geometry 1*e* differs from 1*d* in only one important respect: one of the re-entrant corners has been rounded to a radius of curvature h, where $4h$ is the width of the narrow channel.

Geometry 1*f* is also a conventional contraction but this time in a circular geometry with a contraction ratio of 4.4 : 1. For reasons that will become apparent later, we also modified this geometry by rounding part of the exit lip (figure 1*g*). Specifically, 180° of the exit lip was left

untouched and the remaining 180° was rounded to a radius of curvature h, where $10h$ is the diameter of the narrow capillary (geometric discontinuities arose at the intersections of the sharp and rounded parts of the exit lip).

Finally we remark that, in all cases, the geometries were of sufficient length to ensure that 'fully developed' flow conditions existed at both entrance and exit. This feature has been omitted from figure 1 for convenience of presentation.

Interest in the present study centres on flow visualization and we have resorted to a modified version of the laser technique introduced in part 1. The relevant set-up for the combined mixing-and-separating geometries is shown in figure 2.

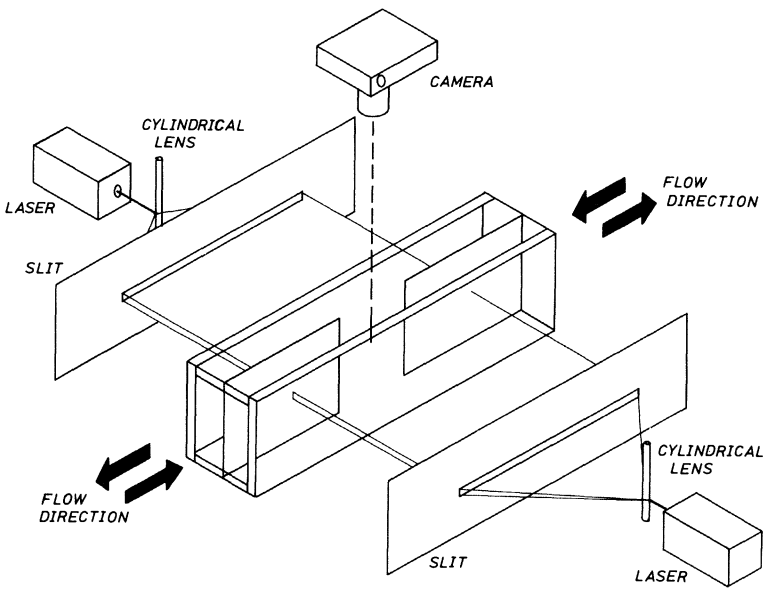

FIGURE 2. Flow-visualization apparatus.

Two 5 mW helium–neon lasers (Spectra Physics Model 120) had to be employed because of the metal barriers. These were spread into narrow sheets of light by means of cylindrical lenses. These were then photographed with a conventional camera mounted vertically above the test section. The principle of the method is simple. Small particles, contained in and moving with the fluid, scatter light on entering the measuring plane. When developed, the photographs of the streamlines give a visual representation of the flow. In the present study, we used polyvinyl chloride particles with a density of 1.4 g cm^{-3} and found it convenient to use 2 g of powder in every 10 l of liquid.

For geometries 1 *d–g* only one laser was required in the experiments.

(*b*) *Test liquids*

The Newtonian liquids used in the experimental programme were mixtures of water and maltose syrup (C.P.C., U.K.). The non-Newtonian liquids were polymer solutions, most of which were dilute solutions of polyacrylamide (N100 grade supplied by Cyanamid of Great Britain) in a mixture of water and maltose syrup. These Boger (1977/8) fluids were highly elastic and yet possessed a reasonably constant viscosity (Walters 1980).

The test liquids were characterized on a Weissenberg Rheogoniometer, R16 model. In a steady simple shear flow with Cartesian velocity components given by†

$$v^1 = qx^2, \quad v^2 = v^3 = 0, \tag{1}$$

where q is a constant shear rate, the corresponding stress distribution for a rheologically complex fluid can be written in the form

$$\left.\begin{aligned} p^{12} &= \tau(q) = q\eta(q), \\ p^{11}-p^{22} &= \nu_1(q), \quad p^{22}-p^{33} = \nu_2(q), \end{aligned}\right\} \tag{2}$$

where τ is the shear stress and ν_1 and ν_2 are the first and second normal stress differences, respectively; η is called the apparent viscosity.

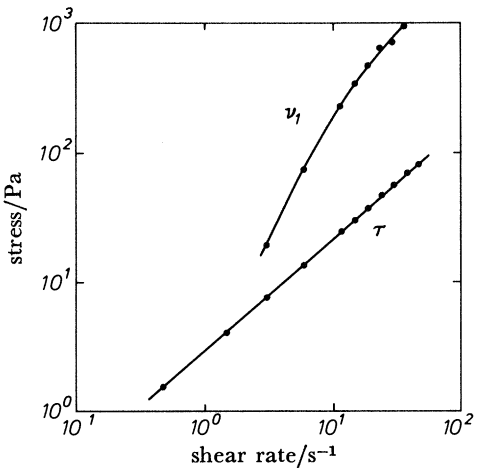

FIGURE 3. Rheometric data for liquid B10.

The Weissenberg Rheogoniometer, in normal operation, allows determination of τ (and hence η) and ν_1 (Walters 1975). For a Newtonian liquid, ν_1 and ν_2 are zero and η is the constant viscosity coefficient. For the Boger fluids, the stress distribution can be approximated by

$$\left.\begin{aligned} \tau &= \eta_0 q, \\ \nu_1 &= 2\eta_0 \lambda q^2, \end{aligned}\right\} \tag{3}$$

where η_0 and λ are constants. λ is a characteristic relaxation time, which can be viewed as a measure of fluid memory. There is some evidence to support the contention that $\nu_2 \approx 0$ for Boger fluids (Keentok *et al.* 1980).

Figure 3 shows typical rheometrical results obtained for one of the Boger fluids used in the present study. From this figure, it is not difficult to deduce approximate values of η_0 and λ from (3). All the relevant parameters thus obtained for the various Boger test fluids, together with the corresponding densities ρ, are given in table 1.

For reasons that will become apparent in § 5, it was also of interest to do experiments on a more conventional elastic test fluid, an aqueous solution of polyacrylamide (liquid C1). The relevant

† We use standard tensor notation. Covariant indices are written as subscripts, contravariant indices as superscripts, and the usual convention for repeated indices is assumed.

rheometrical data for liquid C1 are given in figure 4, together with the associated apparent viscosity. Substantial shear-thinning behaviour is clearly evident.

All the experiments were carried out at 20 °C.

TABLE 1. ESTIMATED DENSITY, VISCOSITY AND RELAXATION TIME FOR BOGER LIQUIDS

liquid	$\rho/(\mathrm{g\ cm^{-3}})$	$\eta_0/(\mathrm{Pa\ s})$	λ/s
B5	1.3	0.2	0.036
B6	1.3	0.1	0.007
B7	1.3	0.15	0.011
B8	1.3	1.6	0.35
B9	1.3	0.8	0.035
B10	1.3	2.25	0.4

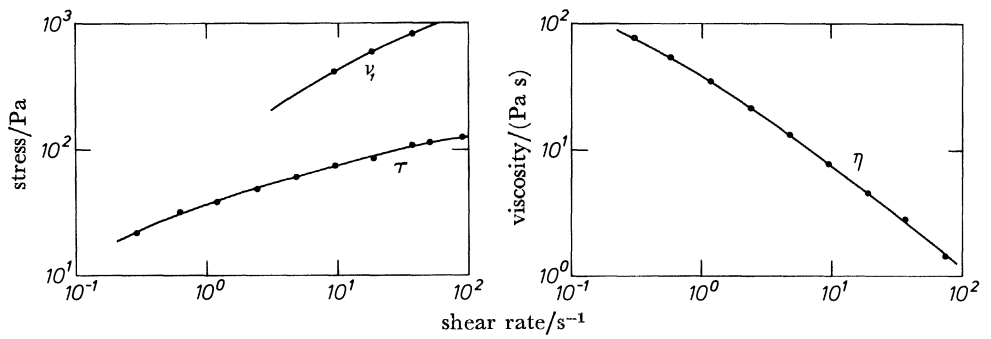

FIGURE 4. Rheometric data for liquid C1.

For the Newtonian and Boger test fluids, it is convenient to define two dimensionless numbers. The first, the Reynolds number R is given by

$$R = \rho \bar{U} L/\eta_0, \tag{4}$$

where $\bar{U}$ is the mean velocity and L is a characteristic length. The second, an elasticity number W, is defined by

$$W = \lambda \bar{U}/L. \tag{5}$$

For combined mixing-and-separating flow, $\bar{U}$ is taken as the flow rate into one of the inlet arms divided by the appropriate cross-sectional area and L is taken as the inlet channel width (5 mm). In the contraction flows, $\bar{U}$ is taken as the flow rate divided by the upstream cross-sectional area and the characteristic length L is the upstream channel width for the planar geometry and the upstream radius for the circular contraction.

3. NUMERICAL SIMULATION

The search for dramatic experimental elastico-viscous effects in complex flows is one of our two main concerns in the present study. The other is the possibility of their theoretical prediction. This exercise necessarily involves the application of advanced numerical techniques and a basic consideration of the Navier–Stokes equations for Newtonian flow, prior to the more difficult study of elastico-viscous effects. The numerical simulation of Newtonian flow has not been a major problem and we shall see that the agreement between theory and experiment in

this regard is very satisfactory. Unfortunately, the same cannot be said concerning elastico-viscous flow and the most that can be hoped for at the present time is a qualitative indication of observed trends, especially when the experimental results show dramatic differences between Newtonian and non-Newtonian flow. The basic problems were highlighted in part 1. They are:

(i) the choice of the most appropriate rheological equations of state;

(ii) the correct numerical strategy of handling re-entrant corners;

(iii) the extension of numerical algorithms to realistic values of W, where interesting changes in flow characteristics are observed in the experimental study.

In part 1, we indicated that (i) was not a major concern at the present time, especially for the Boger fluids, and it was argued that any one of a number of implicit differential or explicit integral equations of the Oldroyd–Maxwell type could be used without invoking undue criticism. The so-called upper-convected Maxwell model was employed in much of the work of part 1. This had equations of state given by

$$p_{ik} = -p\delta_{ik} + p'_{ik}, \tag{6}$$

$$p'^{ik} + \lambda \frac{\mathfrak{d}p'^{ik}}{\mathfrak{d}t} = 2\eta_0 e^{(1)ik}, \tag{7}$$

where δ_{ik} is the Kronecker delta, p is an isotropic pressure, $e^{(1)ik}$ is the (first) rate-of-strain tensor and $\mathfrak{d}/\mathfrak{d}t$ is the convected time derivative introduced by Oldroyd (1950).

For the steady simple shear flow given by (1), the relevant stress distribution for the model represented by equation (7) is

$$p^{12} = \eta_0 q, \quad p^{11} - p^{22} = 2\eta_0 \lambda q^2, \quad p^{22} - p^{33} = 0, \tag{8}$$

so that the model predicts a constant viscosity η_0 and a quadratic first normal stress difference ν_1, in reasonable agreement with the experimental data obtained for the Boger test fluids. To introduce the facility of a variable viscosity behaviour (which is certainly required in any numerical simulation involving liquid C1 for example) one can modify (7) by introducing two further time constants λ_2 and μ_0 to yield

$$p'^{ik} + \lambda_1 \frac{\mathfrak{d}}{\mathfrak{d}t} p'^{ik} + \mu_0 p'^{j} e^{(1)ik} = 2\eta_0 \left[1 + \lambda_2 \frac{\mathfrak{d}}{\mathfrak{d}t}\right] e^{(1)ik}, \tag{9}$$

for which the appropriate simple shear stress p^{12} is now given by

$$p^{12} = \eta_0 q \left[\frac{1 + \lambda_2 \mu_0 q^2}{1 + \lambda_1 \mu_0 q^2}\right], \tag{10}$$

and, if $\lambda_1 > \lambda_2$, the apparent viscosity function $\eta(q)$ falls monotonically from a low shear value η_0 to a so-called 'second Newtonian' value $\eta_0 \lambda_2/\lambda_1$.† In part 1, we did not imply that models (7) and (9) were the only possible choices but used them as relatively simple examples of the many possibilities open to us. Even the use of these models requires techniques that are significantly more sophisticated than those employed in any study of the Navier–Stokes equations. One obvious example is the fact that since (7) and (9) are implicit in the stress tensor, the stress components must be considered as dependent variables along with the stream function ϕ and vorticity ω.

The second problem concerning conditions near a re-entrant corner has not yet received the

† For model (9), W is given by $W = (\lambda_1 - \lambda_2)\bar{U}/L$, and the time constants λ_2 and μ_0 are non-dimensionalized by multiplying by $\bar{U}/L$.

detailed attention it deserves in non-Newtonian fluid mechanics and there has been a tendency to simply ignore it. The arguments appeal to the adequacies of a rounding-of-the-corner approach, which must be valid if the grid is fine enough. There is clearly substance in this argument, but for the numerical analyst a pragmatic choice of an appropriate mesh near the corner must be made which in practice will never be completely adequate. For this reason, we decided to make a detailed experimental study of the effect of a relatively coarse rounding of the corner in two popular complex flows: planar and circular contraction flows. We suggest that the rounding related to figure 1*e, g* would be regarded as realistic in many numerical studies, especially those by finite-difference techniques. The experimental programme is therefore designed in part to answer one important question: What effect does the rounding of the corner have on flow characteristics? If the answer is that very little change is evident by rounding the corner, then we have been wrong to emphasize the need for a detailed study of conditions near re-entrant corners. However, if flow characteristics are manifestly affected by the precise shape of the corner, it behoves those working in the field to give serious attention to the difficult problem of specifying re-entrant corner conditions in the case of rheologically complex fluids. (It must be emphasized that the problem is basically restricted to such fluids, since the Newtonian situation has already been essentially resolved (Moffatt 1964; Holstein & Paddon 1981; Cochrane *et al.* 1982).)

The third problem concerning the present inability to simulate flows at high values of the elasticity number W is by far the most troublesome and little progress has been made in problems where experimental results show dramatic elastico-viscous effects. Under these conditions, the most that one can hope for at the present time is an encouraging indication of trends.

We now concentrate on the mixing-and-separating flow geometry (figure 1*a*) and model (7). Rectangular Cartesian coordinates x^i are introduced, with origin at C and CH given by $x^2 = 0$ and DG by $x^2 = 1$, and the physical variables are non-dimensionalized in the following manner:

$$\left.\begin{aligned} x^{1*} &= \frac{x^1}{L}, \quad x^{2*} = \frac{x^2}{L}, \quad v^{1*} = \frac{v^1}{\bar{U}}, \quad v^{2*} = \frac{v^2}{\bar{U}}, \\ p'^{ik*} &= \frac{p'^{ik}L}{\eta_0 \bar{U}}. \end{aligned}\right\} \tag{11}$$

The governing equations for a steady two-dimensional flow of the model represented by equation (7) are then

$$\omega = -\left(\frac{\partial^2\phi}{\partial(x^1)^2} + \frac{\partial^2\phi}{\partial(x^2)^2}\right), \tag{12}$$

$$R\left[\frac{\partial\phi}{\partial x^1}\frac{\partial\omega}{\partial x^2} - \frac{\partial\phi}{\partial x^2}\frac{\partial\omega}{\partial x^1}\right] = \frac{\partial^2 p'^{11}}{\partial x^1 \partial x^2} + \frac{\partial^2 p'^{12}}{\partial(x^2)^2} - \frac{\partial^2 p'^{12}}{\partial(x^1)^2} - \frac{\partial^2 p'^{22}}{\partial x^1 \partial x^2}, \tag{13}$$

$$p'^{11}\left[1 - 2W\frac{\partial v^1}{\partial x^1}\right] + W\left[v^1\frac{\partial p'^{11}}{\partial x^1} + v^2\frac{\partial p'^{11}}{\partial x^2}\right] - 2Wp'^{12}\frac{\partial v^1}{\partial x^2} = 2\frac{\partial v^1}{\partial x^1}, \tag{14}$$

$$p'^{22}\left[1 - 2W\frac{\partial v^2}{\partial x^2}\right] + W\left[v^1\frac{\partial p'^{22}}{\partial x^1} + v^2\frac{\partial p'^{22}}{\partial x^2}\right] - 2Wp'^{12}\frac{\partial v^2}{\partial x^1} = 2\frac{\partial v^2}{\partial x^2}, \tag{15}$$

$$-Wp'^{11}\frac{\partial v^2}{\partial x^1} - Wp'^{22}\frac{\partial v^1}{\partial x^2} + W\left[v^1\frac{\partial p'^{12}}{\partial x^1} + v^2\frac{\partial p'^{12}}{\partial x^2}\right] + p'^{12} = \left(\frac{\partial v^1}{\partial x^2} + \frac{\partial v^2}{\partial x^1}\right), \tag{16}$$

with $v^1 = \partial\phi/\partial x^2$, $v^2 = -\partial\phi/\partial x^1$, where ω and ϕ are the non-dimensional vorticity and stream function, respectively, and we have dropped the star notation for convenience of presentation. Equations (12)–(16) are five equations in the five unknowns p'^{11}, p'^{22}, p'^{12}, ω and ϕ.

The boundary conditions are provided by the no-slip condition $v^1 = v^2 = 0$ over solid boundaries and fully developed Poiseuille flow conditions over the inlets CD and FG and the outlets DE and GH. Over CD, for example, we have the velocity profile

$$v^1 = 6x^2(1-x^2), \quad v^2 = 0, \quad 0 \leqslant x^2 \leqslant 1, \tag{17}$$

or, equivalently,

$$\phi = (x^2)^2[3-2x^2], \quad 0 \leqslant x^2 \leqslant 1, \tag{18}$$

and the mean flow rate across CD, as given by $\phi_D - \phi_C$, is unity as required.

The boundary conditions on the remaining stress and vorticity variables are now easily obtained over CD from equations (12), (14)–(16) by using (17) or (18).

Our overall numerical strategy follows closely that described by Davies *et al.* (1979) as modified by Cochrane *et al.* (1981, 1982). It is a square-mesh finite-difference representation that involves the decoupling of the nonlinear system of governing equations and the solving of the resulting linear systems by a successive-over-relaxation (S.O.R.) iterative technique. Available computer store and time allowed approximately 4000 grid points at maximum in the flow geometry.

By using a method of inner and outer iterations, the rheological equations of state and the stress equations of motion were solved as three decoupled systems of equations in the stress components, ω and ϕ. The method is described in detail by Davies *et al.* (1979) but particular attention must now be paid to the new corner strategies involved in the present work.

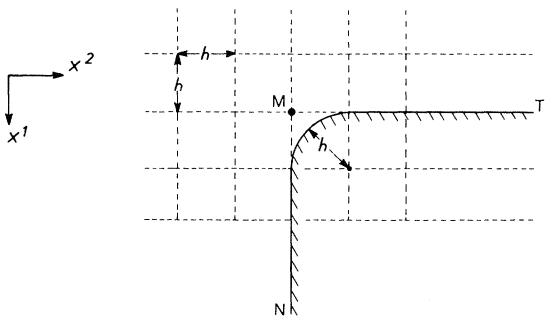

FIGURE 5. The relation of the numerical grid to the rounded corner geometry in planar contraction geometry (1*e*).

The treatment of the thin inserted partitions associated with geometries 1*a–c* follows closely the multi-valued boundary variable approach suggested by Roache (1972) used in conjunction with a Kawaguti (1965) corner technique. The stress components and vorticity are taken to be double-valued away from the leading edges and triple-valued at A and B. The choice of the boundary value adopted for each of these variables is then made, depending on the particular direction of reference involved. For example, the choice at corner point A would depend on whether the point is reached along the top or bottom face of DA or from the edge direction BA.

The sharp re-entrant corner technique required for the planar contraction flow geometry of figure 1*d* to supply numerical estimates of the stress components and the vorticity is the one that we have found to be the most acceptable of the various *simple* corner strategies available, namely an extension of that proposed by Kawaguti (1965) and discussed in detail by Cochrane *et al.* (1982).

The asymmetrical planar contraction geometry (figure 1*e*) involves one sharp re-entrant corner and one rounded corner. The sharp corner is handled in the same way as the corners in

the symmetrical geometry 1*d*. For the rounded corner, the point M in figure 5 now becomes an *internal* grid point and must be treated as such numerically. This involves removing the no-slip condition at M and iterating for the variables $\phi, \omega, p'^{11}, p'^{12}$ and p'^{22} at this point. The process proves to be fairly straightforward owing to the choice of mesh dimensions and rounding (cf. figure 5). A potential complication *does* arise in the calculation of second-order mixed derivatives at M. This is overcome by consideration of the half-stepsize grid and an averaging approximation about M (cf. Holstein 1981).

4. Combined mixing-and-separating flow

(*a*) *Introduction*

In part 1, we considered a combined mixing-and-separating flow with arms DA and BG of thickness 1 mm, which could not be neglected in the numerical simulation. The ends were considered as two re-entrant corners with one grid spacing between them. It was predicted numerically and confirmed experimentally that some of the flow was of a *unidirectional* type with fluid flowing from the entry CD to the exit GH and similarly from FG to DE, while some was of a *reversed* type flowing from CD to DE and FG to GH. Over the range of conditions studied, the amount of fluid flowing in a unidirectional fashion increased in relative terms as the elasticity parameter W increased. No attempt was made to study the corresponding effect of increasing the Reynolds number R.

Making the gap AB wider tended to encourage reversed flow and it was possible to choose conditions for which all the flow was of the reversed kind.

The combined mixing-and-separating flow studied in the present work differed from that of part 1 in that the inserts were considered sufficiently thin to have negligible thickness and 360° corners at A and B. The general features of the flow, both predicted and observed, were, not surprisingly, very similar to those found in part 1. Additionally we have been able to study new situations where quite dramatic changes with geometry, inertia and elasticity have been observed, and in some instances predicted as well.

(*b*) *Wide-gap geometry*

We consider first the wide-gap geometry of figure 1*a*. Figure 6 contains numerical simulations for a Newtonian fluid with increasing R values, the numbers on the various simulation curves corresponding to non-dimensional stream function ϕ values. The effect of elasticity on the flow is shown in figure 7, which contains simulations for non-zero values of W.

No unidirectional flow was predicted for any cases within the scope of the numerical program when the flow rates in the arms are all equal. Increasing the Reynolds number has the effect of increasing the size and strength of the central vortex, which ultimately divides into two vortices at high values of R. Introducing non-zero values of W has no dramatic effect on flow characteristics, but increased strength of the central vortex over the Newtonian equivalent is evident.

The type of streamline patterns to be expected when the balance of flow in the various arms is disturbed is shown in figure 8, the length of the arrows being an indication of the relative strength of the flow in each arm.

In the experimental programme, it was very difficult to control with sufficient accuracy the flow rate in the various arms and, in the wide-gap geometry, the streamline characteristics were very sensitive to small changes in the flow balance. However, figure 9, plate 1, does contain

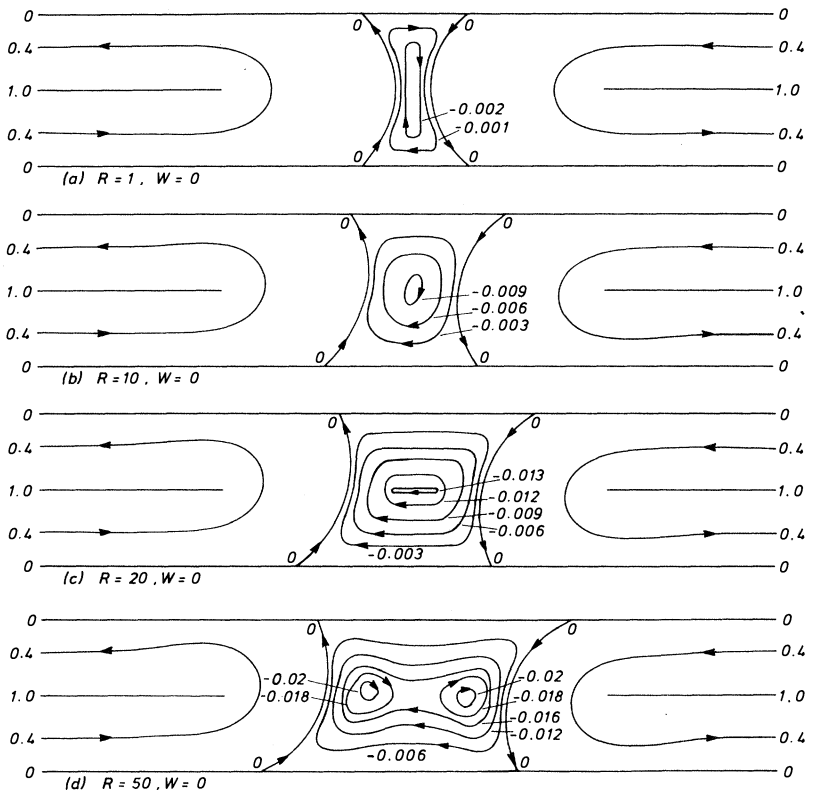

FIGURE 6. Numerical simulation for a Newtonian fluid in the wide-gap geometry (1*a*); equal flow rates in all arms.

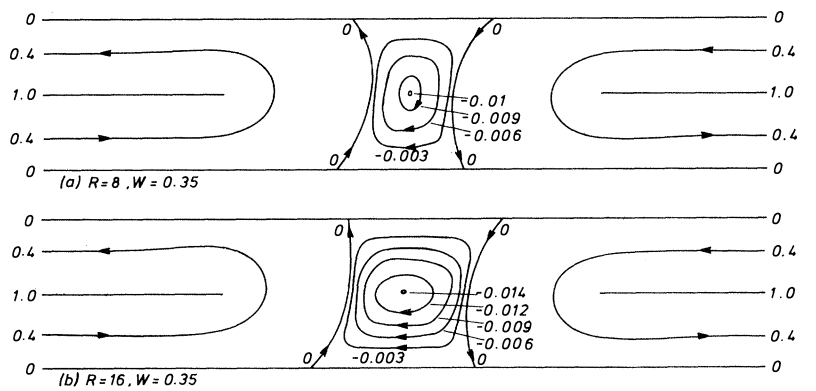

FIGURE 7. Numerical simulation for the Maxwell model (7) in the wide-gap geometry (1*a*); equal flow rates in all arms.

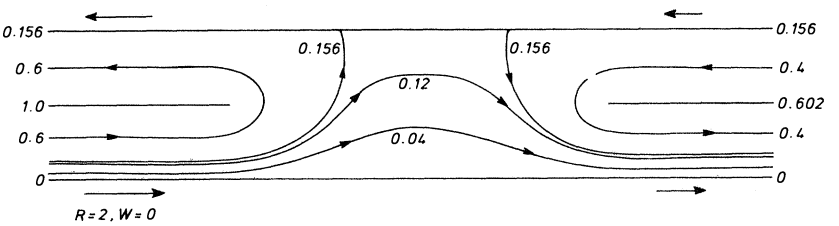

FIGURE 8. Numerical simulation for a Newtonian fluid in the wide-gap geometry (1*a*); relative flow rates indicated by lengths of arrows and Reynolds number based on flow conditions in lower left arm CD.

examples of reasonably successful photographic results for comparison with the numerical simulations given in figures 6–8.

The shadows cast by the two lasers provide an indication of the positioning of the partitions. The central vortex is too weak to be seen in figure 9*a* but it is discernible in figure 9*b*. An unstable flow in the central region becomes evident in the high Reynolds number elastico-viscous case (figure 9*c*). The unbalanced flow-rate case (figure 9*d*) is seen to be in very good agreement with the numerical prediction of figure 8.

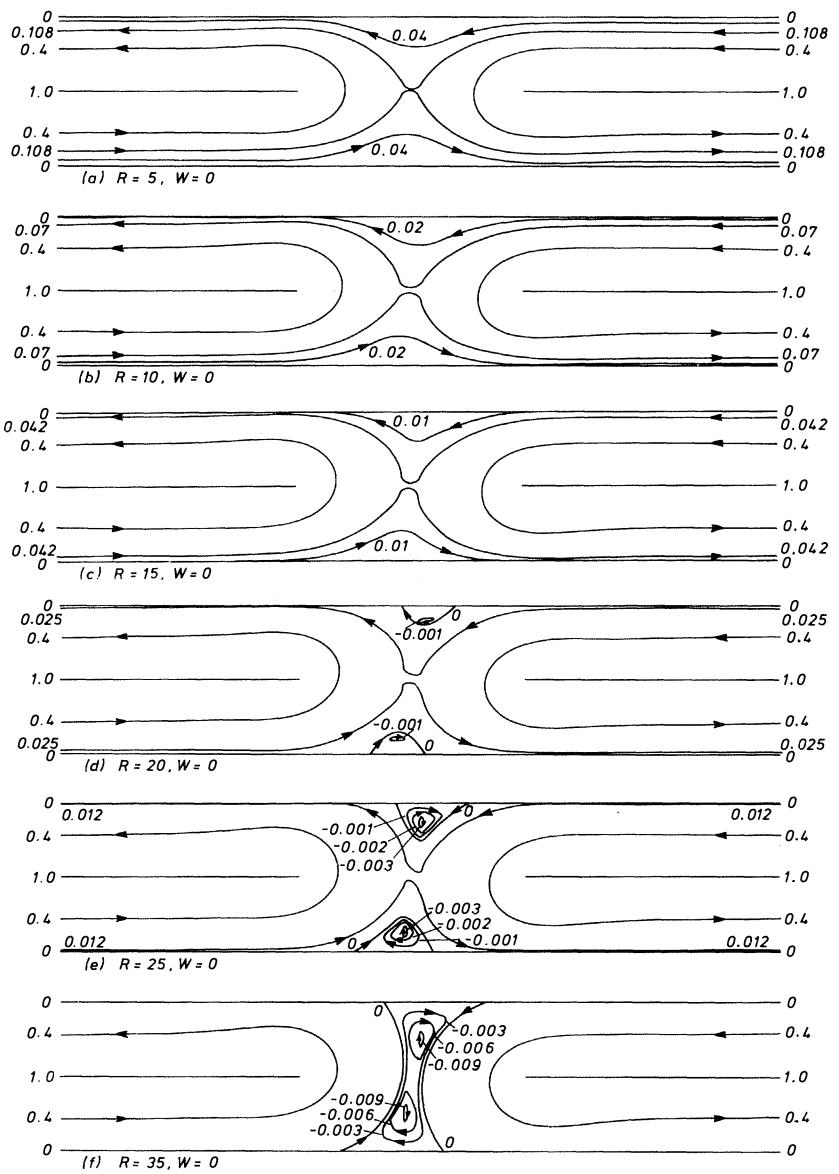

FIGURE 10. Numerical simulation for a Newtonian fluid in the medium-gap geometry (1*b*); equal flow rates in all arms.

(*c*) *Medium-gap geometry*

The medium-gap situation provides the most interesting effects of the three combined mixing-and-separating flow geometries considered. The relevant Newtonian simulations are given in figure 10. At low Reynolds numbers, the flow has the complete symmetry one would anticipate, but this is disturbed as inertial effects become evident. Further increases in R give rise to two recirculating vortices as shown in figures 10*d*, *e*. Of significant interest is the prediction that increasing Reynolds number does not give rise to an increased unidirectional flow. Indeed, the flow becomes of the completely reversed type!

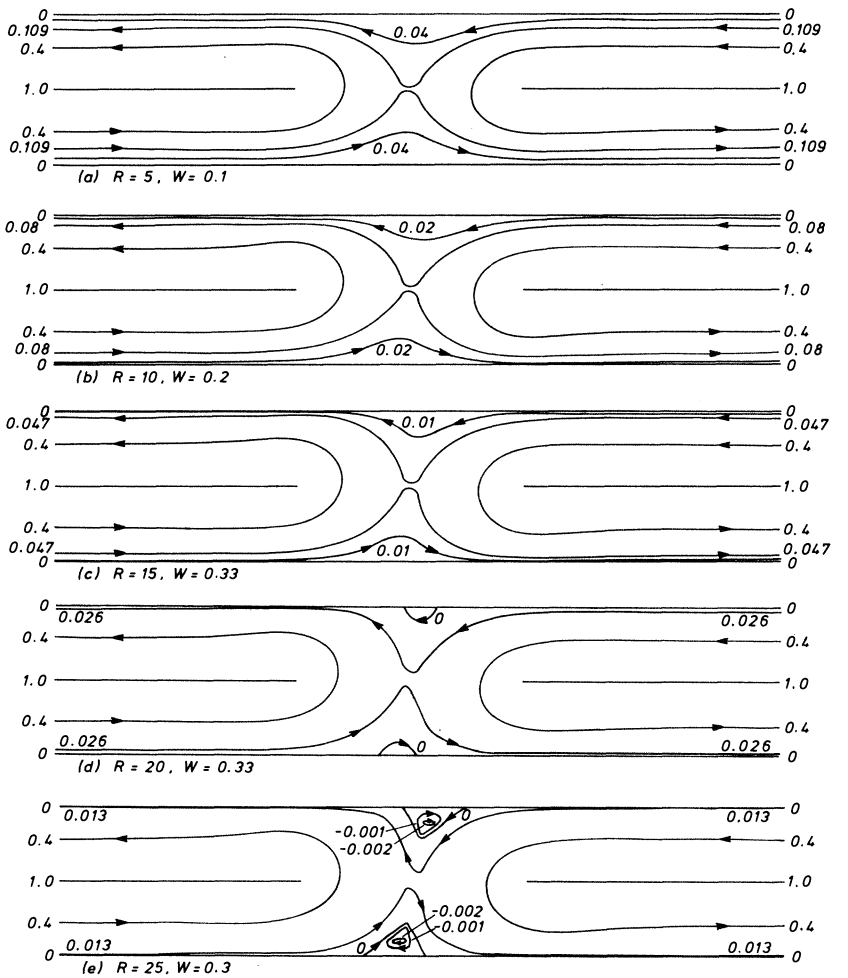

FIGURE 11. Numerical simulation for the Maxwell model (7) in the medium-gap geometry (1*b*); equal flow rates in all arms.

Over the range of conditions that we have been able to cover in the elastico-viscous case, there is a strong indication that fluid elasticity delays the move to reversed flow by encouraging more flow of the unidirectional type and the suppression of the strength of the recirculating vortices (see figure 11). However, it must be admitted that we have not been able to predict the dramatic experimental elastico-viscous effects that we shall now proceed to discuss.

Figure 12, plate 2, contains experimental results for the Newtonian fluid in the medium-gap case.† The combination of unidirectional and reversed flow, together with complete symmetry, is evident in the low Reynolds number cases, as is the disturbing effect of inertia in figure 12*c*. Two recirculating vortices are clearly in evidence in figures 12*d*, *e*, although it can be easily deduced that a three-dimensional effect is present at these high Reynolds numbers with the vortices essentially acting as sinks. At the same time, the complete absence of unidirectional flow and the general features of the flow are in dramatically good agreement with the numerical predictions given in figure 10.

In striking contrast is the situation with regard to the elastico-viscous Boger fluids. Here, increasing the Reynolds number results in relatively more unidirectional flow (figure 13, plate 3) and, by choosing conditions appropriately, it is possible to arrive at a situation where the flow is almost completely of the unidirectional type, except in the region very close to the partition barriers (see, for example, figure 13*e*). This preference for unidirectional flow, already hinted at in part 1, is a very dramatic demonstration of elastico-viscous behaviour. We have made numerous unsuccessful attempts to predict such behaviour by taking, for example, a completely unidirectional flow as our initial guess in the numerical algorithm or by employing model (9) in place of model (7). We have also attempted to use a numerical continuation process in the Reynolds number R as suggested by G. Richards (private communication). This involved using, as an initial guess, the solution for a low Reynolds number and a reasonably high value of W to obtain a series of numerical simulations for increasing R and fixed W. We found that this process allowed us to reach higher values of R and W than could be attained by employing a continuation process in W (for fixed R). However, there was still an upper bound on (R, W) above which the numerical process failed to converge, with the attainable value of W decreasing with increasing R.

Over most of the range, the numerical trend with increasing W is consistent in qualitative terms with the experimental results in that the proportion of the flow which is of the unidirectional type increases with W. Often, however, a notable exception to this occurs near the breakdown conditions where we found an abrupt and reasonably dramatic reversal of this trend. We feel that this should be viewed as being a part of the numerical breakdown process rather than as an indicator of an interesting change in flow characteristics.

Notwithstanding the above comments about the upper bound on (R, W) above which converged numerical solutions cannot be obtained, we remark with interest that some of the available simulations do cover the range where interesting effects are observed experimentally (cf. figures 11*c* and 13*c*). The fact that the numerical predictions are unable to match the dramatic experimental trends spotlights another, as yet unresolved, problem in the numerical simulation of non-Newtonian flow. Clearly predicting behaviour of the sort shown in figure 13*e* presents an outstanding challenge to computational fluid dynamicists.

(*d*) *Narrow-gap geometry*

In the narrow-gap geometry (figure 1*c*) we have predicted and observed (cf. figure 14 and figure 15, plate 4) a combination of unidirectional and reversed flow for Newtonian liquids, with the tendency for fluid elasticity to increase, in relative terms, the amount of unidirectional flow. The trend is again more evident in the experiments than in the numerical simulations.

† We now restrict attention to the balanced flow situation.

However, the flow characteristics do not have the dramatic features discussed in the last section for the medium-gap geometry.

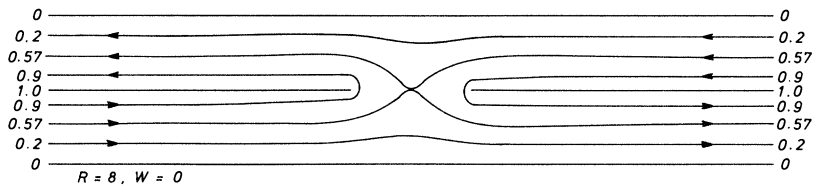

FIGURE 14. Numerical simulation for the narrow-gap geometry (1*c*): Newtonian; equal flow rates in all arms.

5. CONTRACTION FLOWS

(*a*) *Introduction*

Contraction flows, both planar and circular, have received very detailed study from a theoretical and an experimental standpoint and a number of recent reviews are available to assess the present situation (see, for example: White & Kondo 1977/8; Boger 1980, 1982).

It is generally accepted that the basic flow is of the type shown schematically in figure 16. Recirculating vortices are shown in the salient corners and an important length is the attachment length ST. So-called 'vortex growth' or 'vortex enhancement' is associated with a substantial increase in the length of ST.

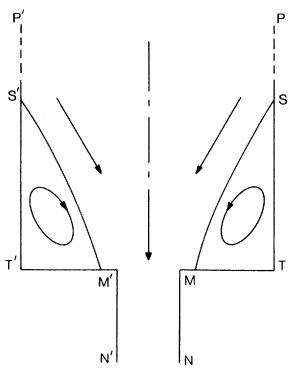

FIGURE 16. Schematic diagram of flow in the contraction geometry (1*d*).

Existing experimental evidence indicates that most elastico-viscous polymer systems exhibit significant vortex behaviour but that in some it is completely absent (cf. White & Kondo 1977/8). Some attempts have been made to associate such dramatic behavioural differences with the extensional viscosity characteristics of the polymer systems (cf. Cogswell 1972).

In circular contraction flows at very low Reynolds numbers the attachment length ST is often found to increase dramatically with the elasticity parameter W, and this vortex enhancement has provided one of the major challenges in numerical simulation of non-Newtonian fluid flow. To date, theoretical studies have indicated the existence of a small vortex region for Newtonian fluids which increases in size as W increases. However, these studies are totally inadequate to predict the large vortex enhancement observed experimentally for Boger fluids at very low Reynolds numbers (cf. Boger 1982).

When fluid inertia is significant, it has the effect of diminishing the size of the recirculating vortices. For a given test fluid and geometry a usual sequence with increasing flow rate would be an initial increase in vortex size followed by a slow decrease until finally an unstable flow ensues.

It has been usual to consider planar and circular contraction flows together and to assume that trends in one situation automatically apply to the other but there is some evidence to discourage this practice. For example, Black *et al.* (1975) offer some comments suggesting that smaller vortex regions may sometimes occur in planar contractions than in the corresponding circular cases.

Contraction flows, both planar and circular, clearly provide some of the most challenging current problems for theoretical and experimental rheologists. From the experimental standpoint, it would be useful to be able to correlate the appearance or absence of vortices with material properties and to understand the basic differences between planar and circular contraction flows. Theoretically such issues are also of interest, as is the related problem of vortex enhancement. Concerning the latter, the governing rheological equations have been varied by Crochet & Bezy (1980) to simulate accurately known rheometrical behaviour without leading to any significant improvement in the comparison between theory and experiment.

The precise influence of the re-entrant corners may provide another possible avenue of approach to study and it is hoped that the experiments described in this paper will cast some light on this suggestion.

(*b*) *Newtonian fluids*

As a basis for comparison, we refer first to experimental results for Newtonian fluids. Figure 17, plate 5, contains experimental data for three Reynolds numbers obtained for the rounded-corner planar geometry (figure 1*e*), the Reynolds numbers being based on conditions in either the upstream or downstream channel. There is evidence of weak recirculation in the salient corners, and the rounding of one of the re-entrant corners has the effect of reducing slightly the size of the associated recirculating region. This apart, there are no other flow characteristics that are worthy of special mention.

A corresponding numerical simulation for the Newtonian case is given in figure 18. There is clearly a reduction in the size of the vortex region associated with the rounded corner and, in this respect, there is satisfactory agreement between theory and experiment. The simulations also indicate that the influence of the rounded corner is felt as far afield as the central axis (although there is not sufficient resolution in the photographs to confirm this experimentally). We conclude that the coarse rounding of the corner under investigation would not be particularly appropriate as a replacement for a sharp re-entrant corner even in the Newtonian case.

Experimental results for Newtonian flow in the asymmetric *circular* contraction (figure 1*g*) are given in figure 19, plate 6. The geometry is aligned so that the part of the exit lip to the left is sharp while that to the right has been rounded as indicated in §2*a*. There is some evidence of recirculating regions in the salient corners, but these are not as apparent as for the planar geometry. It is difficult to assign any significant flow field changes to the changes in geometry at the exit lip. The experimental photographs in figure 19 are in satisfactory agreement with the published predictions of Viriyayathakorn & Caswell (1980).

(*c*) *Boger fluids*

Experiments on Boger fluids have provided a number of dramatic illustrations of elastico-viscous behaviour. Figure 20, plate 7, contains photographs for the rounded-corner planar

contraction geometry (figure 1*e*) and three Boger fluids. Of significant interest is the observation that, for all fluids and flow conditions tested, no significant vortex behaviour could be found and, if anything, this behaviour is not as strong as in the Newtonian case. There is some evidence to support the contention that rounding the corner results in a slight reduction in the size of the vortex region but, apart from this, the change in corner conditions has little visible effect on the characteristics in the bulk of the flow field.

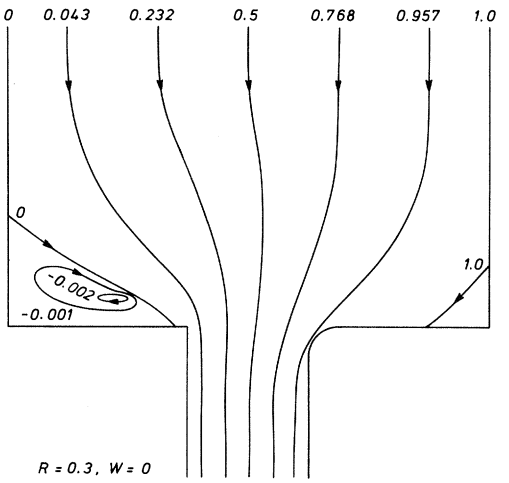

FIGURE 18. Numerical simulation for the planar contraction geometry (1*e*): Newtonian.

Figure 20 contrasts dramatically with the corresponding numerical simulations given in figure 21. A non-zero W gives rise to a substantial *increase* in the size and strength of the recirculating vortices, in marked contrast to the experimental results. Rounding one of the re-entrant corners has the effect of reducing the size of the associated recirculating region, with much disturbance to the flow throughout the geometry. Again, the coarse rounding of the corner under consideration is inappropriate as a replacement for a sharp re-entrant corner (at least within the context of the numerical strategy employed here).

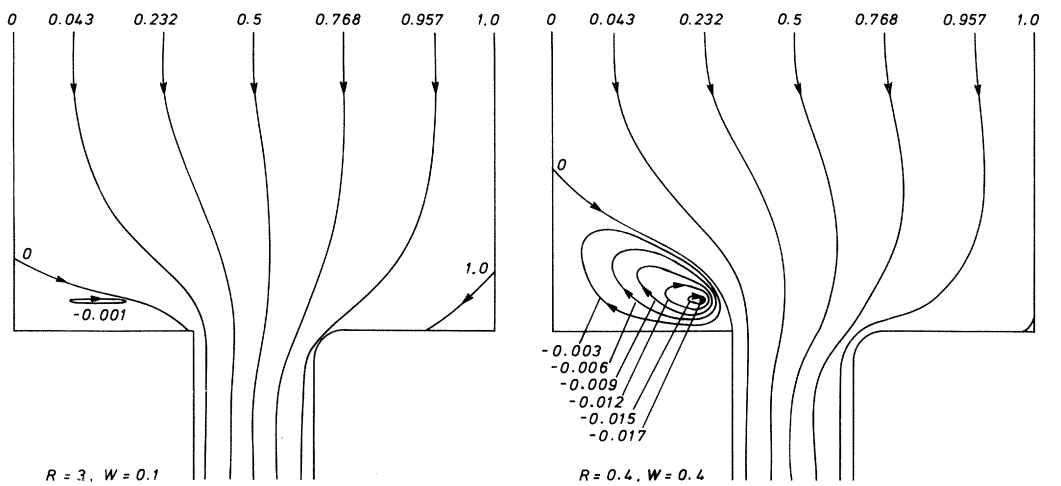

FIGURE 21. Numerical simulation for the Maxwell model (7) in the asymmetric planar contraction geometry (1*e*).

The theoretical and experimental results given in figures 20 and 21 for planar contractions have raised a number of interesting questions, the answers to which are not immediately apparent. Indeed, while many workers in computational non-Newtonian fluid mechanics have experimental evidence of vortex enhancement in circular contraction flow that they cannot predict (cf. Crochet & Bezy 1980), we have numerical predictions of vortex growth that we do not observe!

For completeness, we include in figure 22, plate 8, representative photographs for symmetrical planar *expansion* flow which were obtained very simply by reversing the flow in geometry 1*d*. Recirculating vortices are evident, associated with a rather abrupt change in the streamline directions near the wall. Figure 22 may be compared with a numerical prediction for model (7) given in figure 23 and *here* the agreement between theory and experiment is satisfactory.

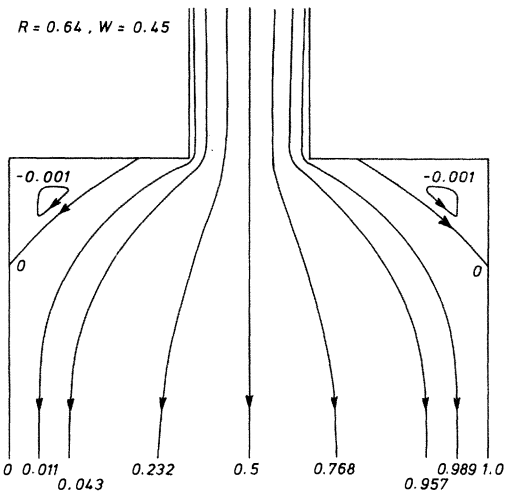

FIGURE 23. Numerical simulation for the Maxwell model (7) in the planar *expansion* geometry (1*d*).

Planar contraction flows contrast dramatically with the behaviour found in the corresponding circular contraction case. Figure 24, plate 9, contains photographs of the streamlines for the Boger fluid B10 obtained from the symmetrical geometry (figure 1*f*) covering a range of flow rates. Here, vortex enhancement is clearly discernible as the Reynolds number (based on conditions in the upstream tube) increases until a stage is reached when fluid inertia becomes important, and the vortices then begin to diminish in size. This behaviour is consistent with the detailed work of Boger and his collaborators (see, for example, Boger 1982).

Figure 24 may be compared with the corresponding photographs for the asymmetrical contraction geometry (figure 1*g*). These are given in figure 25, plate 10. The geometry is aligned so that the rounding of the exit lip is confined to the right half cross-section in all but figure 25*f*. In this last photograph, the geometry has been turned through 90° and the laser beam cuts the plane containing the discontinuity in corner geometry. This situation is a symmetrical viewing, as is evident from the photograph.

It is clear that rounding the sharp edge in the circular contraction geometry has a dramatic effect on flow characteristics. One of the vortex regions is significantly reduced in size by rounding the exit lip, while the size of the other is increased, and the change in lip geometry is seen to affect the whole of the flow field. Here again, there is clearly a strong interaction between corner

conditions and fluid-memory effects and the overall picture has similarities with that which was predicted (but not observed) in the planar contraction case. By implication, a 'rounding' technique to handle the abrupt change in geometry at the lip would need to be implemented with great care, necessitating perhaps an unacceptable level of mesh refinement.

(*d*) *Aqueous polymer solution*

It is clearly important to assess whether the provocative behaviour for the Boger fluids is characteristic of all non-Newtonian elastic liquids. To facilitate such an assessment, we did similar experiments on the polymer solution C1 discussed in §2*b*. We note that the essential difference between C1 and the Boger fluids is the absence of maltose syrup in C1.

Figure 26*a*, plate 11, contains a photograph for C1 in the symmetric planar contraction geometry (figure 1*d*). A comparison between this figure and those for the Boger fluids immediately reveals qualitatively different behaviour. The recirculating regions are now substantial in size (cf. Giesekus 1968) but the vortex motion is very weak indeed, with the flow almost stagnant in comparison with that in the fast-flowing jet-like central region.

Rounding one of the corners again results in a smaller recirculating region and the basic symmetry of the flow is destroyed (cf. figure 26*b*) just as was reported for the Boger fluids in the *circular* contraction geometry and predicted from the Maxwell model in a planar contraction situation.

The flow of polymer solution C1 in the circular contraction geometries is shown in figures 26*c*, *d* and figure 27, plate 12, for both the symmetric and the partly rounded lip cases. Here the behaviour is similar to that observed for liquid C1 in the planar contraction geometry. An extensive but weak recirculating flow is evident and the corner has the effect of reducing the size of the vortex region (cf. figures 26*c*, *d*). If anything, rounding the lip has a less evident effect in this geometry than in the corresponding planar case.

It is interesting to speculate as to the reasons for the different behaviours of the Boger fluids and the aqueous polymer solution C1. The marked shear-thinning behaviour of C1 has already been referred to, and simple laboratory tests indicate that although both systems show substantial resistance to stretching motions, the Boger fluids are particularly noticeable in this respect. However, assigning the differences in behaviour in contraction flows to these factors would appear to be too simplistic at this stage, and it must remain therefore as an open matter for debate.

In the sense that it has been known for many years that some polymer systems exhibit vortices in contraction flows while others do not and that the reason for this remains a matter of conjecture, the present work has simply added to the number of outstanding problems. These findings have therefore re-emphasized the fact that it is dangerous to make generalizations in the area of contraction flows when these involve non-Newtonian systems.

(*e*) *Conclusions*

It is of interest to list the main conclusions that can be drawn from the present work on contraction flows.

(i) Contraction flows for Newtonian fluids do not present significant problems. The observed behaviour is in broad general agreement with numerical simulations.

(ii) The experiments on the Boger fluids demonstrate that it is possible to obtain substantial vortex behaviour in circular contraction flows and virtually none in the corresponding planar case.

(iii) It would be wrong to generalize conclusion (ii) to all polymer systems since the aqueous polyacrylamide solution C1 showed similar vortex characteristics in *both* circular and planar contraction flows.

(iv) A relatively small change in lip geometry in the circular contraction flow of Boger fluids can have a significant influence on flow characteristics throughout the flow field.

(v) A coarse rounding-of-the-corner numerical technique to handle sharp re-entrant corners is inappropriate, especially for highly elastic liquids.

(vi) Existing numerical simulation work for non-Newtonian elastic liquids is inadequate to explain some of the phenomena described in the present paper. Future work must concentrate on different rheological equations of state, precise corner specification and the ability to obtain solutions at high values of elasticity. Solutions that are essentially perturbations about the Newtonian case are unlikely to be of any relevance in this context.

We are most grateful to Dr T. Cochrane for much helpful advice and instruction in the early stages of the work. Discussions with Dr D. V. Boger, Dr A. R. Davies, Dr H. Holstein and Dr W. M. Jones were also of considerable help. Finally, Mr R. Evans gave invaluable assistance throughout the experimental programme, particularly with regard to the photography.

During the course of the work described in this paper, M. F. W. was employed as a post-doctoral research associate on a research grant financed by the S.R.C.

References

Black, J. R., Denn, M. M. & Hsaio, G. C. 1975 In *Theoretical rheology* (ed. J. F. Hutton, J. R. A. Pearson & K. Walters), pp. 3–30. Barking, Essex: Applied Science Publishers.

Boger, D. V. 1977/8 *J. non-Newtonian Fluid Mech.* **3**, 87–91.

Boger, D. V. 1980 *Proc. 8th Int. Congr. on Rheology, Naples*, vol. 1, pp. 195–218. New York and London: Plenum Press.

Boger, D. V. 1982 *Adv. Transport processes.* (In the press.)

Cochrane, T., Walters, K. & Webster, M. F. 1981 *Phil. Trans. R. Soc. Lond.* A **301**, 163–181.

Cochrane, T., Walters, K. & Webster, M. F. 1982 *J. non-Newtonian Fluid Mech.* **10**, 95–114.

Cogswell, F. N. 1972 *Polym. Engng Sci.* **12**, 64–73.

Crochet, M. J. & Bezy, M. 1980 *Proc. 8th Int. Congr. on Rheology, Naples*, vol. 2, pp. 53–58. New York and London: Plenum Press.

Crochet, M. J., Davies, A. R. & Walters, K. 1983 *Numerical simulation of non-Newtonian flow.* New York and Amsterdam: Elsevier (In the press.)

Davies, A. R., Walters, K. & Webster, M. F. 1979 *J. non-Newtonian Fluid Mech.* **4**, 325–344.

Giesekus, H. 1968 *Rheol. Acta* **7**, 127–138.

Holstein, H. 1981 Ph.D. thesis, University of Wales, Aberystwyth.

Holstein, H. & Paddon, D. J. 1981 *J. non-Newtonian Fluid Mech.* **8**, 81–93.

Kawaguti, M. 1965 Mathematics Research Center Report no. 574, University of Wisconsin.

Keentok, M., Georgescu, A. G., Sherwood, A. A. & Tanner, R. I. 1980 *J. non-Newtonian Fluid Mech.* **6**, 303–324.

Moffatt, H. K. 1964 *J. Fluid Mech.* **18**, 1–18.

Oldroyd, J. G. 1950 *Proc. R. Soc. Lond.* A **200**, 523–451.

Roache, P. J. 1972 *Computational fluid dynamics.* Albuquerque, New Mexico: Hermosa Publications.

Walters, K. 1975 *Rheometry.* London: Chapman and Hall.

Walters, K. (ed.) 1980 *Rheometry: industrial applications.* Chichester: John Wiley and Sons.

White, J. L. & Kondo, A. 1977/8 *J. non-Newtonian Fluid Mech.* **3**, 41–64.

Viriyayuthakorn, M. & Caswell, B. 1980 *J. non-Newtonian Fluid Mech.* **6**, 245–267.

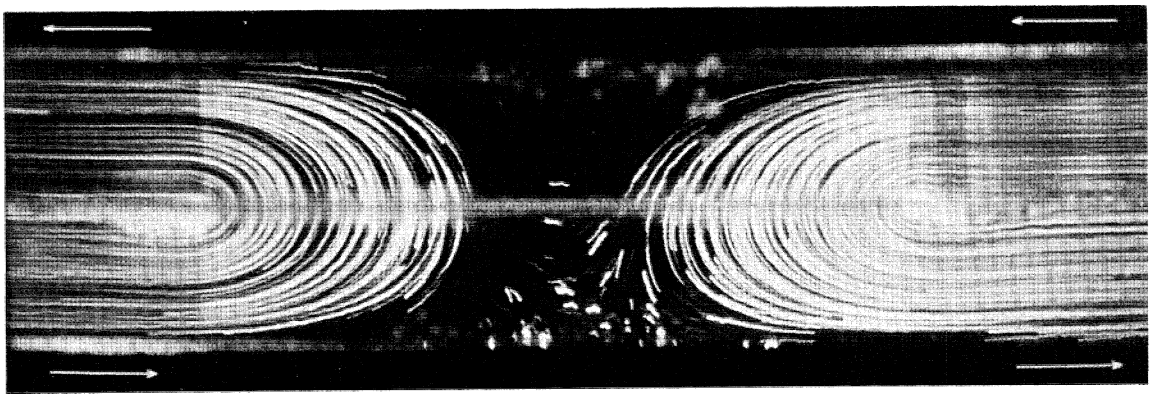

(*a*) $R = 1$, $W = 0$

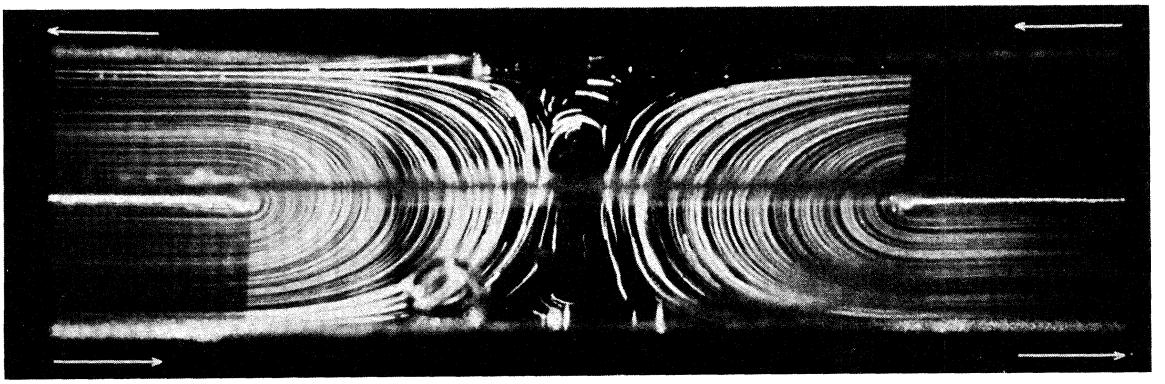

(*b*) $R = 8$, $W = 0.41$

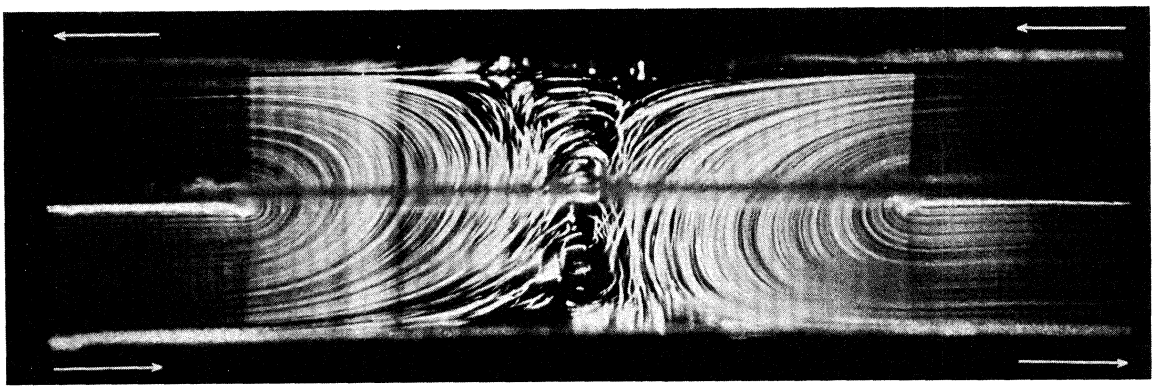

(*c*) $R = 16$, $W = 0.81$

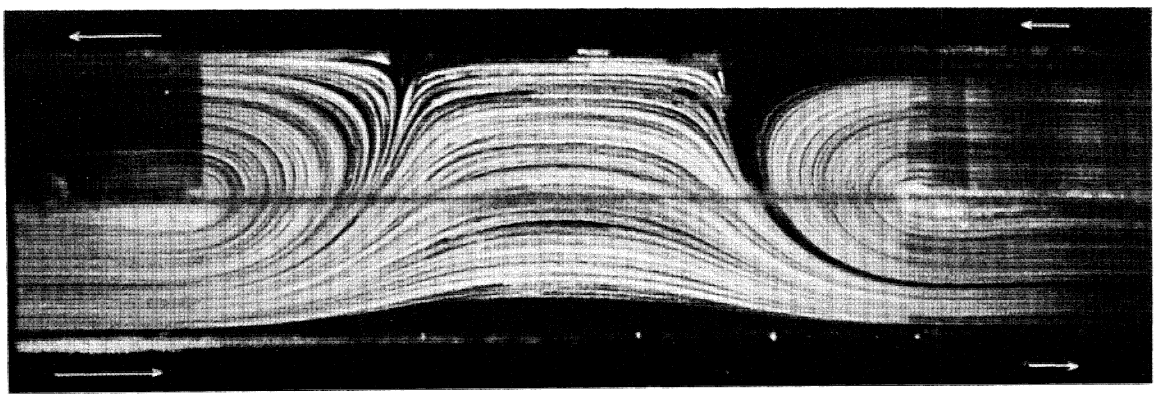

(*d*) $R = 2$, $W = 0$

FIGURE 9. Flow in the wide-gap geometry (1*a*): (*a*) and (*d*) Newtonian; (*b*) and (*c*) liquid B7; equal flow rates in all arms for (*a*)–(*c*); flow conditions for (*d*) as in figure 8.

(*Facing p.* 218)

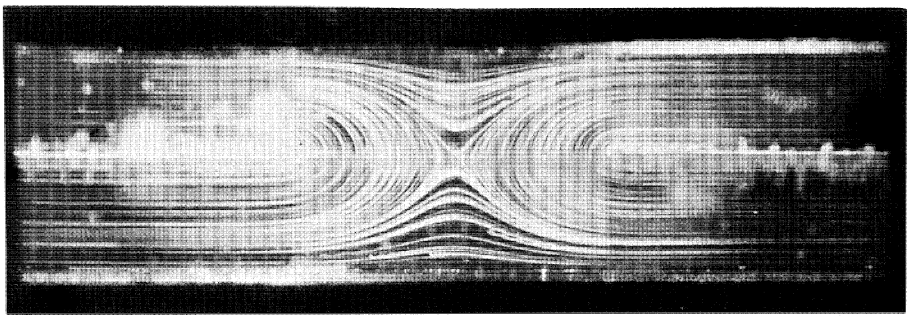

(*a*) $R = 5$, $W = 0$

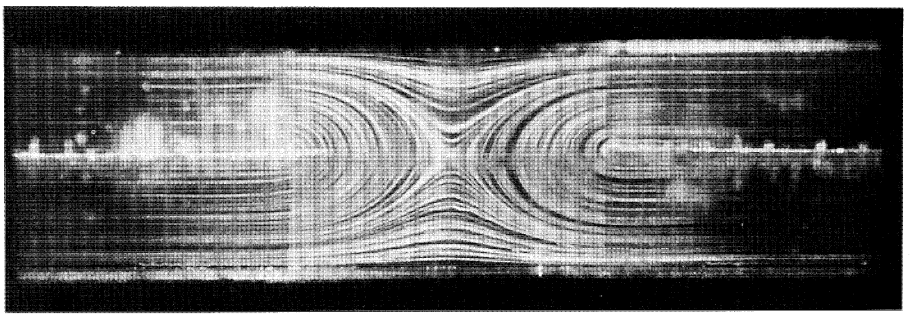

(*b*) $R = 10$, $W = 0$

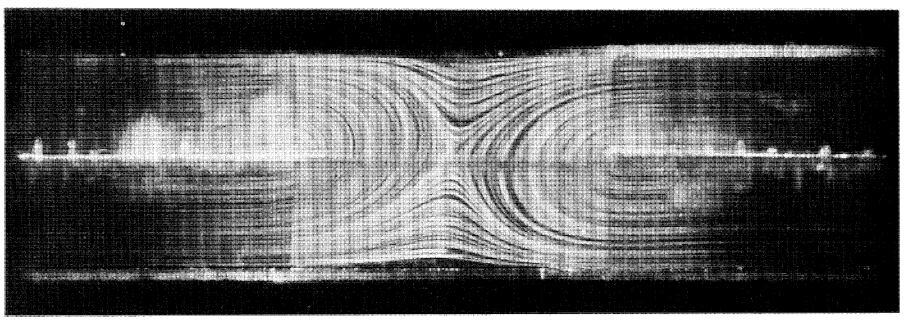

(*c*) $R = 15$, $W = 0$

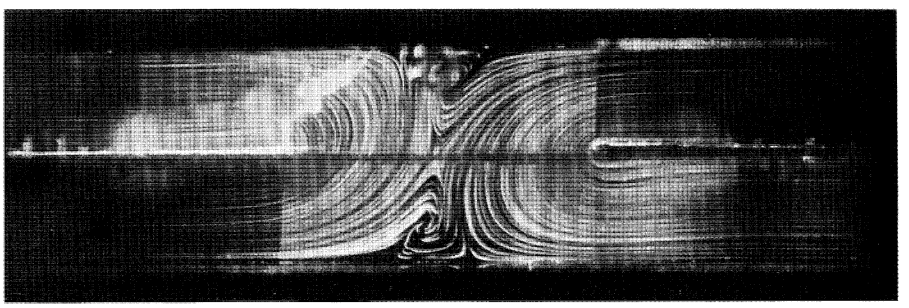

(*d*) $R = 23$, $W = 0$

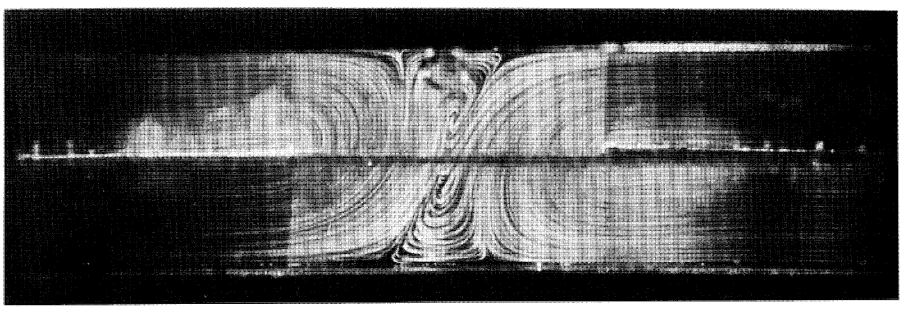

(*e*) $R = 25$, $W = 0$

FIGURE 12. Flow in the medium-gap geometry (1*b*): Newtonian; equal flow rates in all arms.

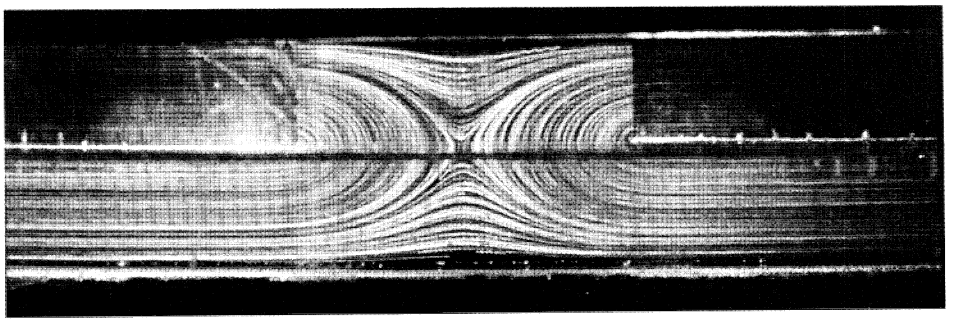

(*a*) $R = 5$, $W = 0.11$

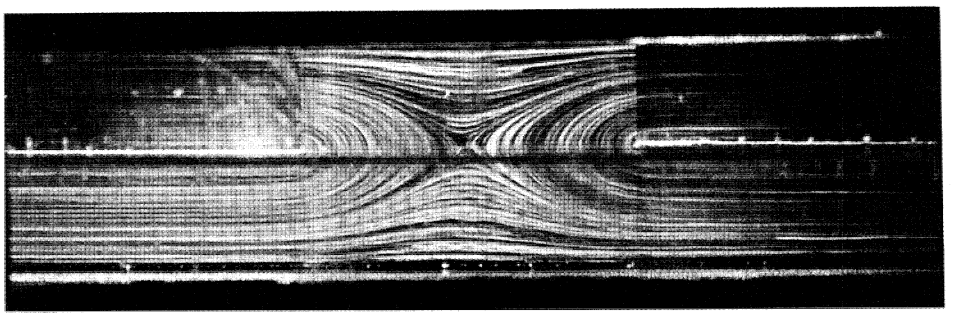

(*b*) $R = 10$, $W = 0.21$

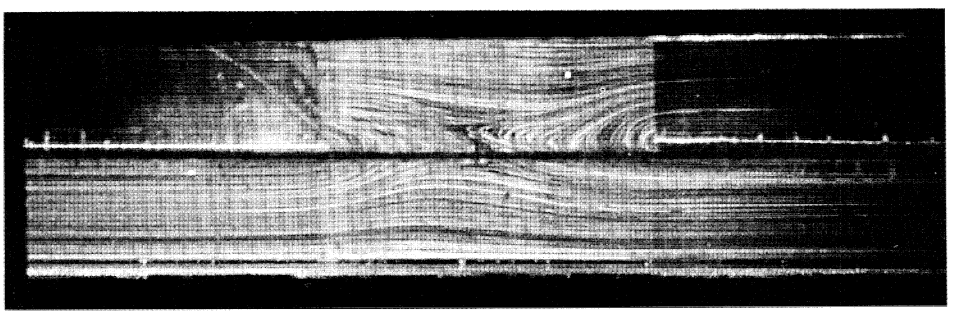

(*c*) $R = 15$, $W = 0.32$

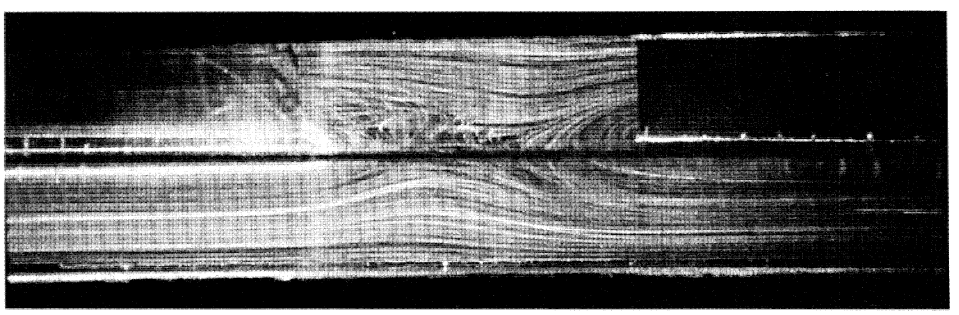

(*d*) $R = 25$, $W = 0.53$

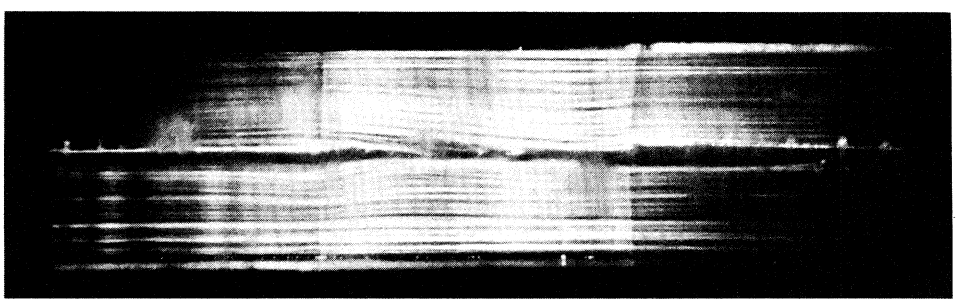

(*e*) $R = 2$, $W = 0.55$

FIGURE 13. Flow in the medium-gap geometry (1*b*): (*a*)–(*d*) liquid B6; (*e*) liquid B5; equal flow rates in all arms.

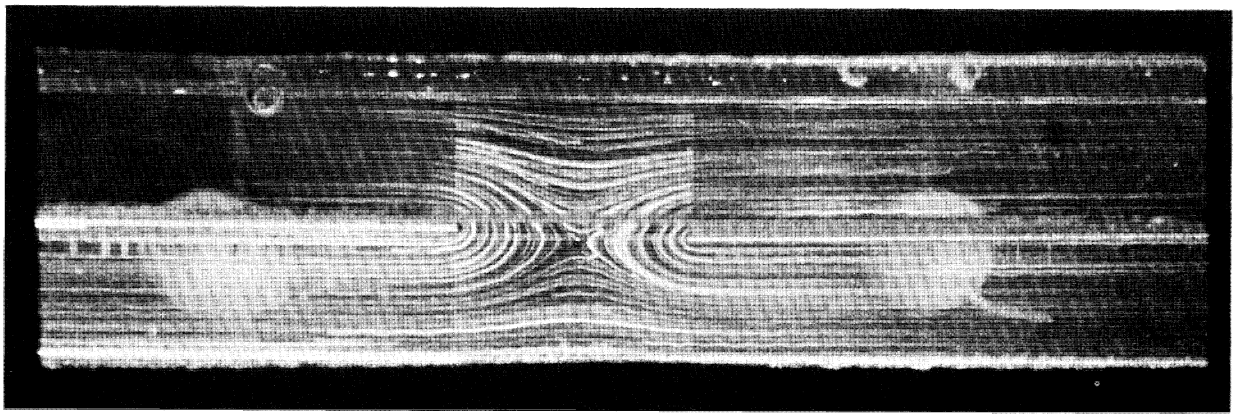

(*a*) $R = 2$, $W = 0$

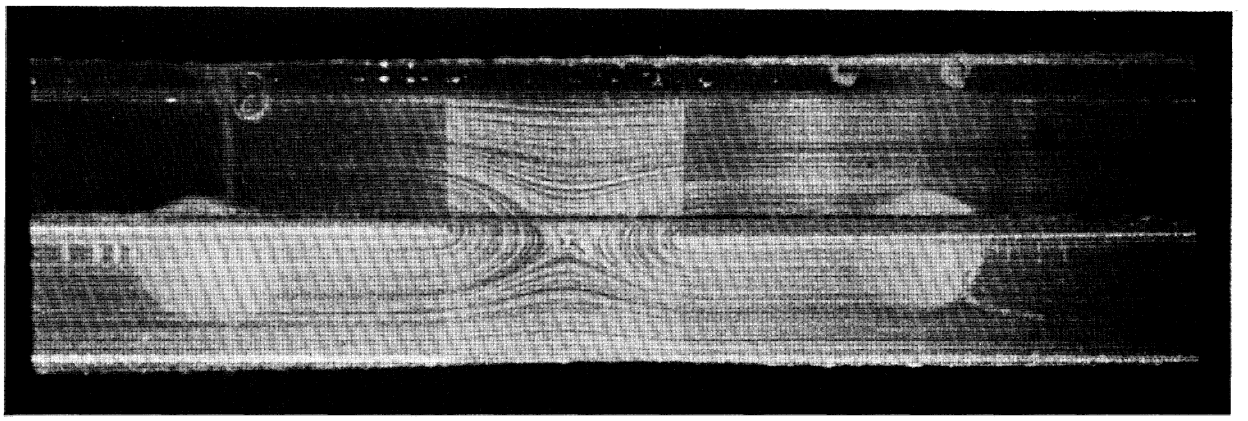

(*b*) $R = 4$, $W = 0$

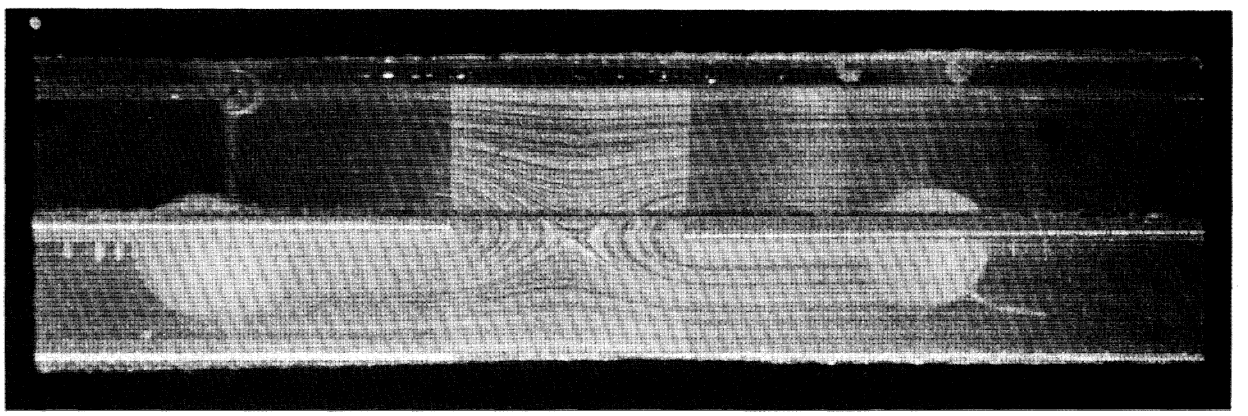

(*c*) $R = 8$, $W = 0$

FIGURE 15. Flow in the narrow-gap geometry (1*c*): Newtonian; equal flow rates in all arms.

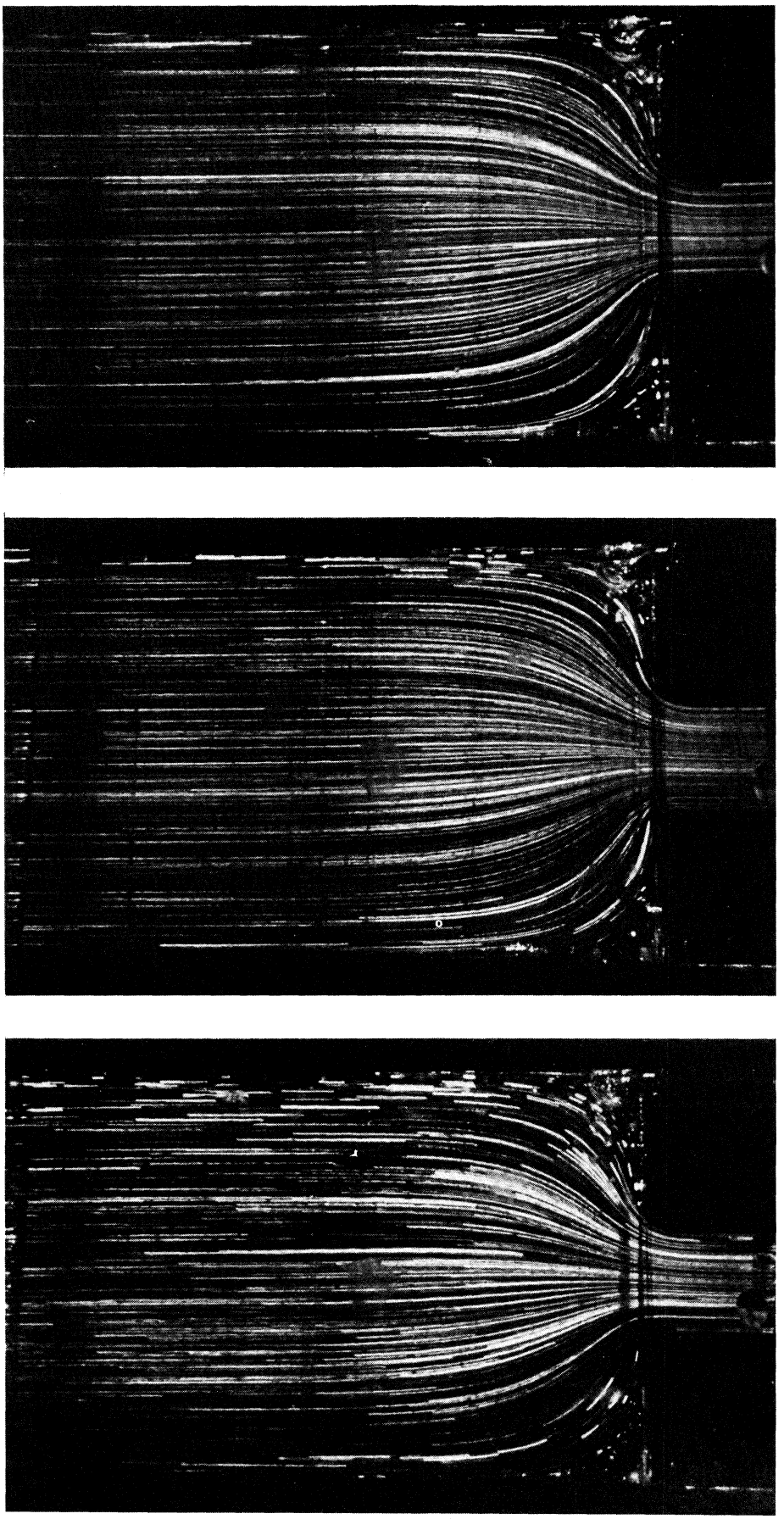

(*a*) $R = 3$, $W = 0.01$, (*b*) $R = 0.04$, $W = 0.04$ (*c*) $R = 0.8$, $W = 0.53$

FIGURE 17. Flow in the planar contraction geometry (1*e*): Newtonian.

(*a*) $R = 0.02$, $W = 0$

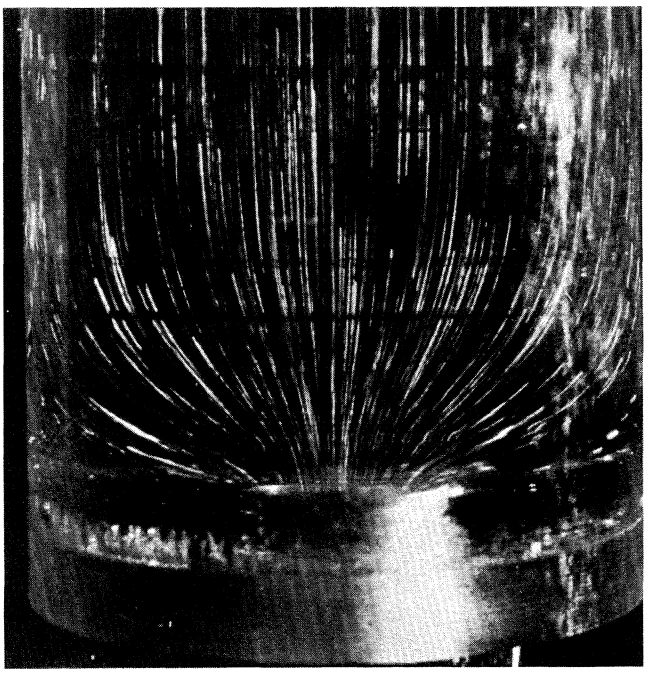

(*b*) $R = 0.06$, $W = 0$

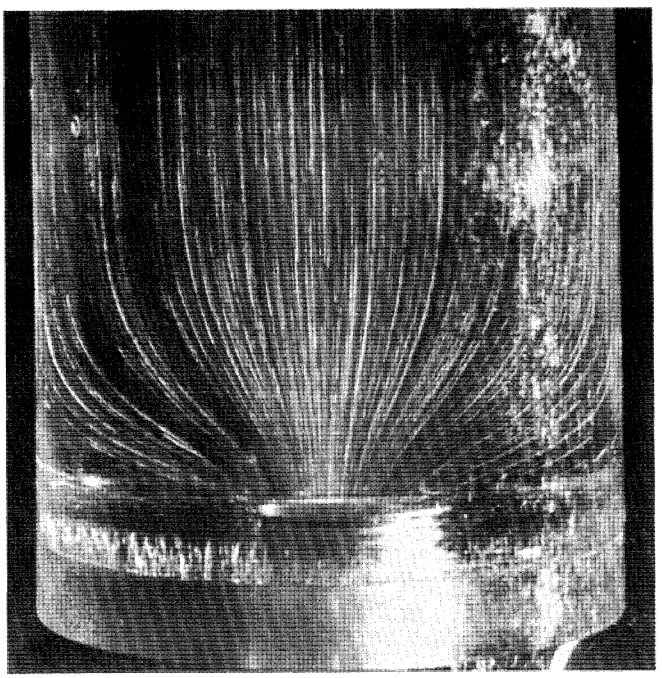

(*c*) $R = 0.09$, $W = 0$

(*d*) $R = 0.13$, $W = 0$

FIGURE 19. Flow in the circular contraction geometry (1*g*): Newtonian.

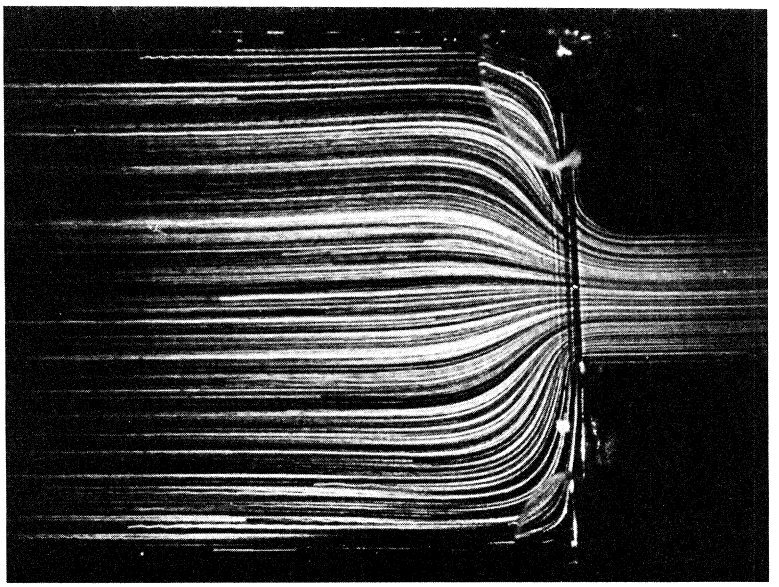

(*c*) $R = 0.8$, $W = 0.53$

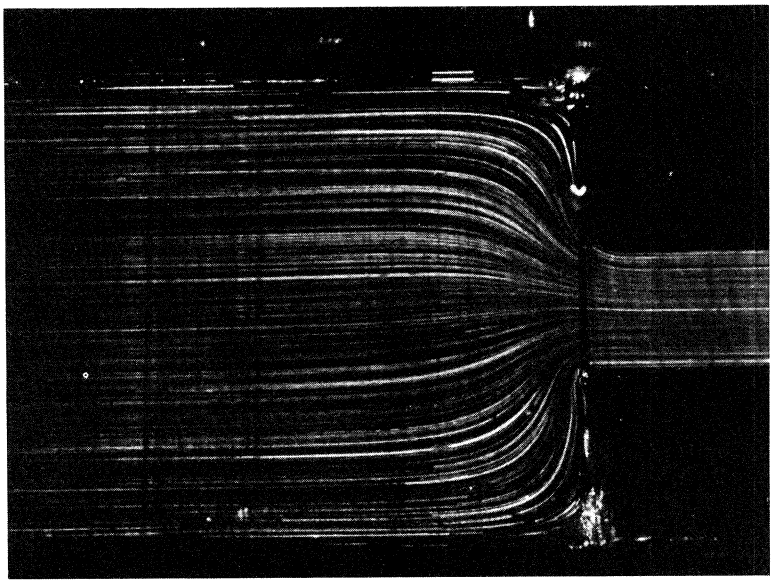

(*b*) $R = 0.04$, $W = 0.04$

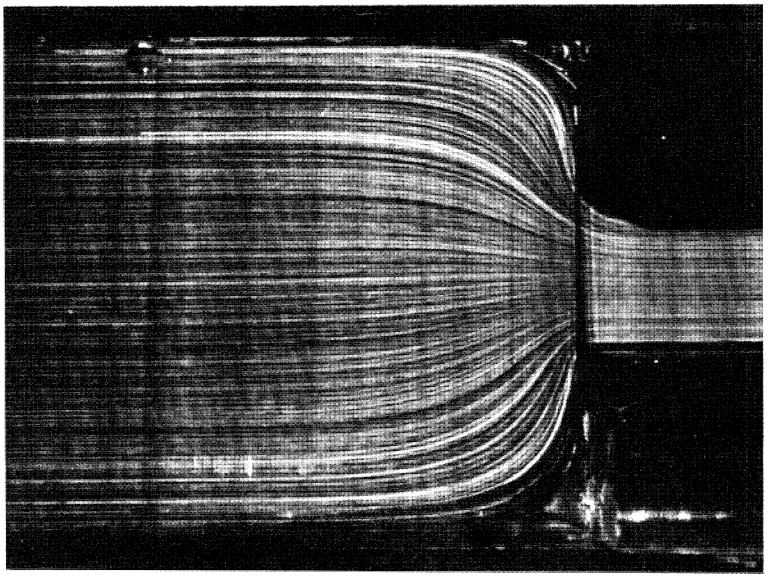

(*a*) $R = 3$, $W = 0.01$,

FIGURE 20. Flow in the planar contraction geometry (1*e*): (*a*) liquid B9; (*b*) liquid B10; (*c*) liquid B8.

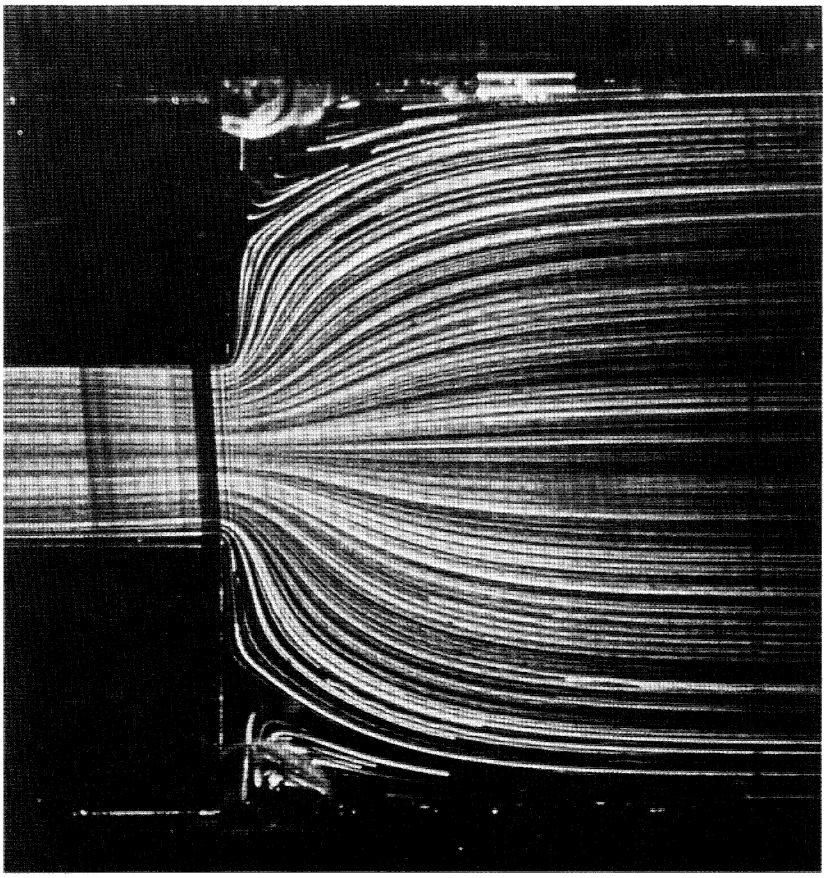

(*b*) $R = 0.8$, $W = 0.53$

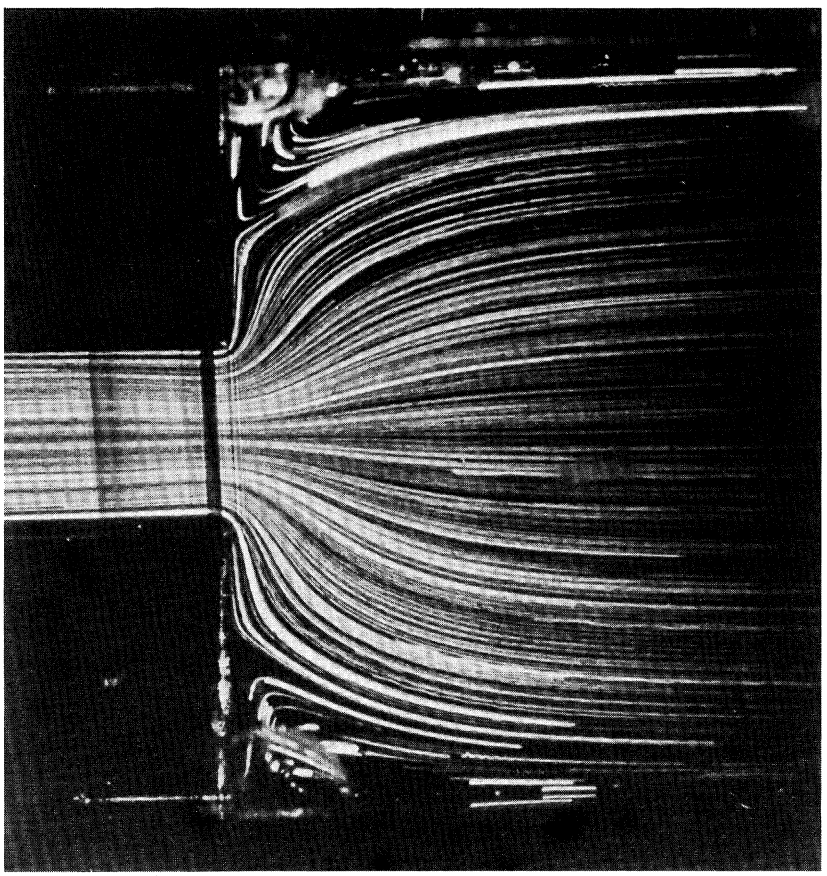

(*a*) $R = 0.64$, $W = 0.43$

FIGURE 22. Flow in the planar *expansion* geometry (1*d*): liquid B8.

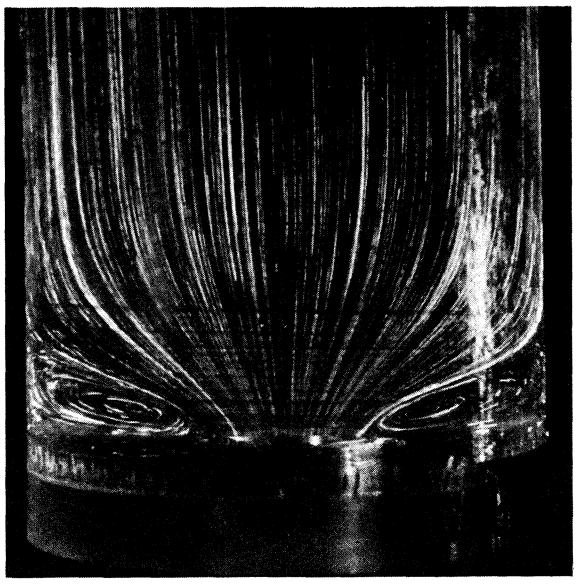

(*a*) $R = 0.08$, $W = 0.11$

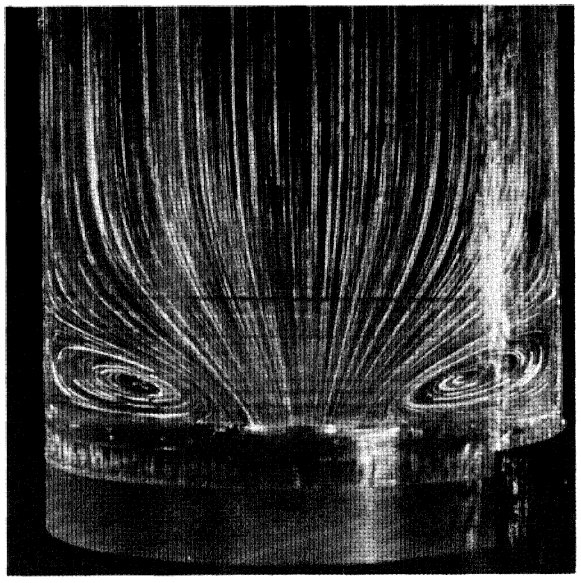

(*b*) $R = 0.11$, $W = 0.15$

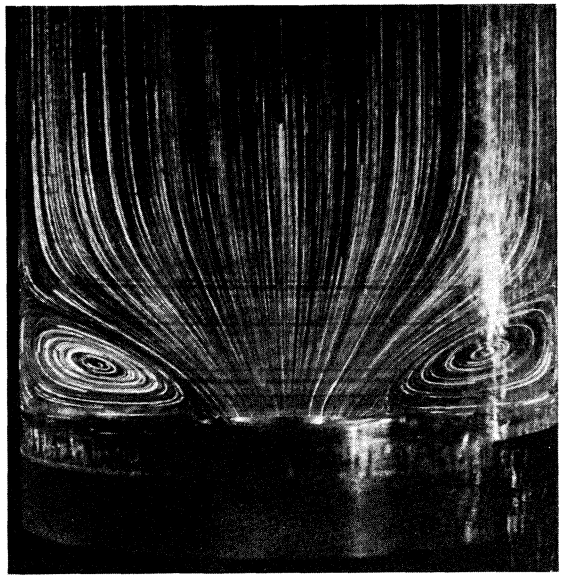

(*c*) $R = 0.15$, $W = 0.22$

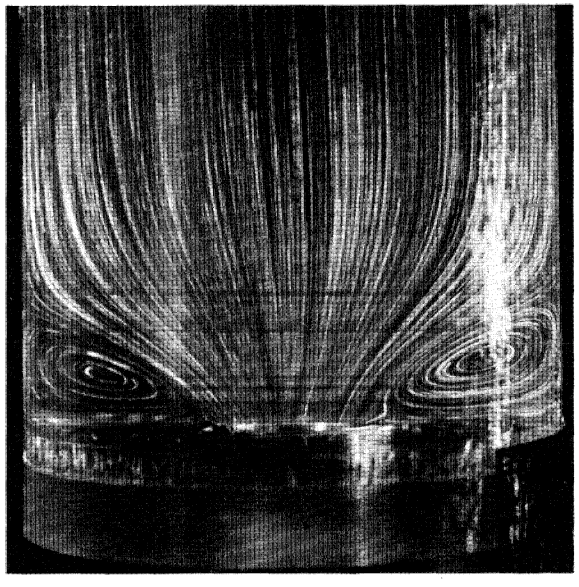

(*d*) $R = 0.17$, $W = 0.24$

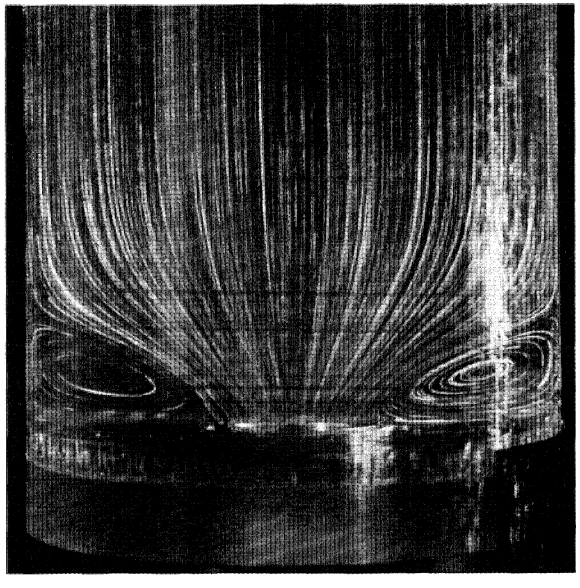

(*e*) $R = 0.19$, $W = 0.27$

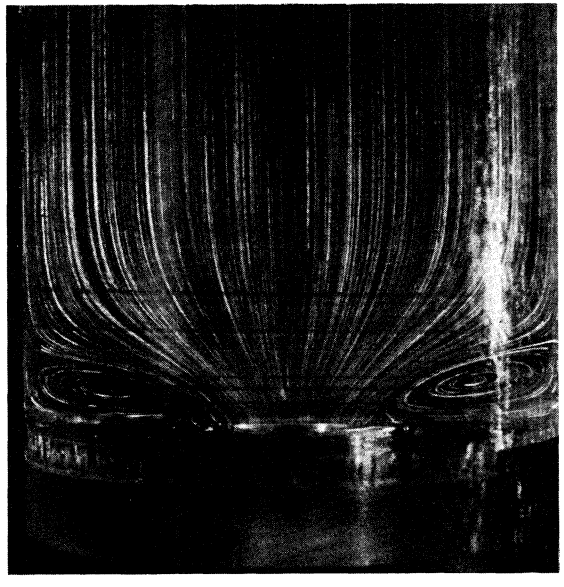

(*f*) $R = 0.21$, $W = 0.3$

FIGURE 24. Flow in the symmetrical circular contraction geometry (1*f*): liquid B10.

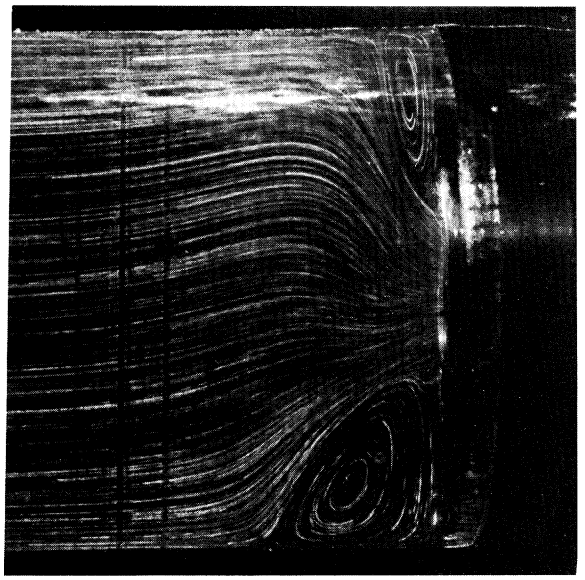

(*c*) $R = 0.15$, $W = 0.22$

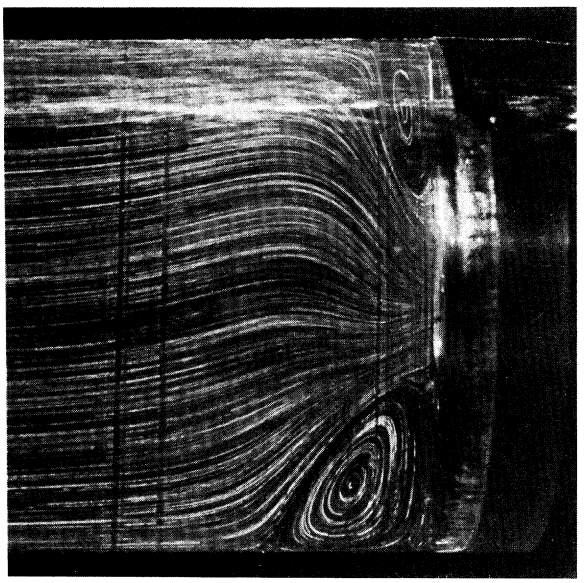

(*b*) $R = 0.13$, $W = 0.18$

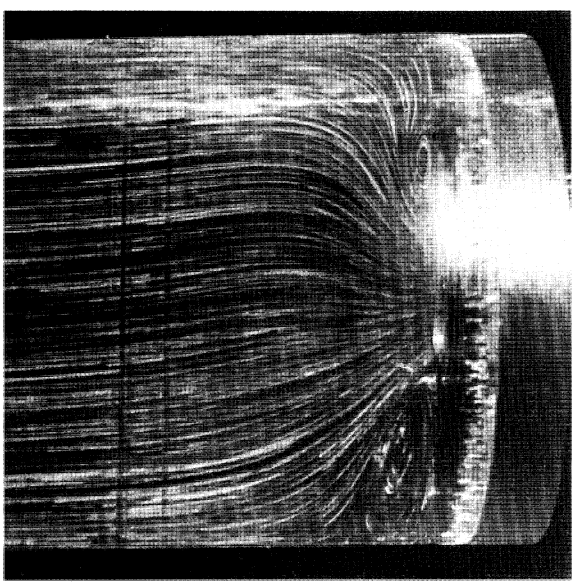

(*a*) $R = 0.08$, $W = 0.11$

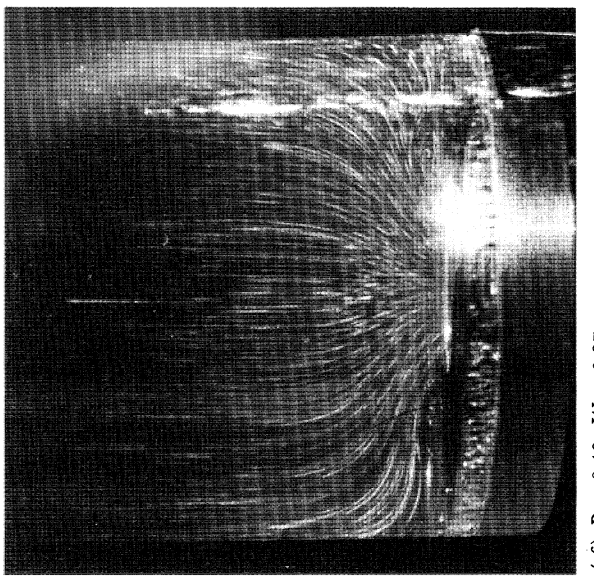

(*f*) $R = 0.19$, $W = 0.27$

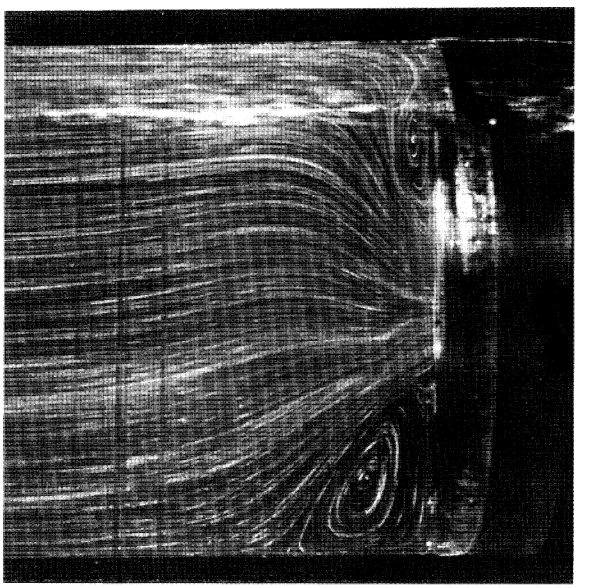

(*e*) $R = 0.19$, $W = 0.27$

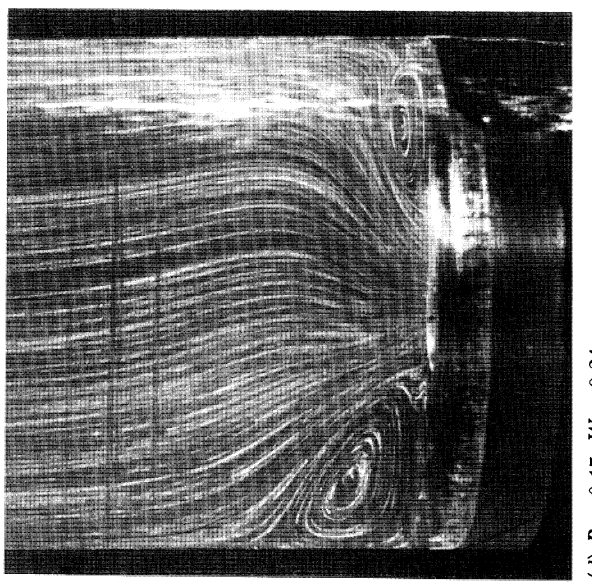

(*d*) $R = 0.17$, $W = 0.24$

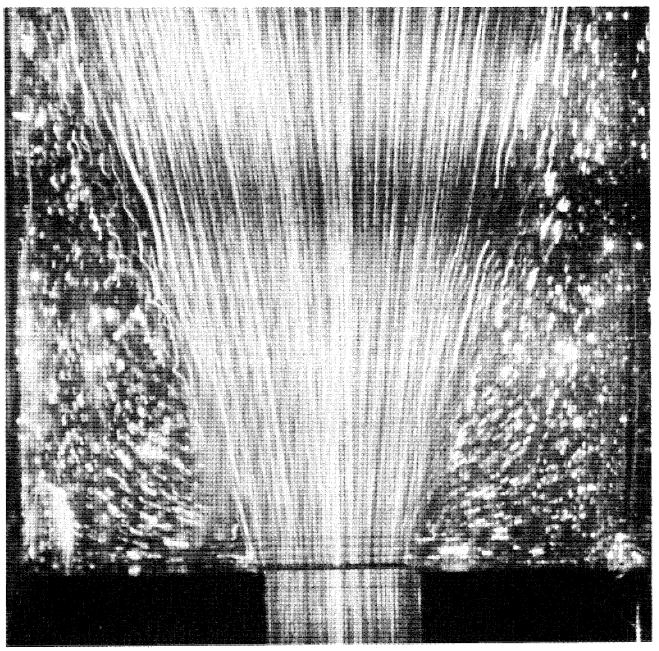

(*a*) geometry 1*d*, $Q = 0.5$ ml s^{-1}

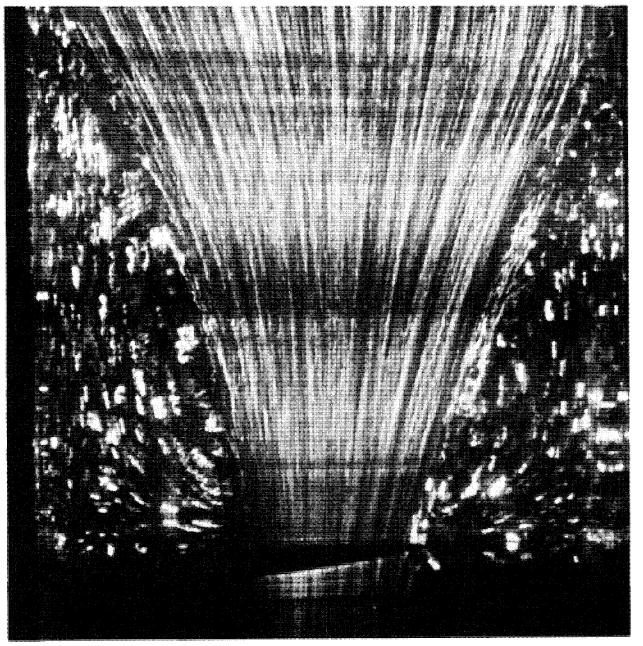

(*b*) geometry 1*e*, $Q = 1.67$ ml s^{-1}

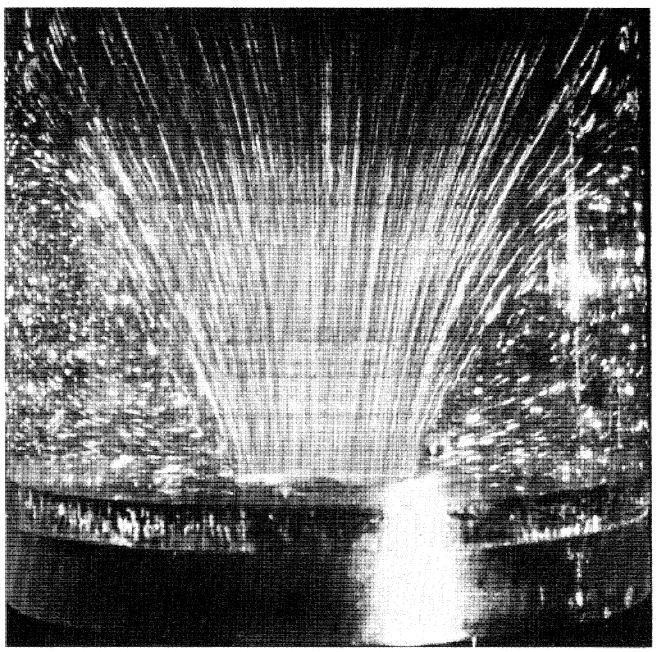

(*c*) geometry 1*g*, $Q = 0.5$ ml s^{-1}

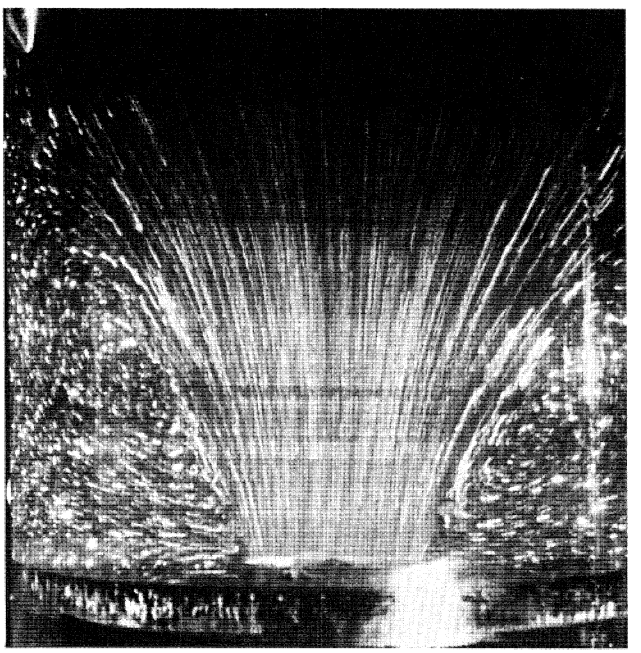

(*d*) geometry 1*g*, $Q = 0.83$ ml s^{-1}

FIGURE 26. Flow of liquid C1 in various contraction geometries: (*a*) geometry (1*d*), flow rate $Q = 0.5$ ml s^{-1}; (*b*) geometry (1*e*), flow rate $Q = 1.67$ ml s^{-1}; (*c*) geometry (1*g*), flow rate $Q = 0.5$ ml s^{-1}; (*d*) geometry (1*g*), flow rate $Q = 0.83$ ml s^{-1}. There is some evidence of camera shake in (*b*).

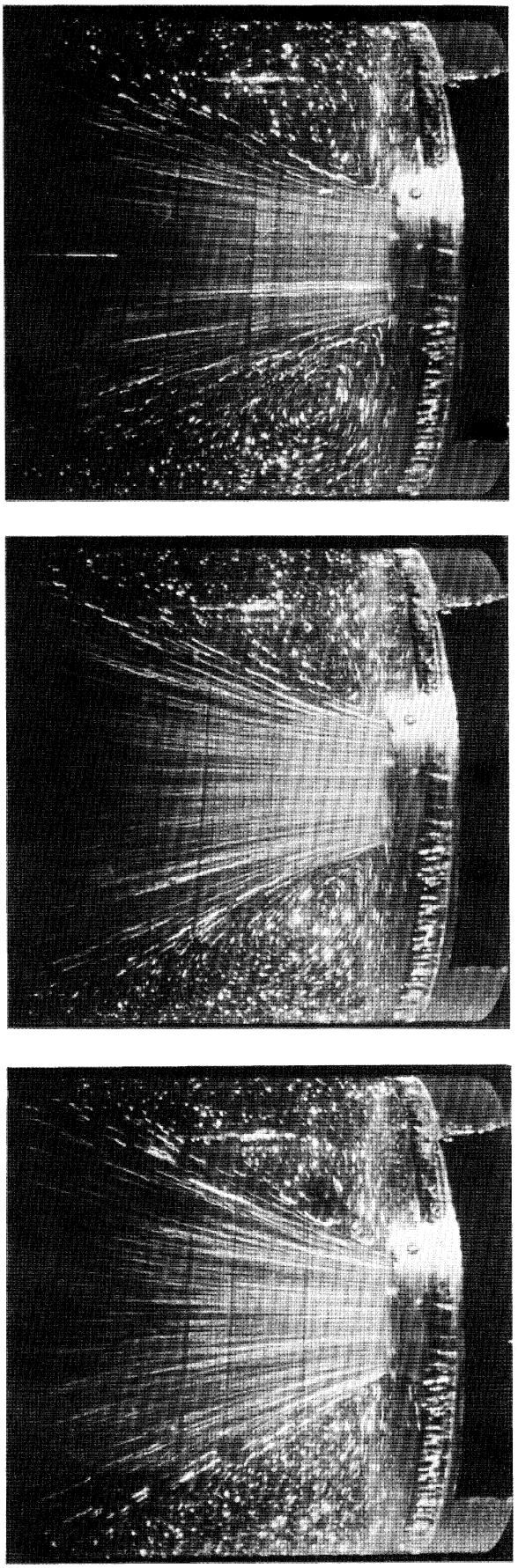

(*a*) $Q = 0.5$ ml s^{-1} (*b*) $Q = 0.83$ ml s^{-1} (*c*) $Q = 1.67$ ml s^{-1}

FIGURE 27. Flow of liquid C1 in symmetrical circular contraction geometry (1*f*): (*a*) $Q = 0.5$ ml s^{-1}; (*b*) $Q = 0.83$ ml s^{-1}; (*c*) $Q = 1.67$ ml s^{-1}.

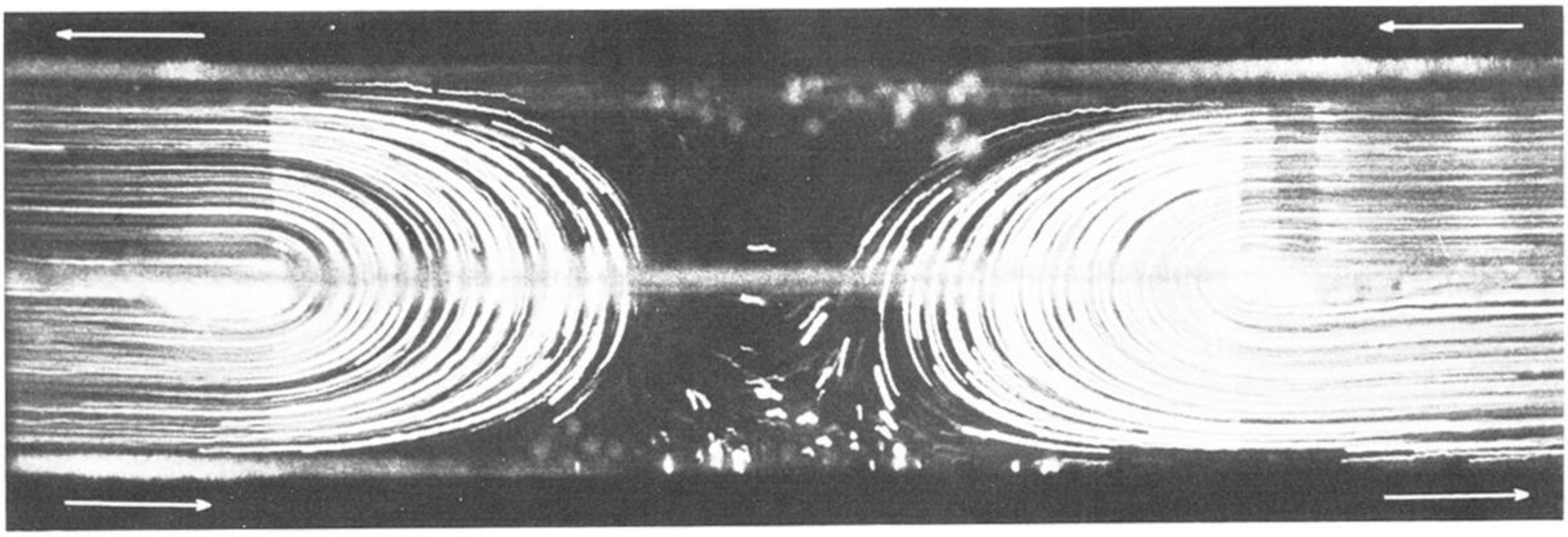

(*a*) $R = 1,\ W = 0$

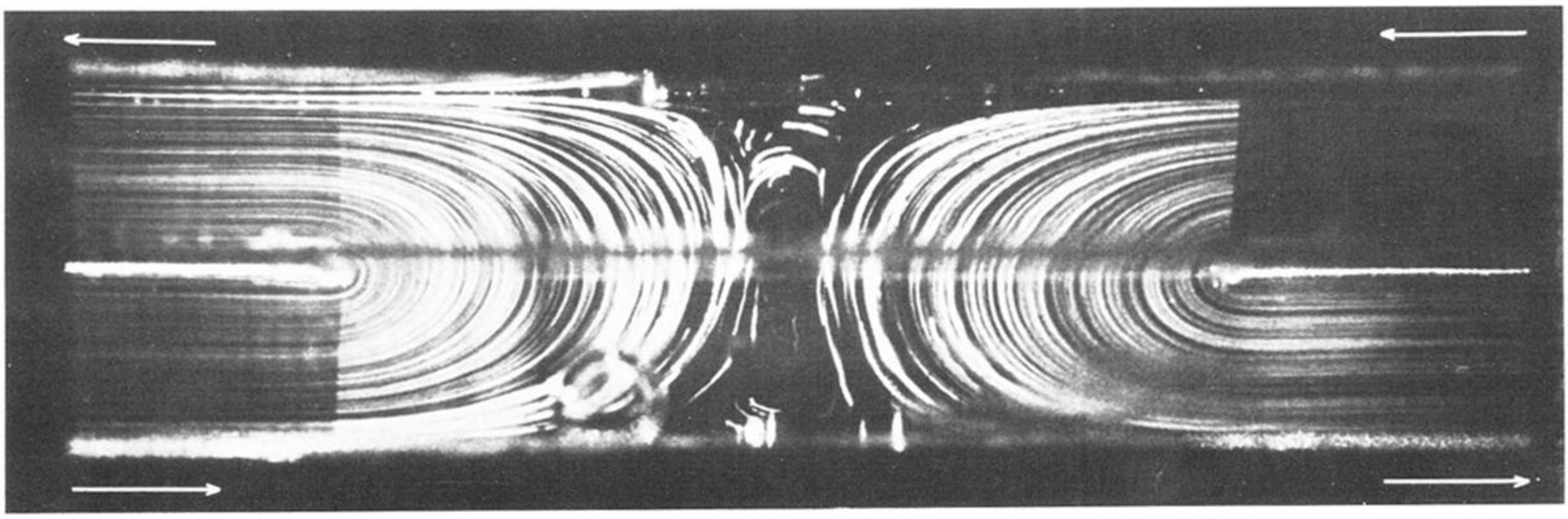

(*b*) $R = 8,\ W = 0.41$

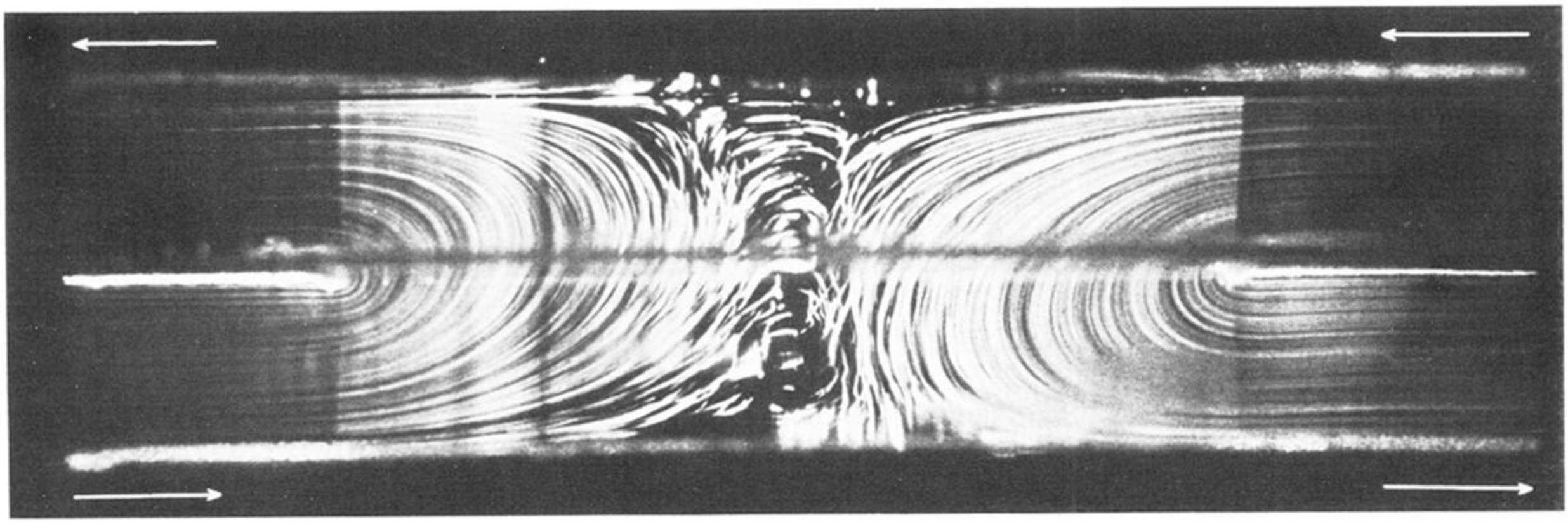

(*c*) $R = 16,\ W = 0.81$

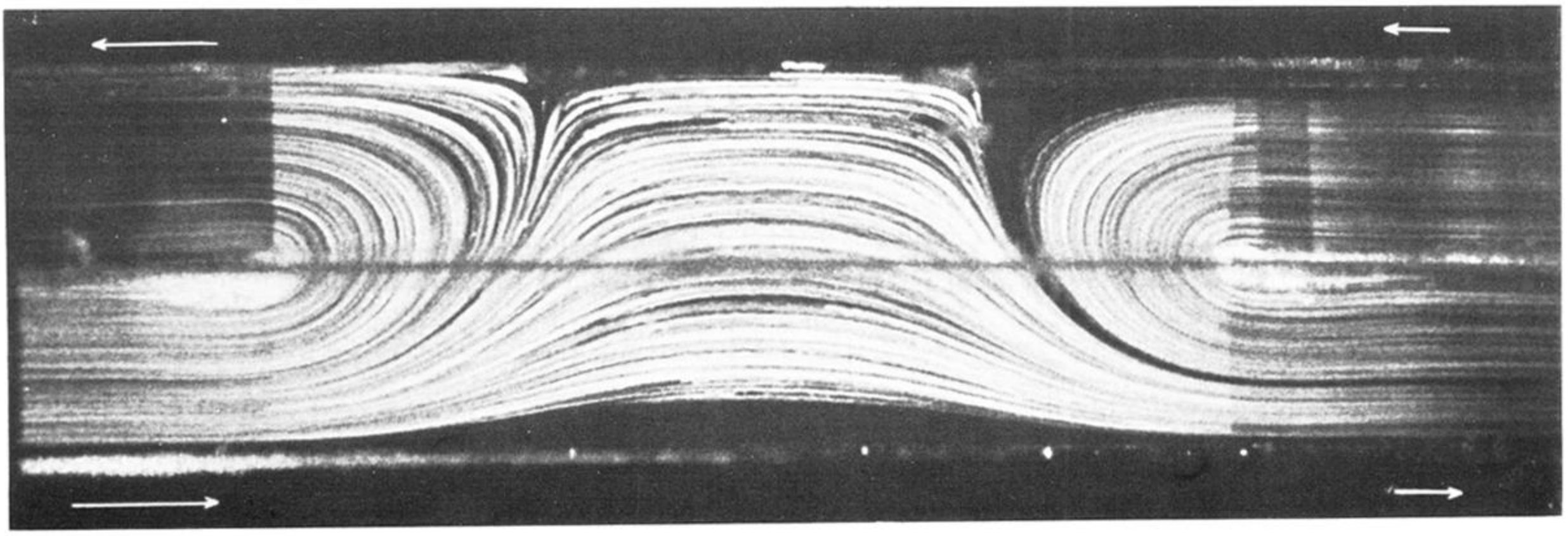

(*d*) $R = 2,\ W = 0$

FIGURE 9. Flow in the wide-gap geometry (1*a*): (*a*) and (*d*) Newtonian; (*b*) and (*c*) liquid B7; equal flow rates in all arms for (*a*)–(*c*); flow conditions for (*d*) as in figure 8.

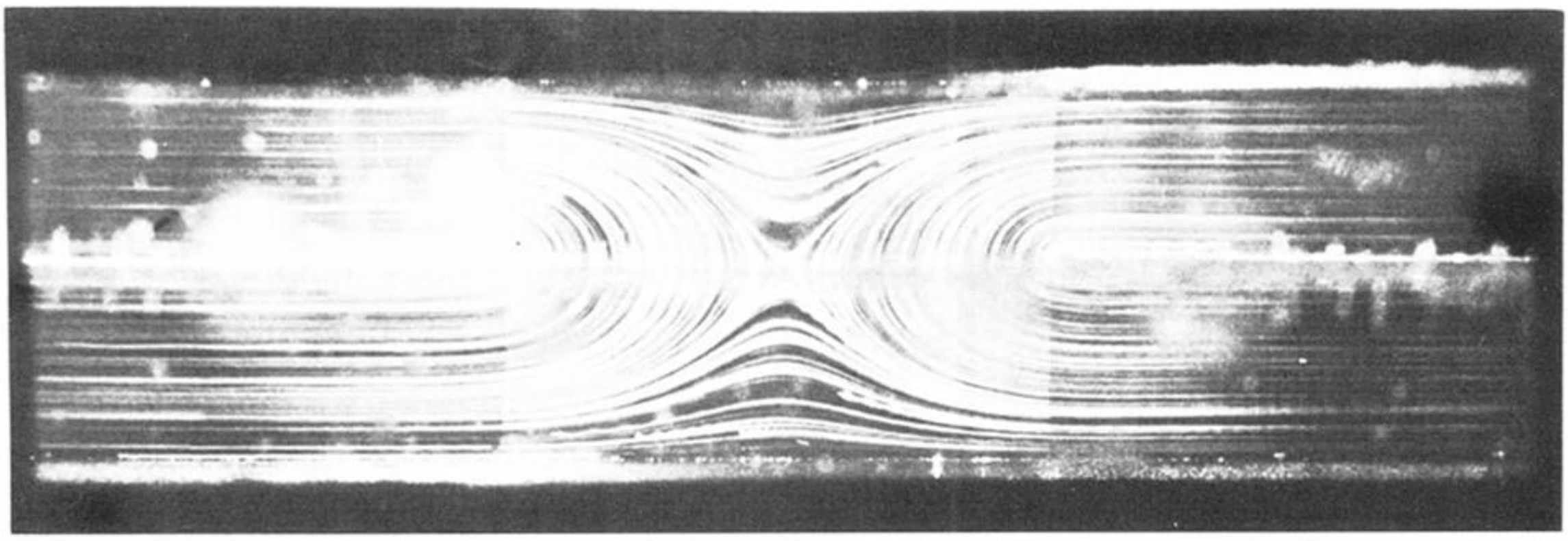

(*a*) $R = 5,\ W = 0$

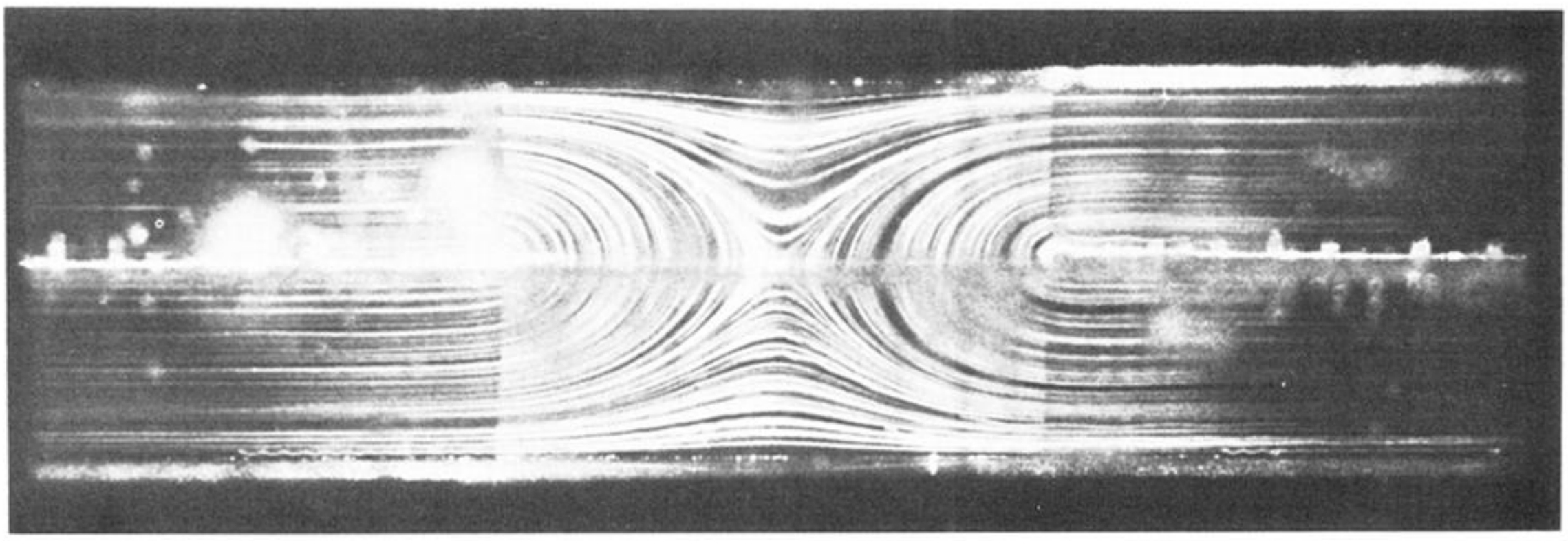

(*b*) $R = 10,\ W = 0$

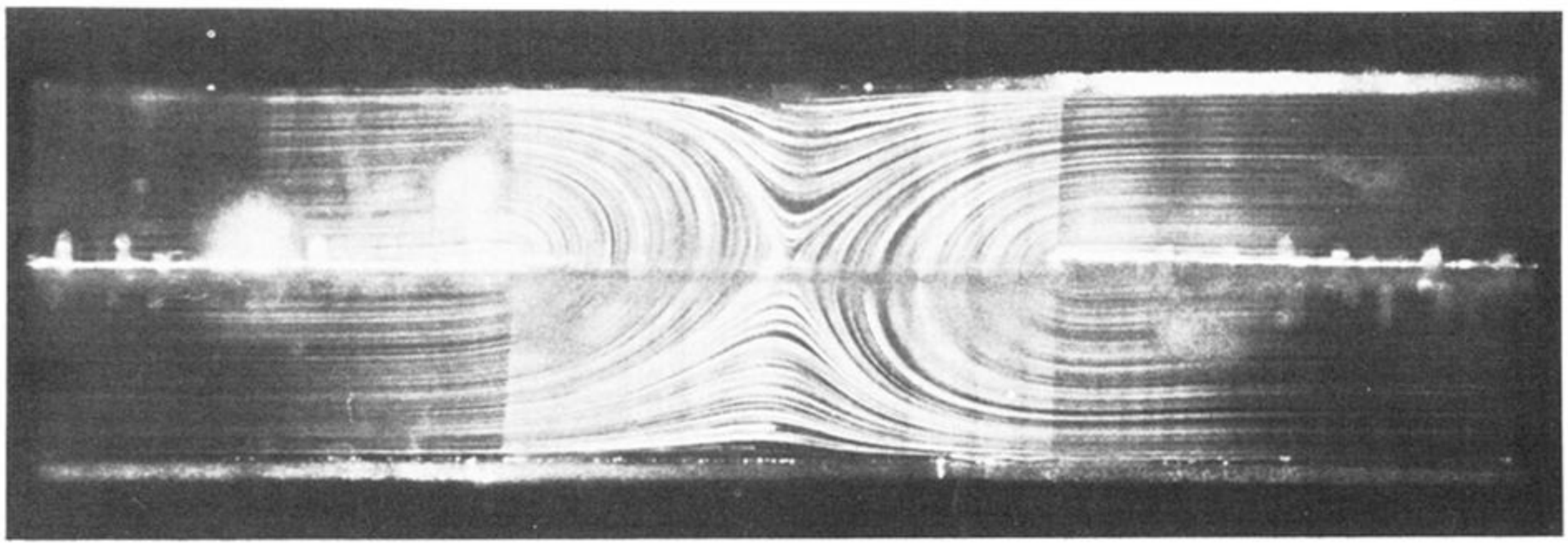

(*c*) $R = 15,\ W = 0$

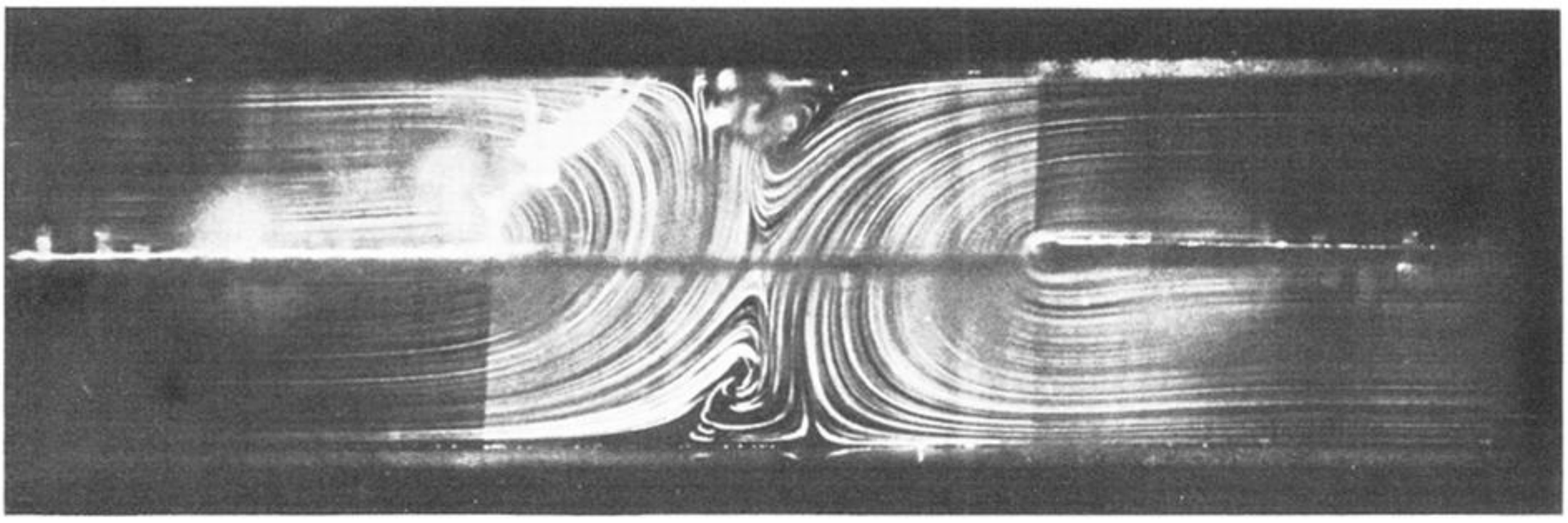

(*d*) $R = 23,\ W = 0$

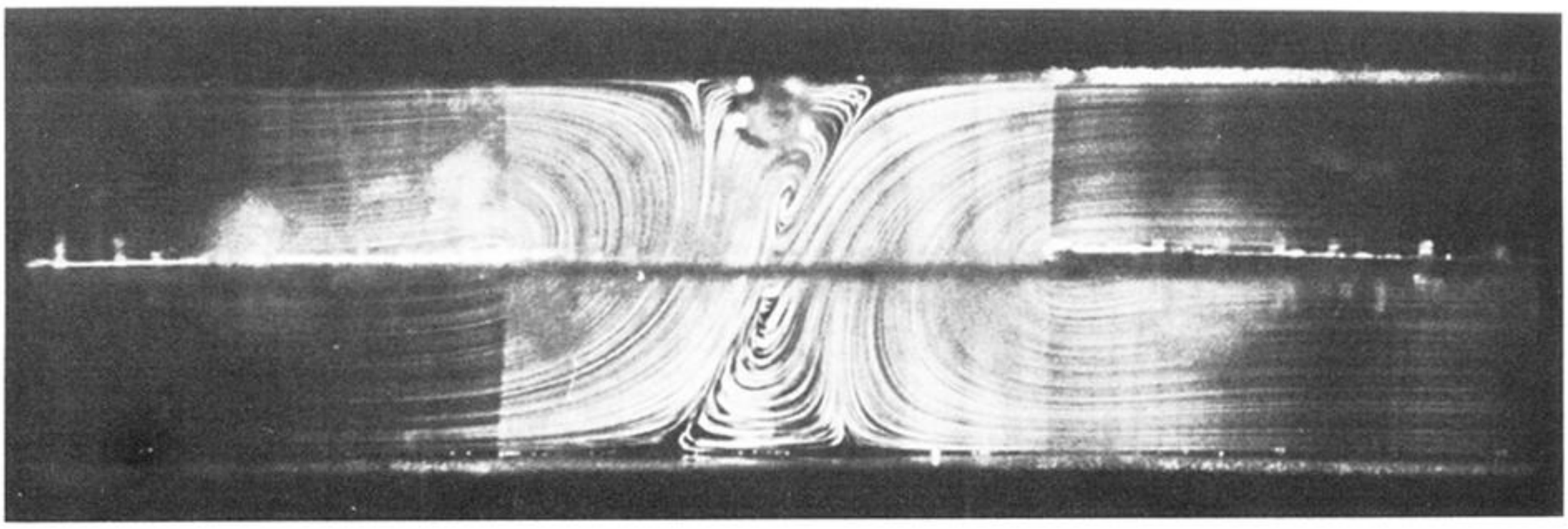

(*e*) $R = 25,\ W = 0$

FIGURE 12. Flow in the medium-gap geometry (1*b*): Newtonian; equal flow rates in all arms.

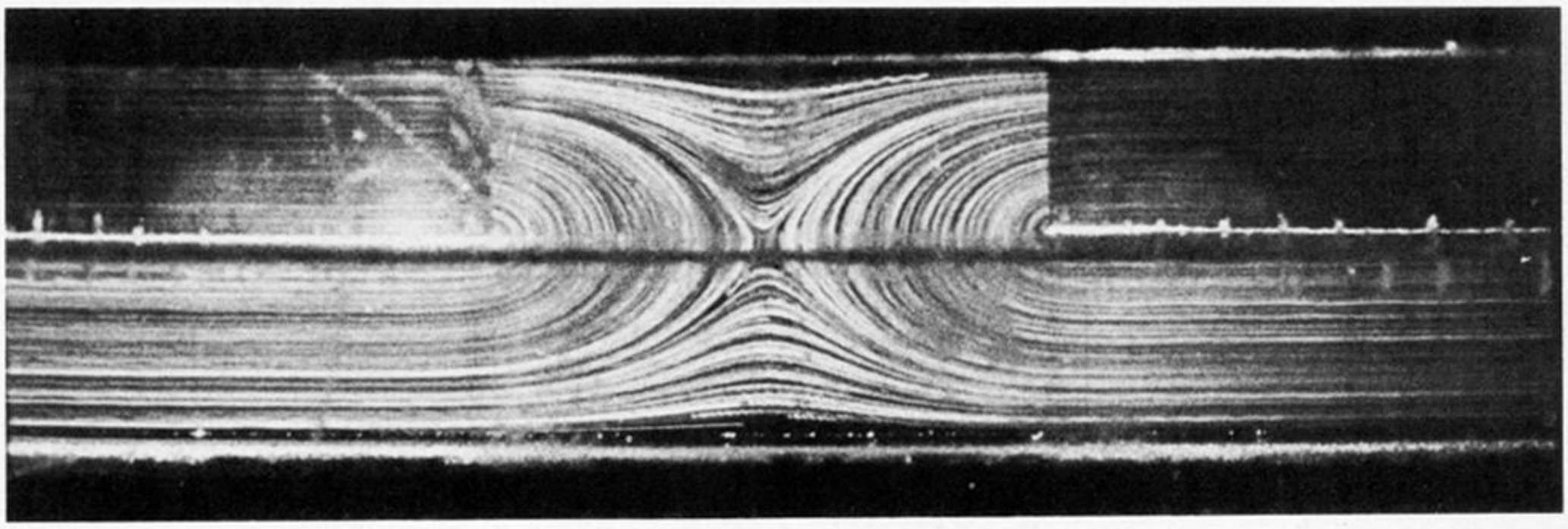

(*a*) $R = \quad 5,\ W = 0.11$

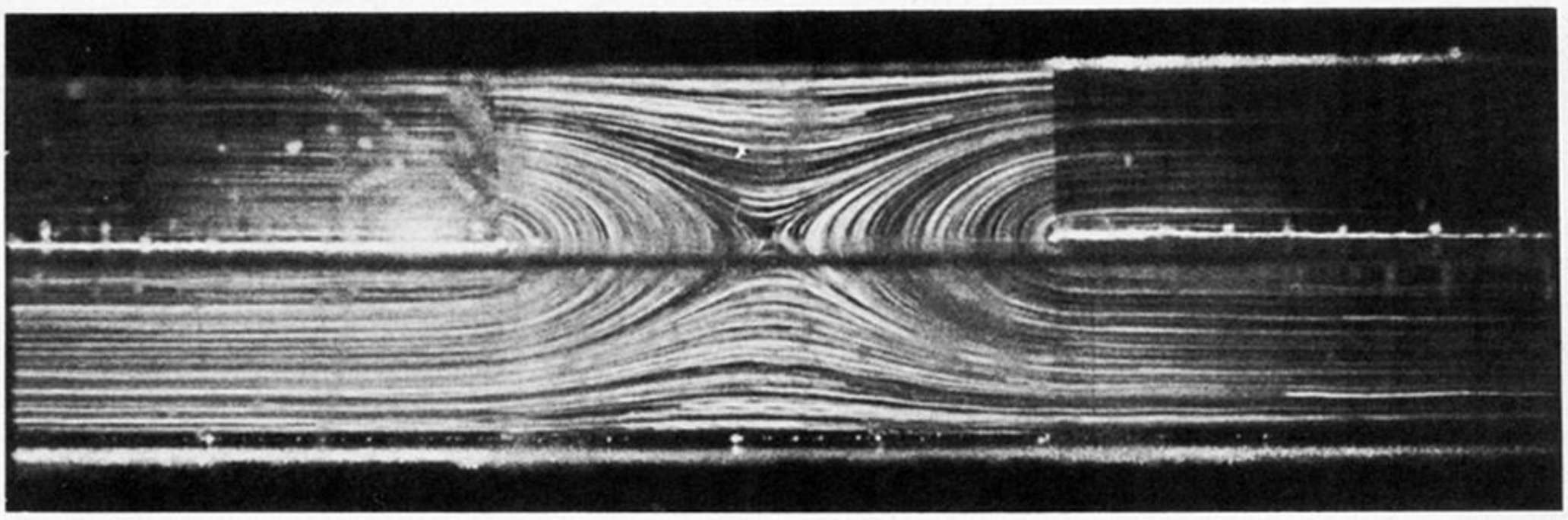

(*b*) $R = 10,\ W = 0.21$

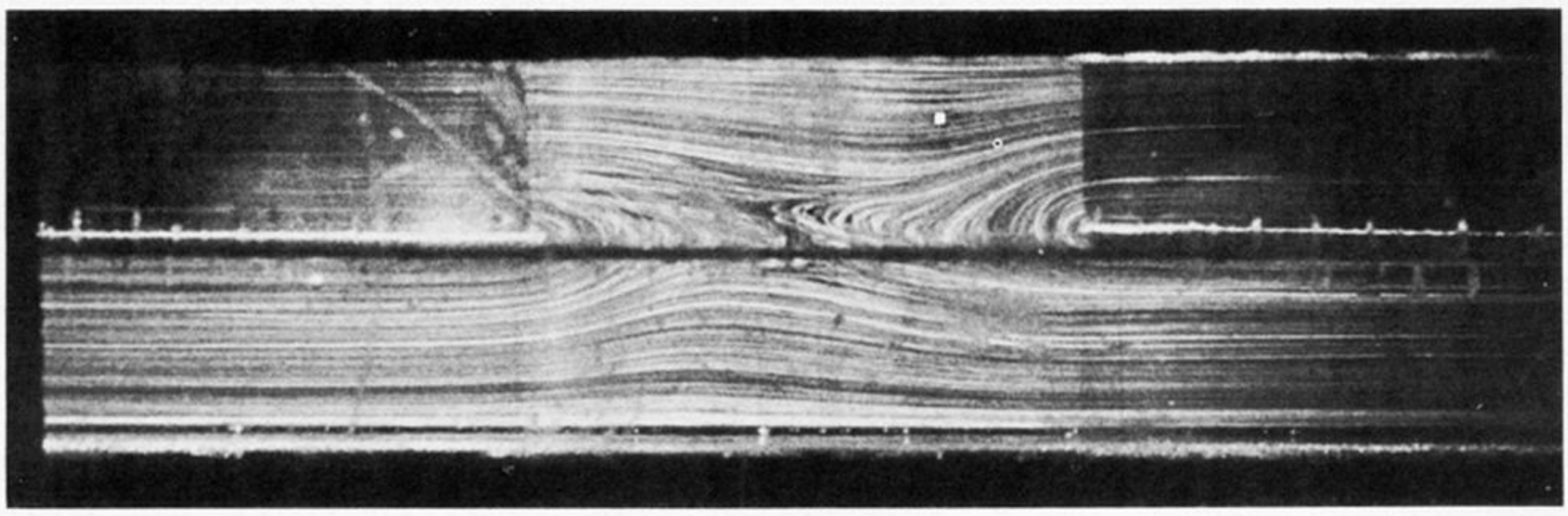

(*c*) $R = 15,\ W = 0.32$

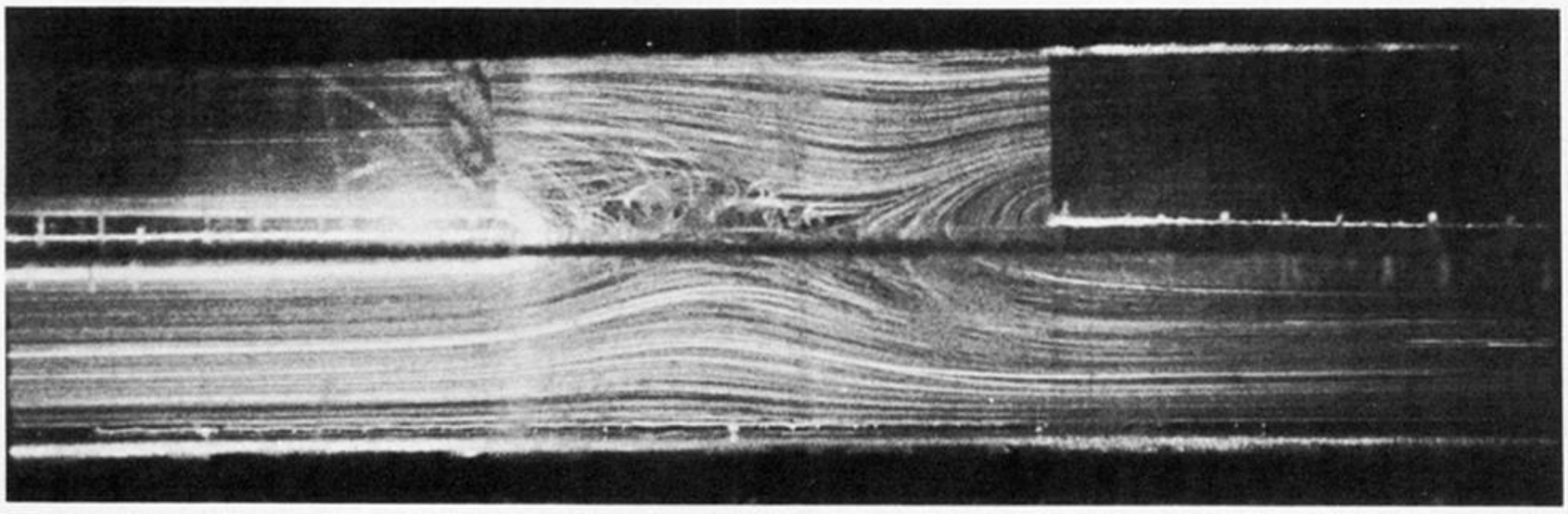

(*d*) $R = 25,\ W = 0.53$

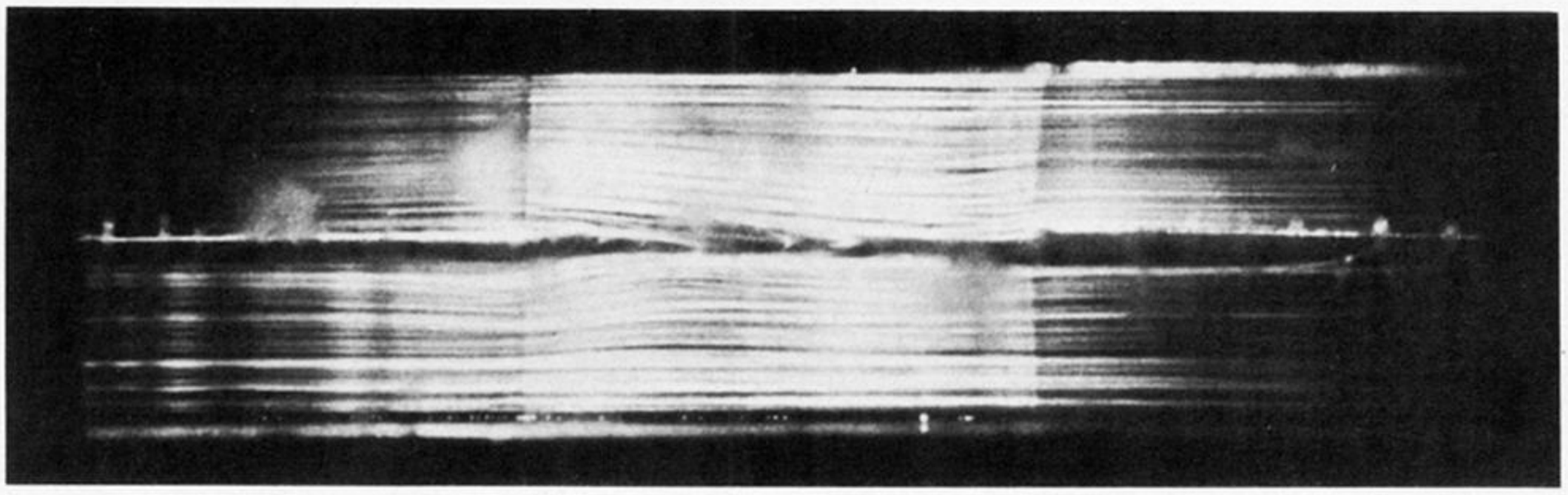

(*e*) $R = \quad 2,\ W = 0.55$

FIGURE 13. Flow in the medium-gap geometry (1*b*): (*a*)–(*d*) liquid B6; (*e*) liquid B5; equal flow rates in all arms.

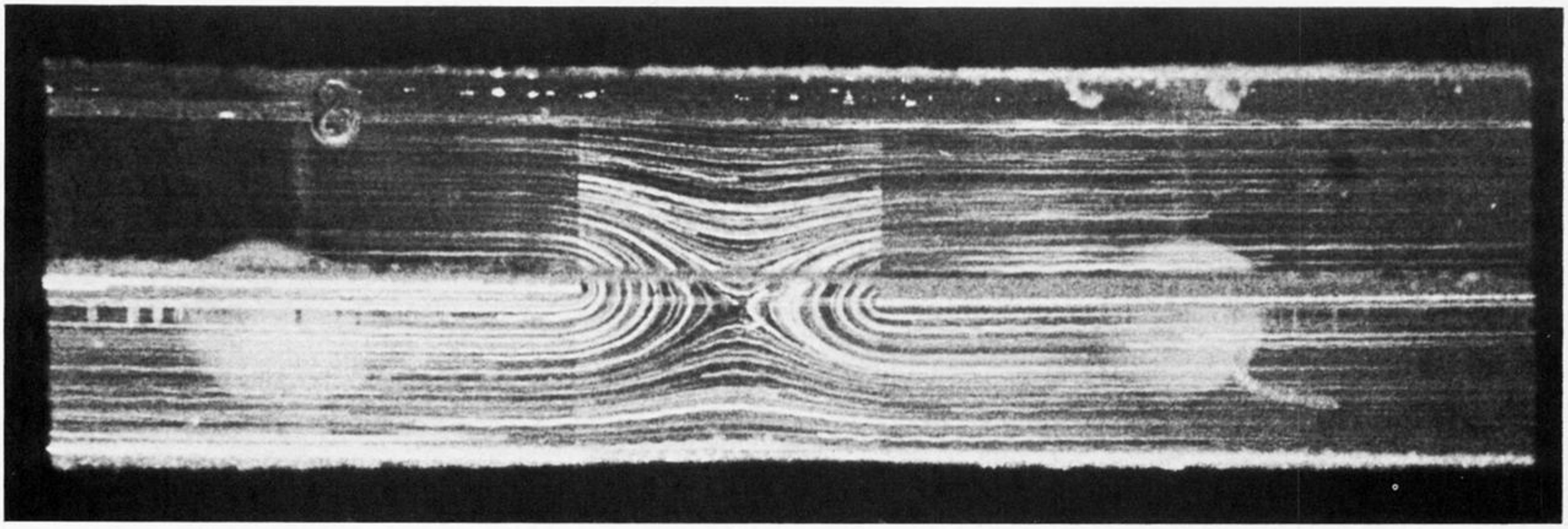

(*a*) $R = 2,\ W = 0$

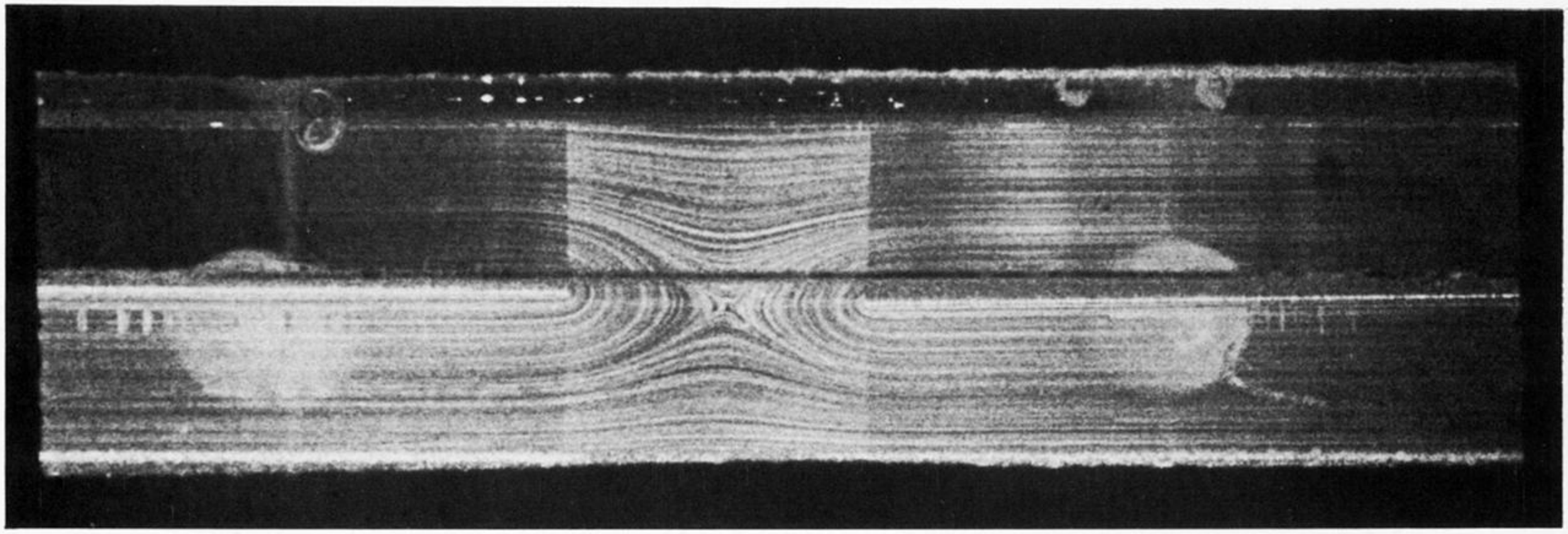

(*b*) $R = 4,\ W = 0$

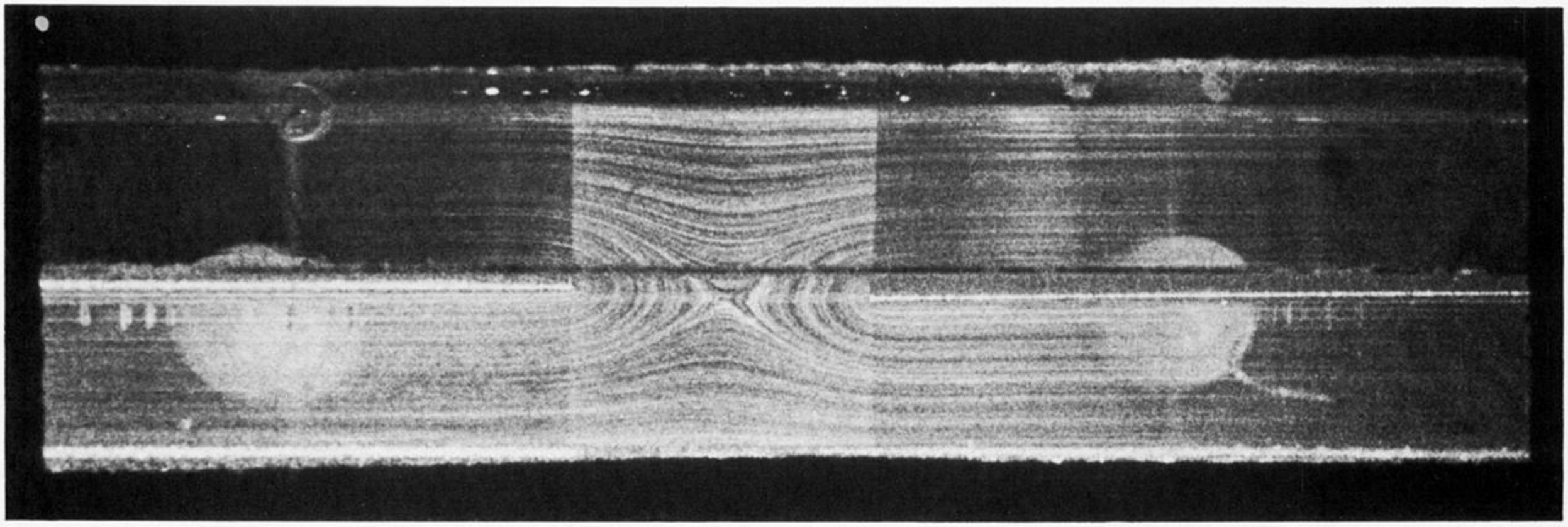

(*c*) $R = 8,\ W = 0$

FIGURE 15. Flow in the narrow-gap geometry (1*c*): Newtonian; equal flow rates in all arms.

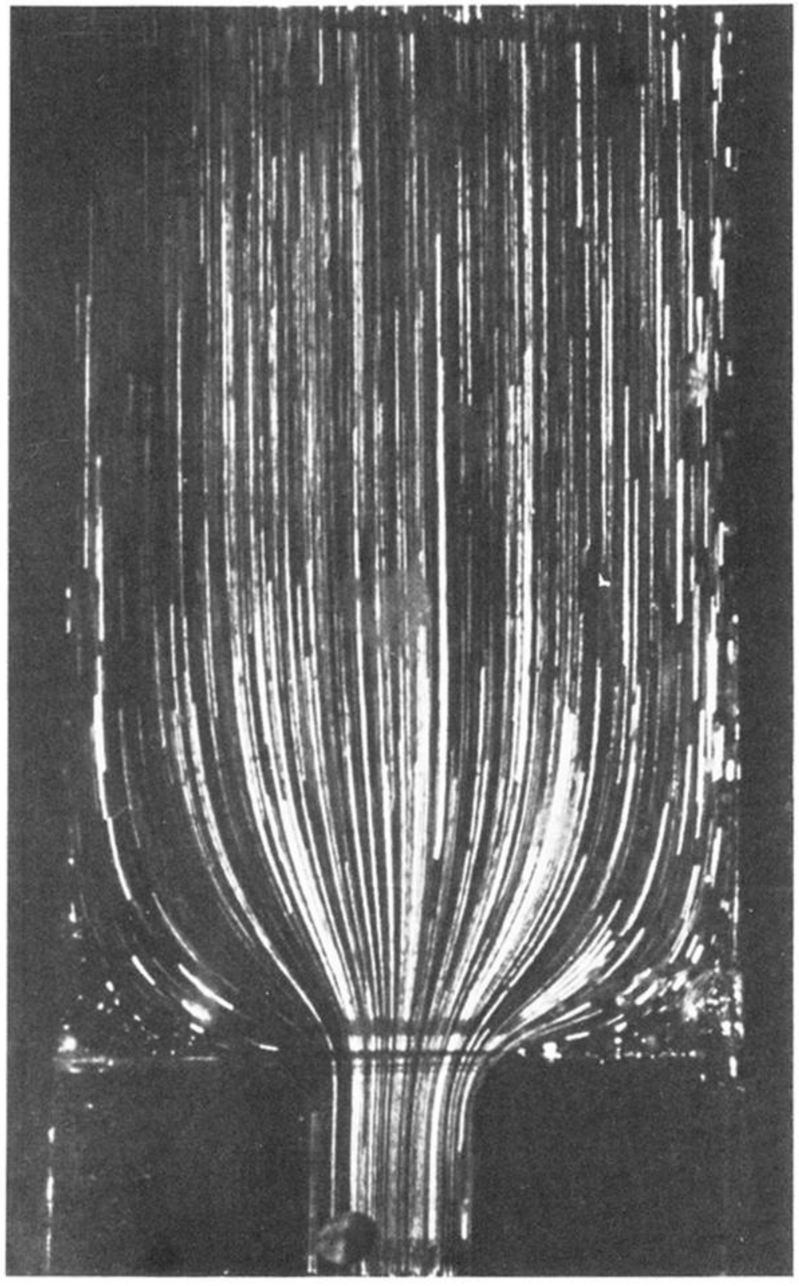

(*a*) $R = 3$, $W = 0.01$,

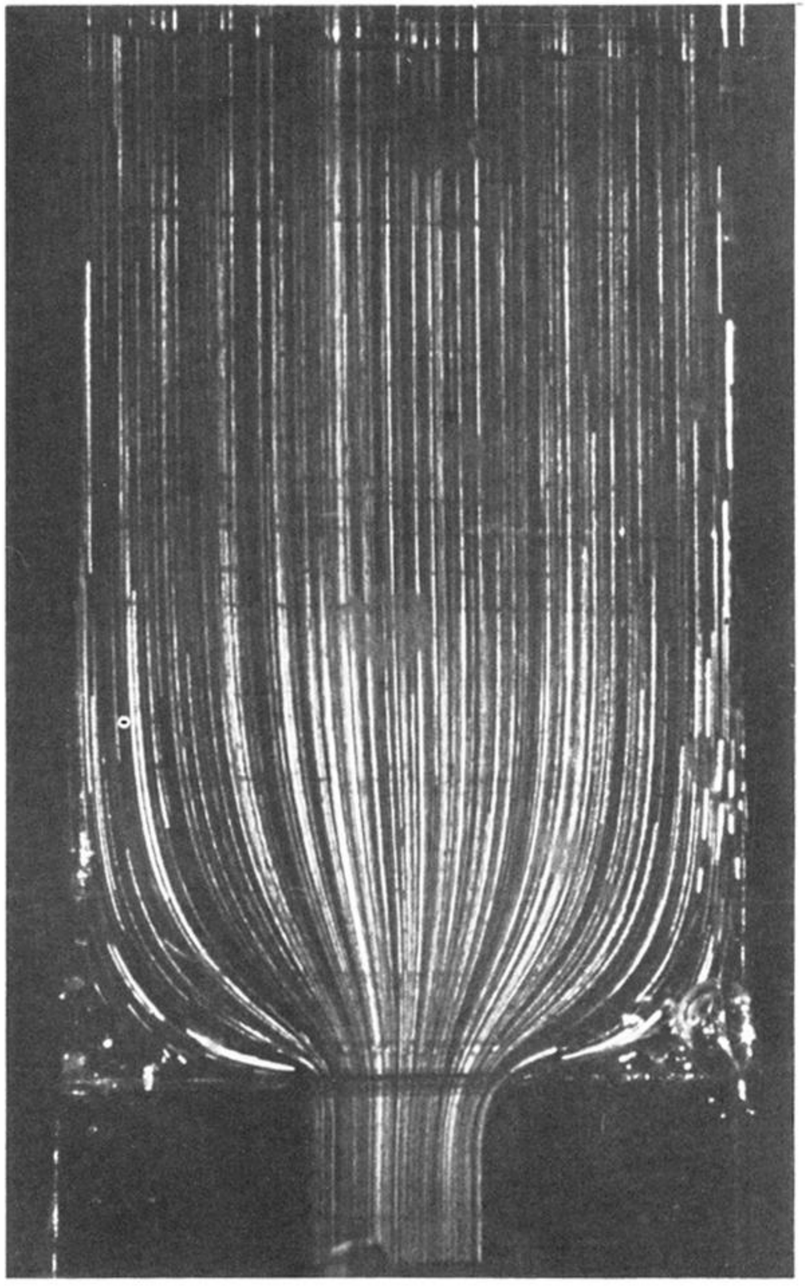

(*b*) $R = 0.04$, $W = 0.04$

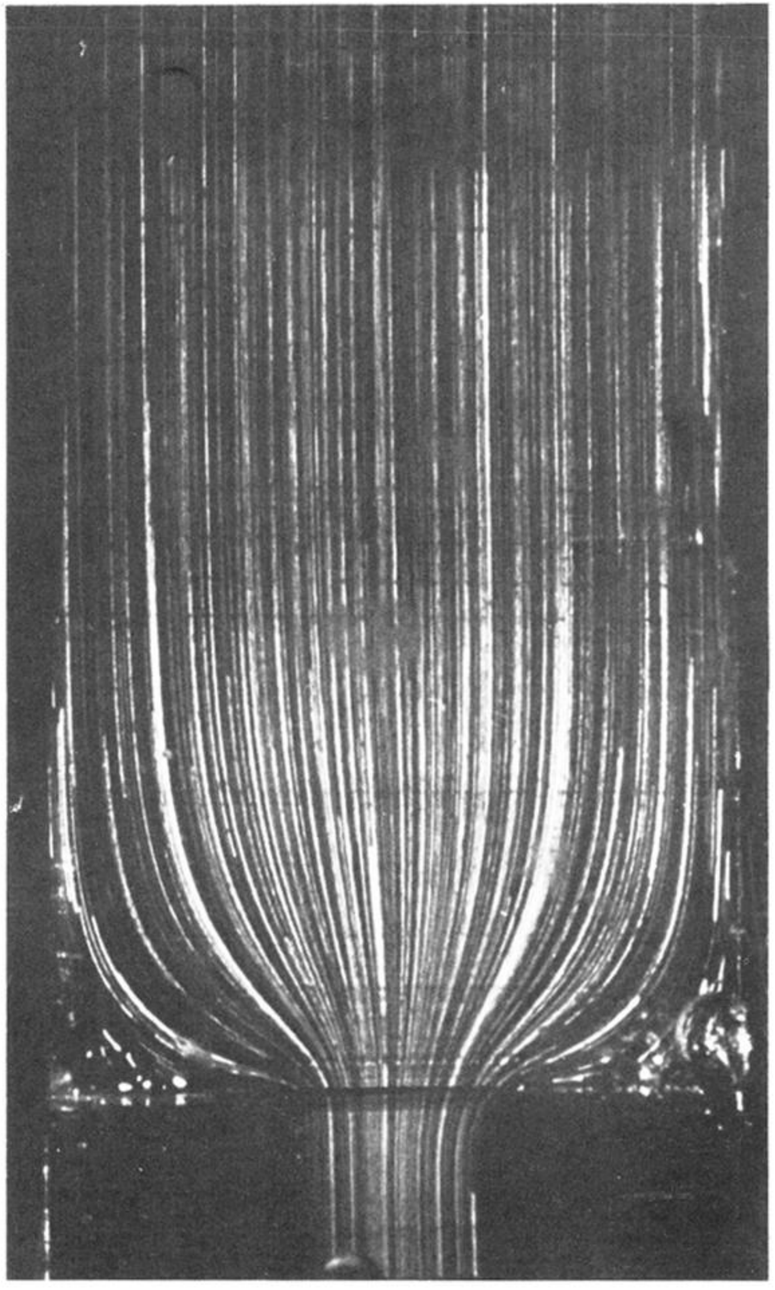

(*c*) $R = 0.8$, $W = 0.53$

FIGURE 17. Flow in the planar contraction geometry (1*e*): Newtonian.

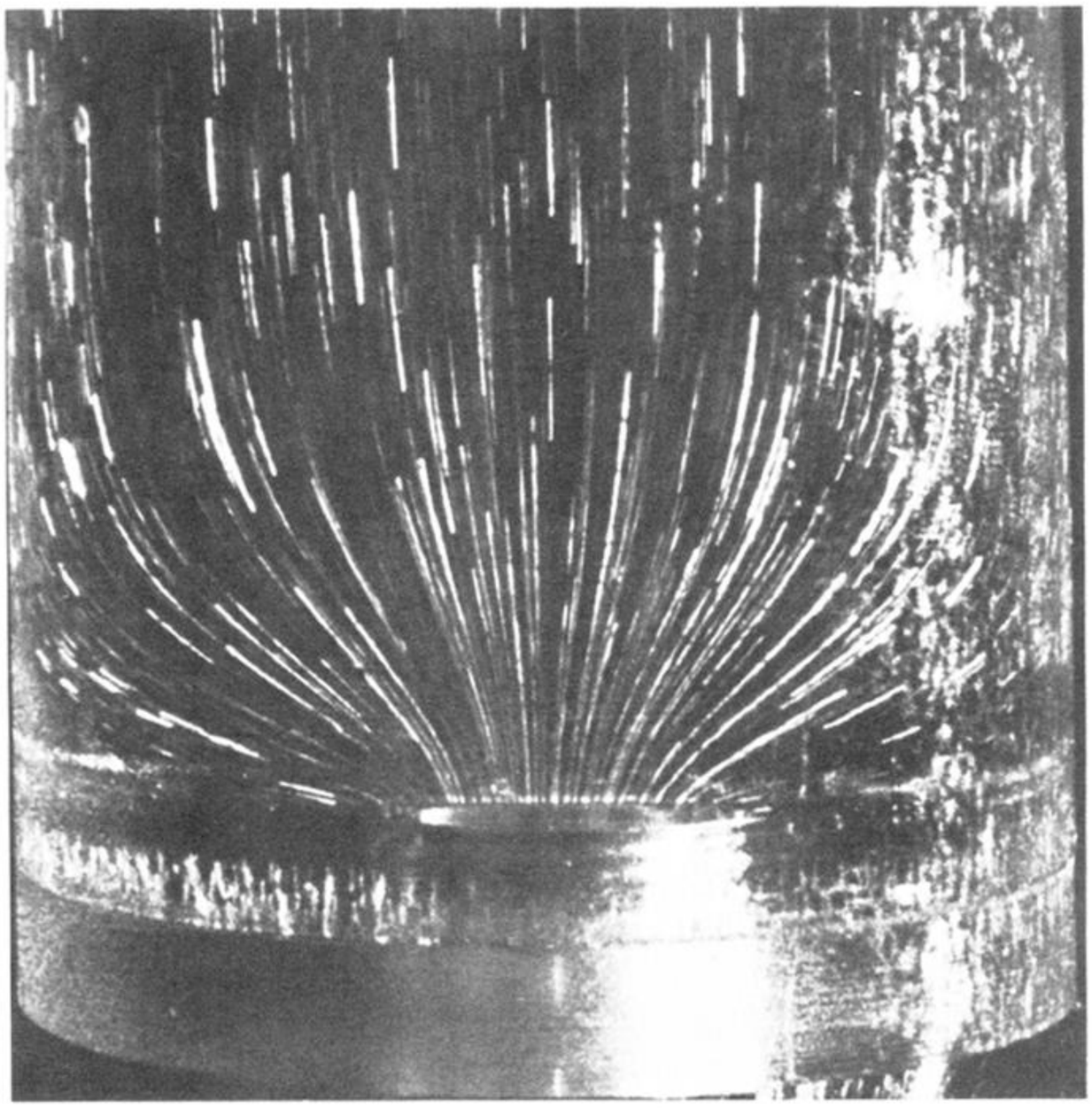

(*a*) $R = 0.02,\ W = 0$

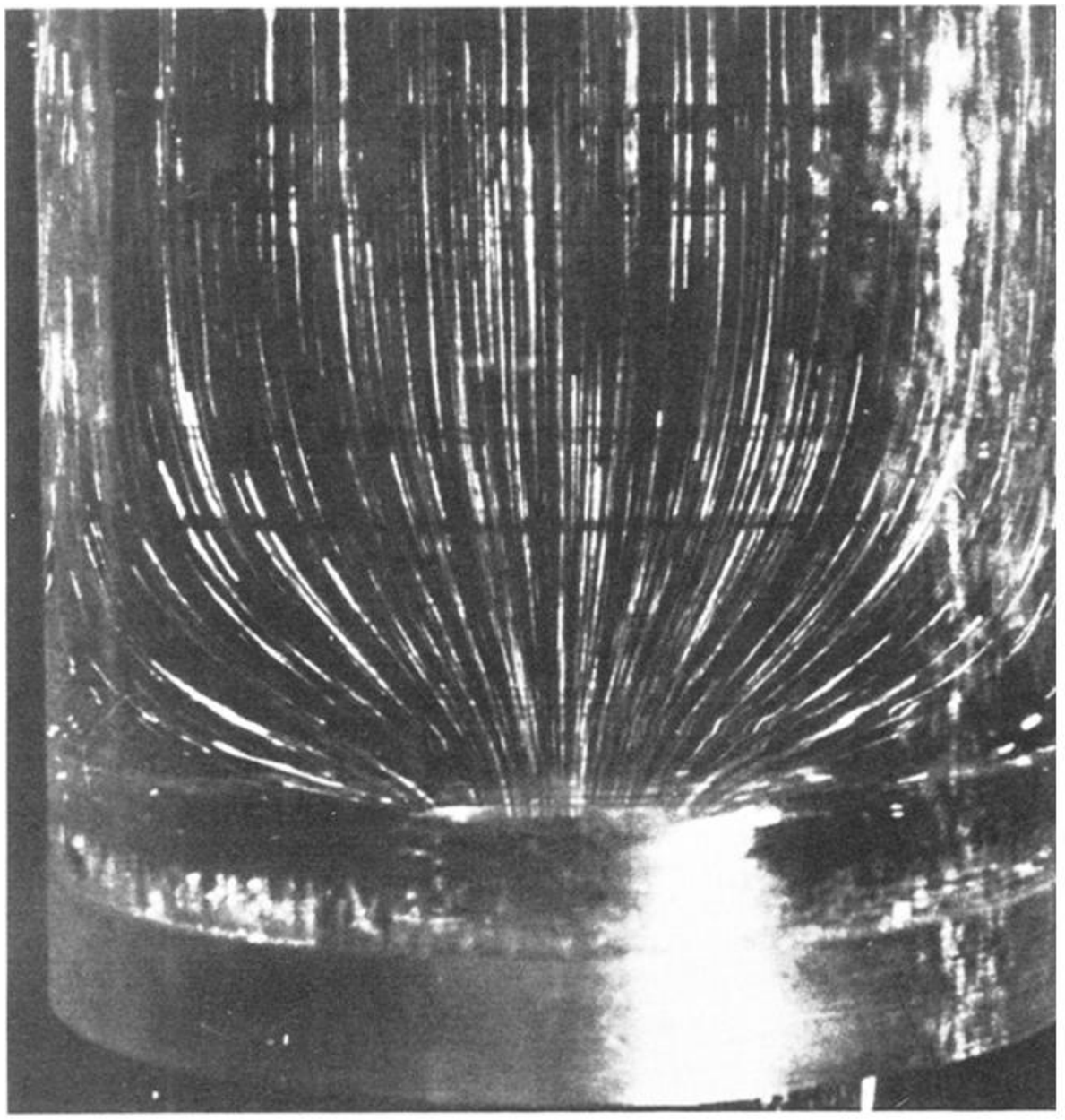

(*b*) $R = 0.06,\ W = 0$

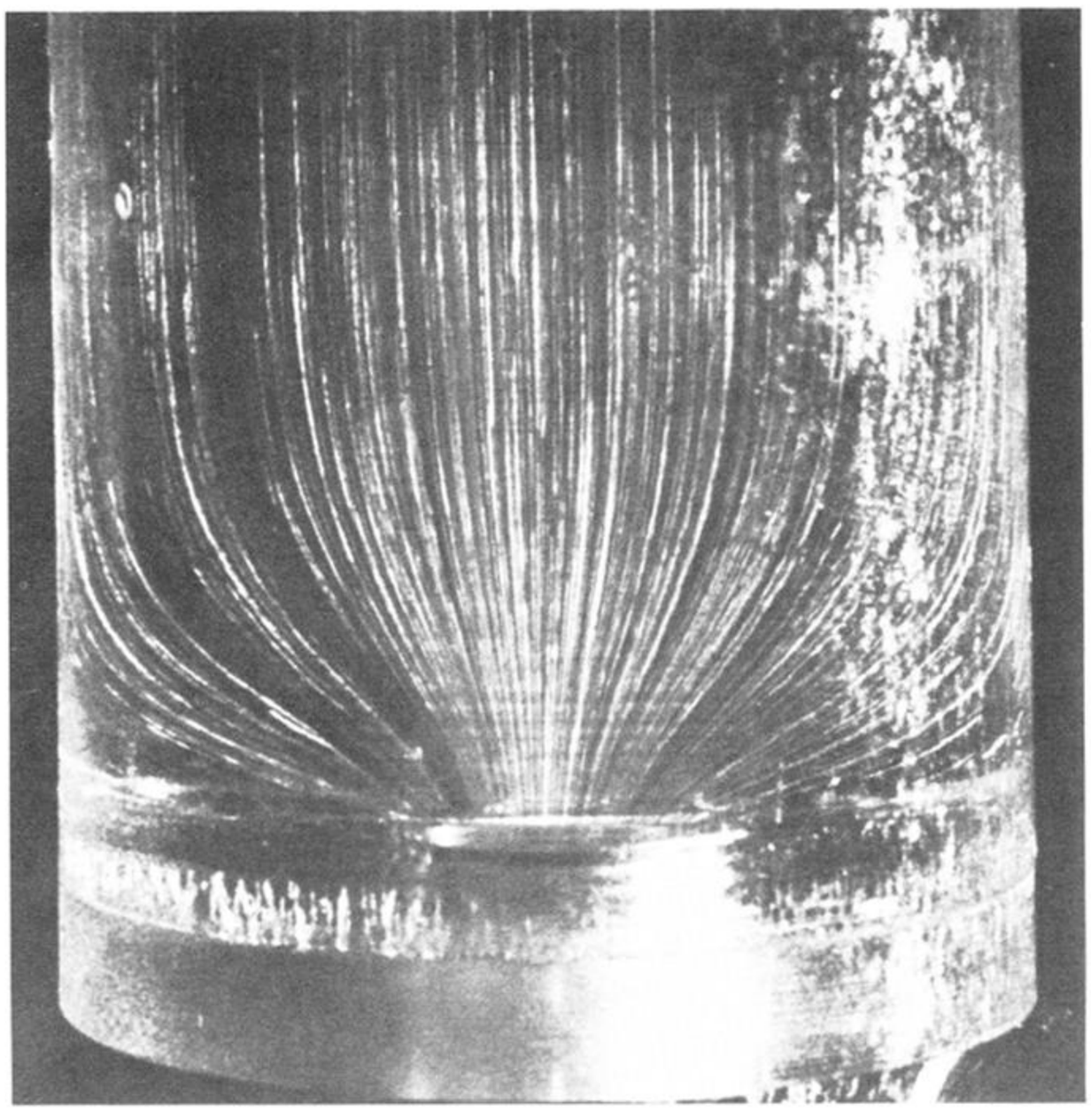

(*c*) $R = 0.09,\ W = 0$

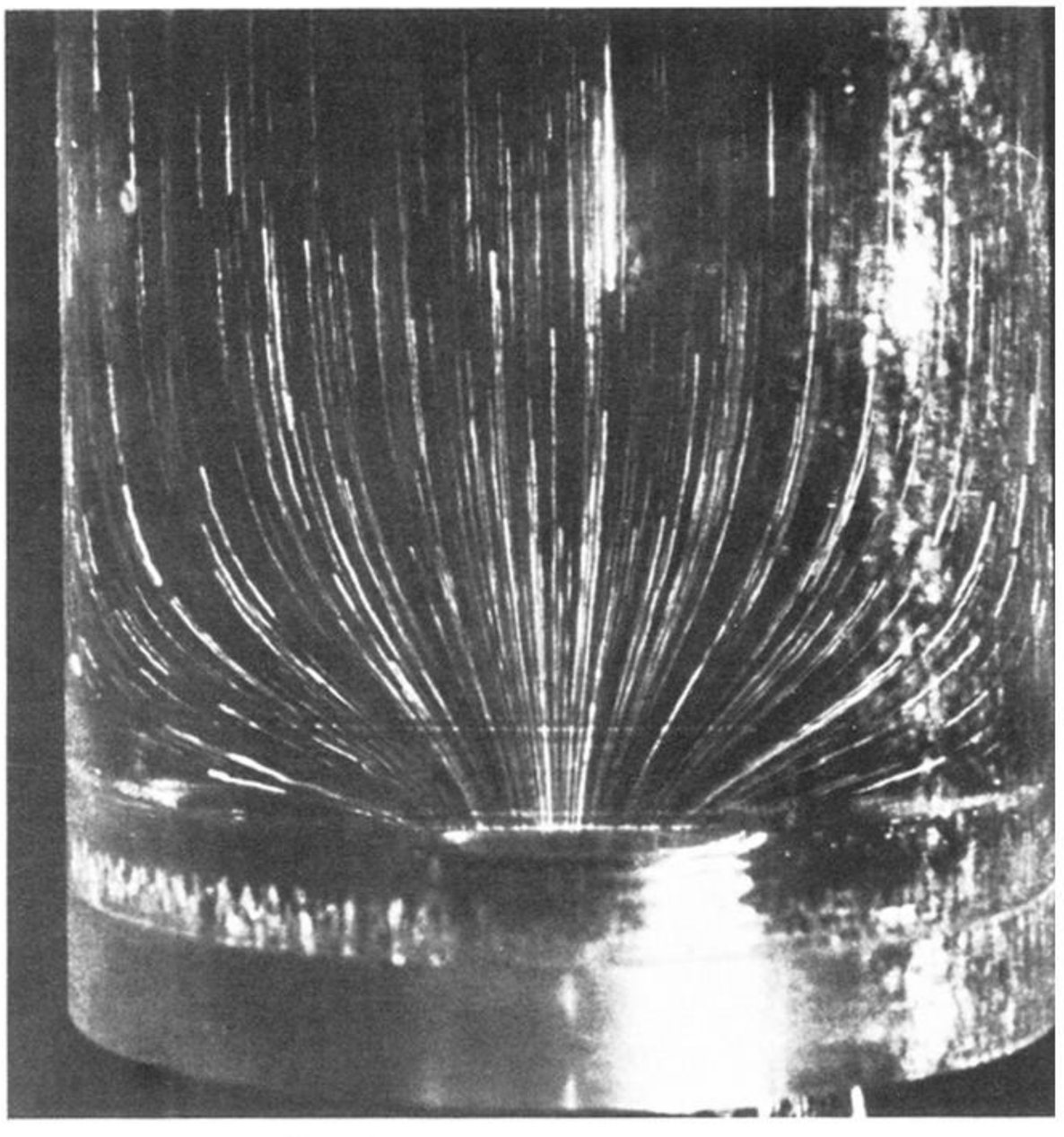

(*d*) $R = 0.13,\ W = 0$

FIGURE 19. Flow in the circular contraction geometry (1*g*): Newtonian.

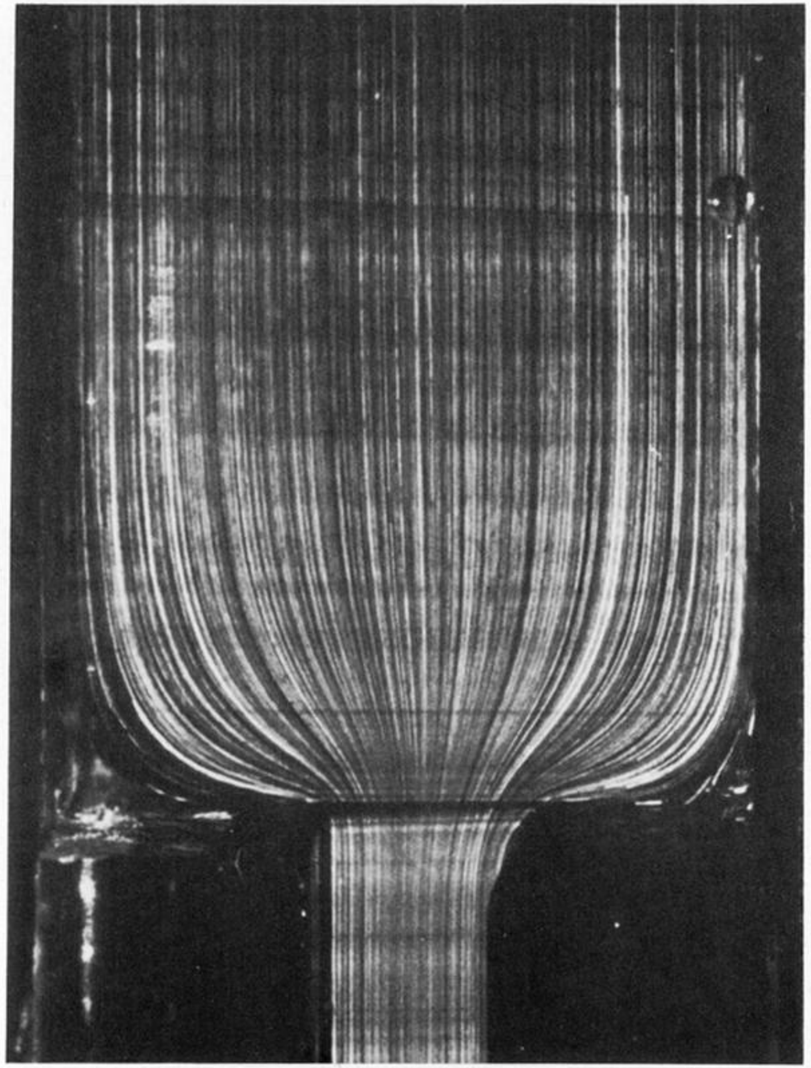

(*a*) $R = 3$, $W = 0.01$,

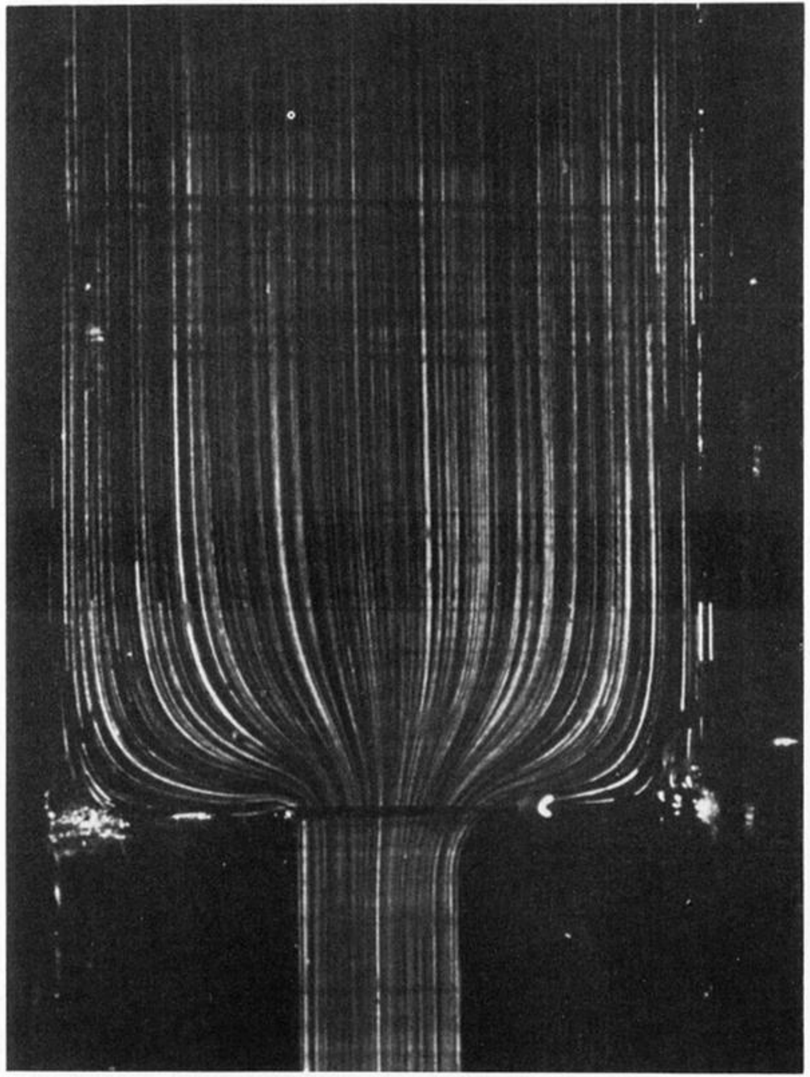

(*b*) $R = 0.04$, $W = 0.04$

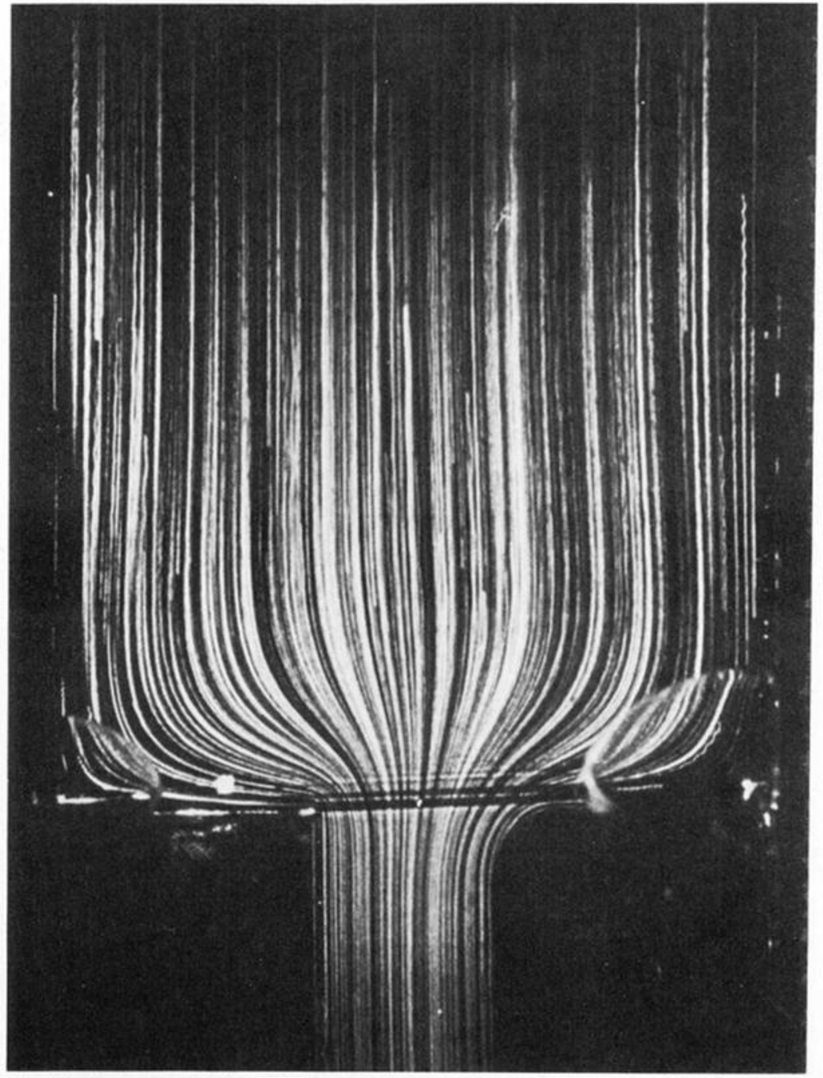

(*c*) $R = 0.8$, $W = 0.53$

FIGURE 20. Flow in the planar contraction geometry (1*e*): (*a*) liquid B9; (*b*) liquid B10; (*c*) liquid B8.

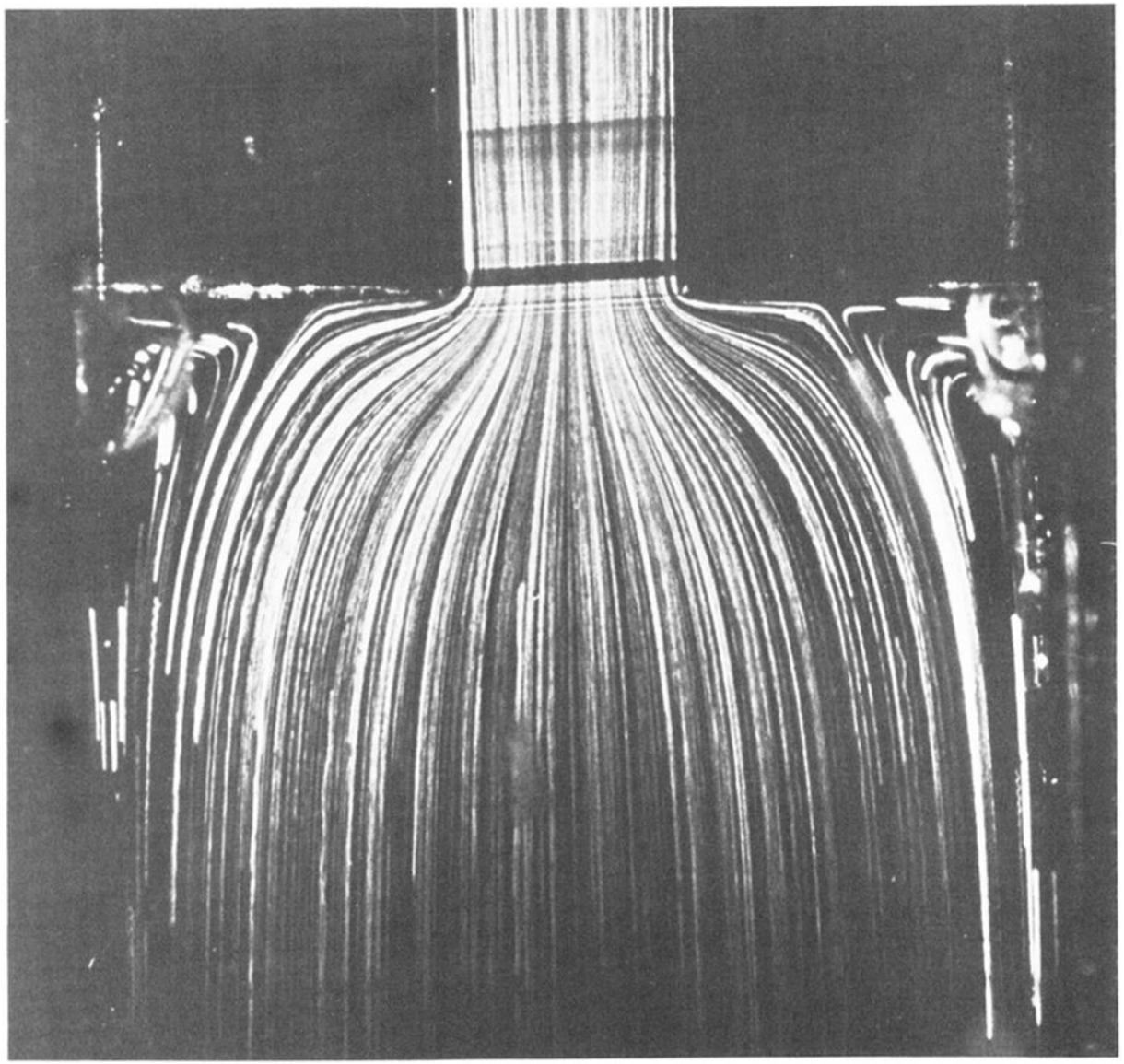

(*a*) $R = 0.64$, $W = 0.43$

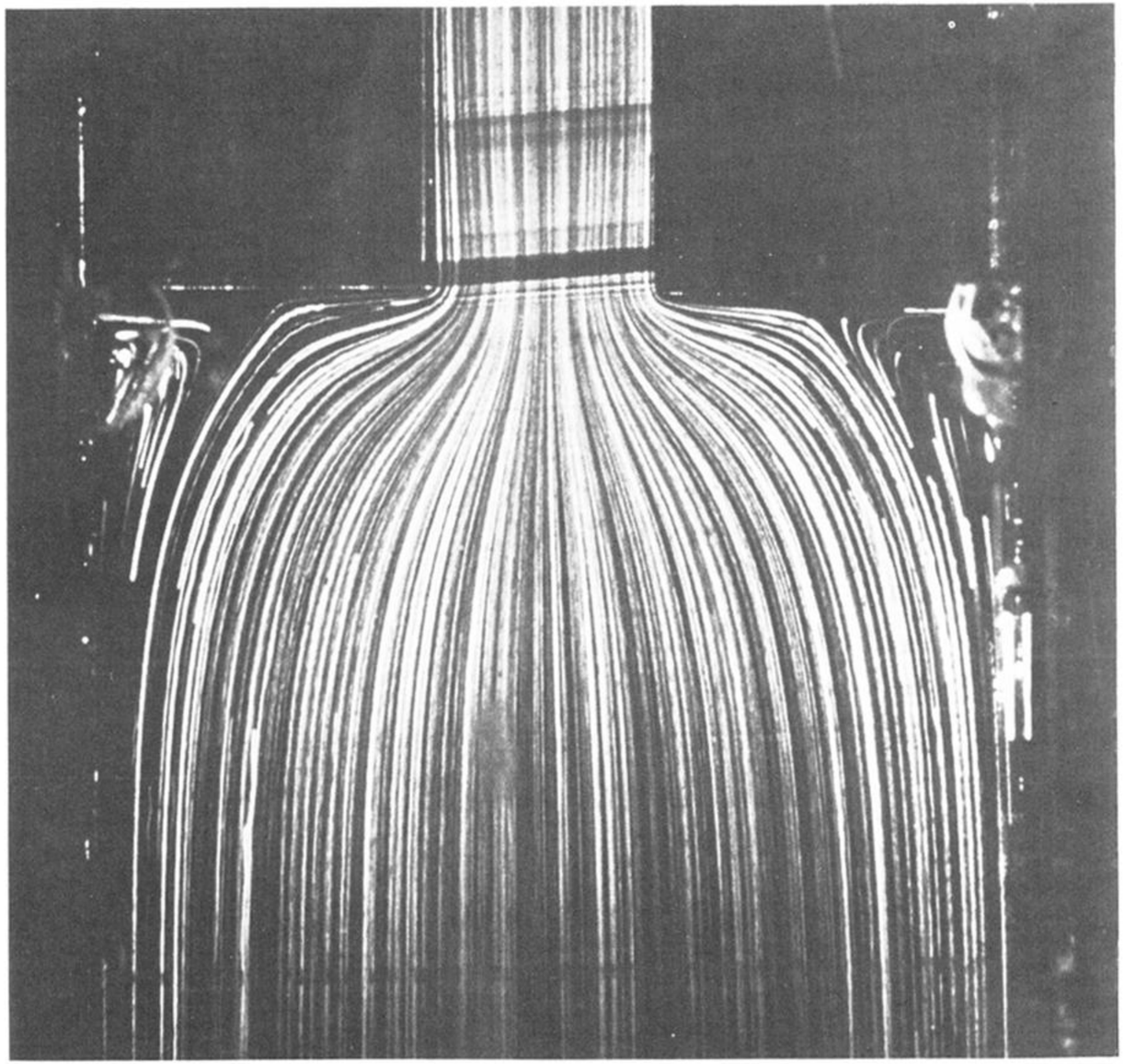

(*b*) $R = 0.8$, $W = 0.53$

FIGURE 22. Flow in the planar *expansion* geometry (1*d*): liquid B8.

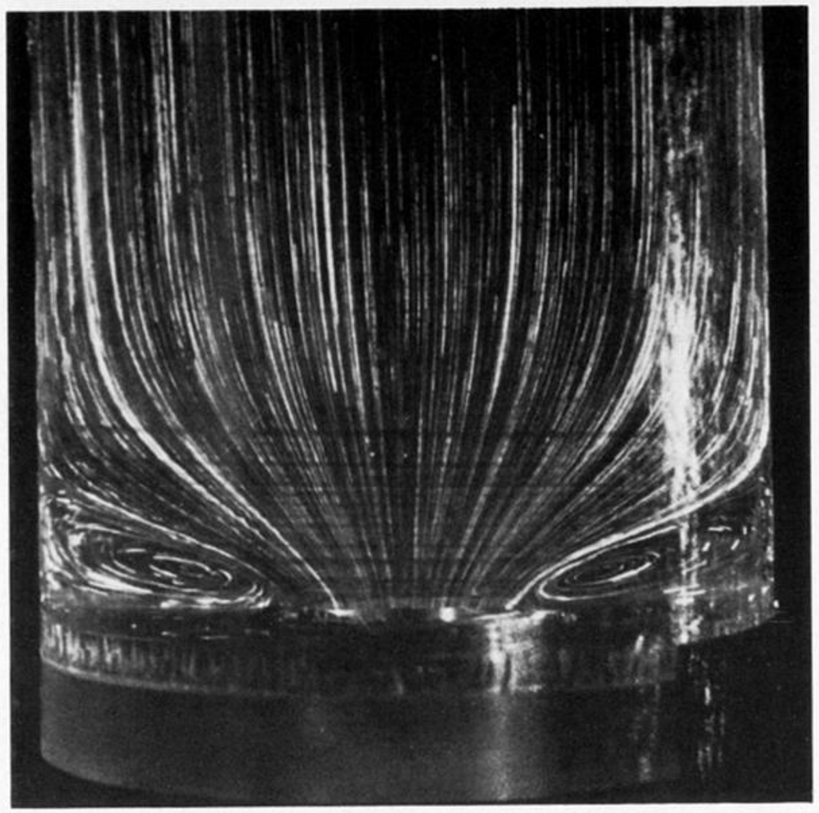

(*a*) $R = 0.08$, $W = 0.11$

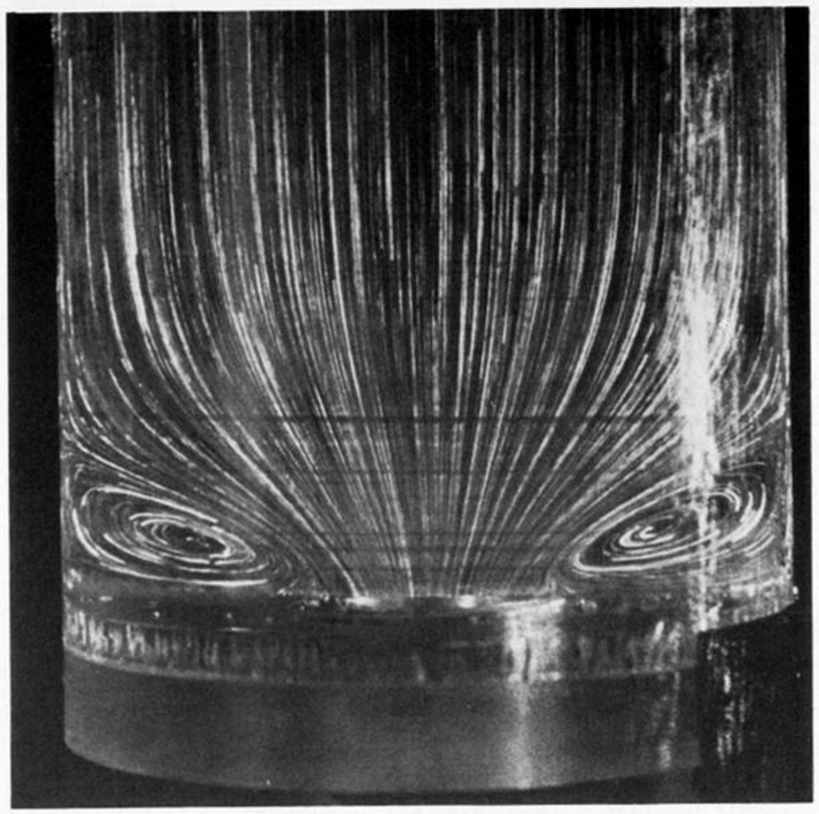

(*b*) $R = 0.11$, $W = 0.15$

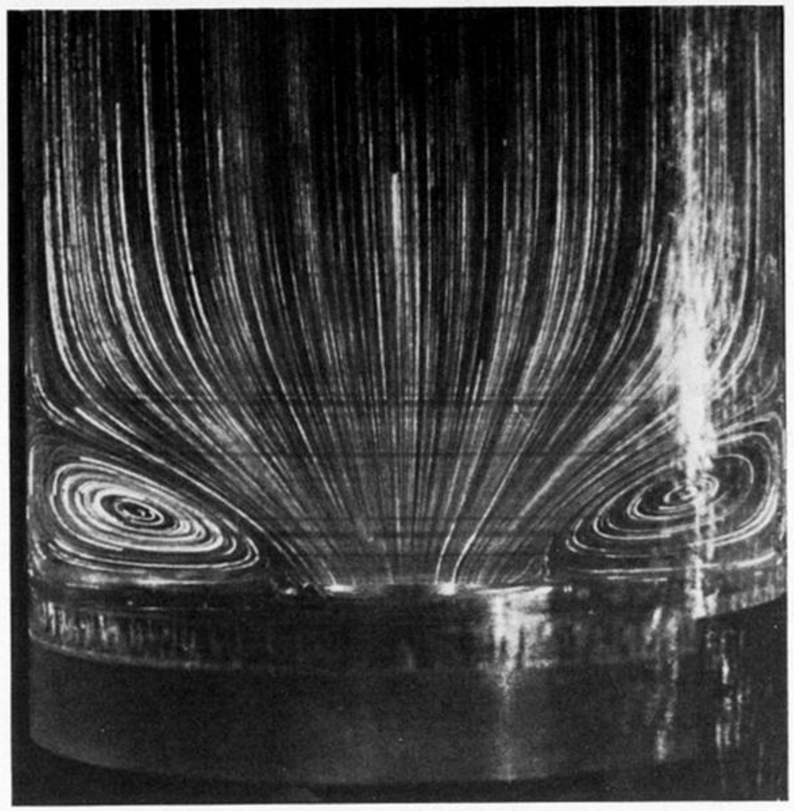

(*c*) $R = 0.15$, $W = 0.22$

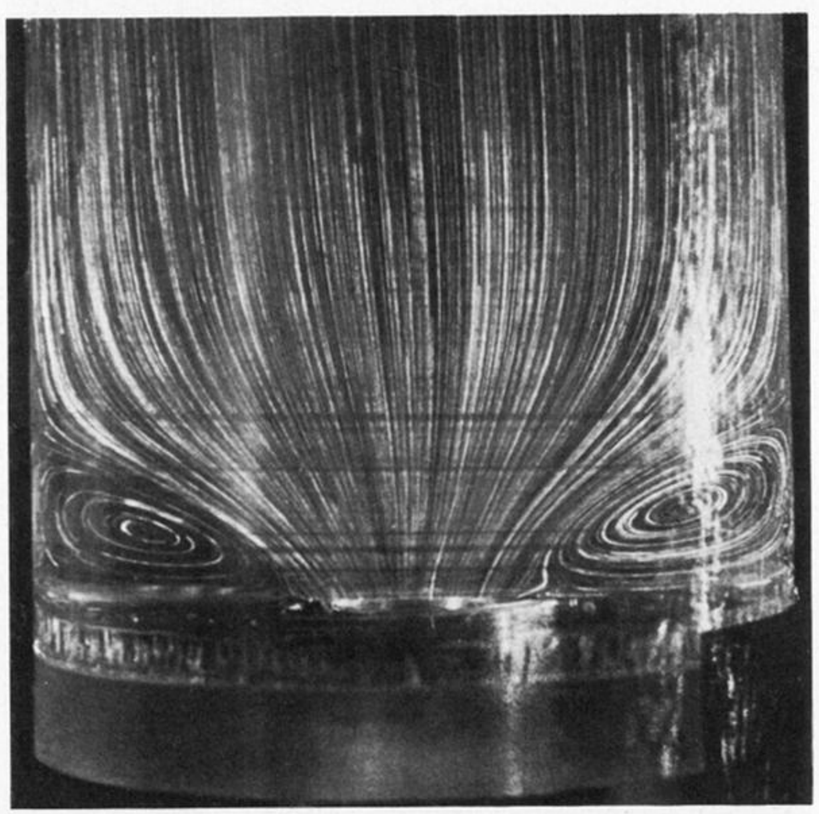

(*d*) $R = 0.17$, $W = 0.24$

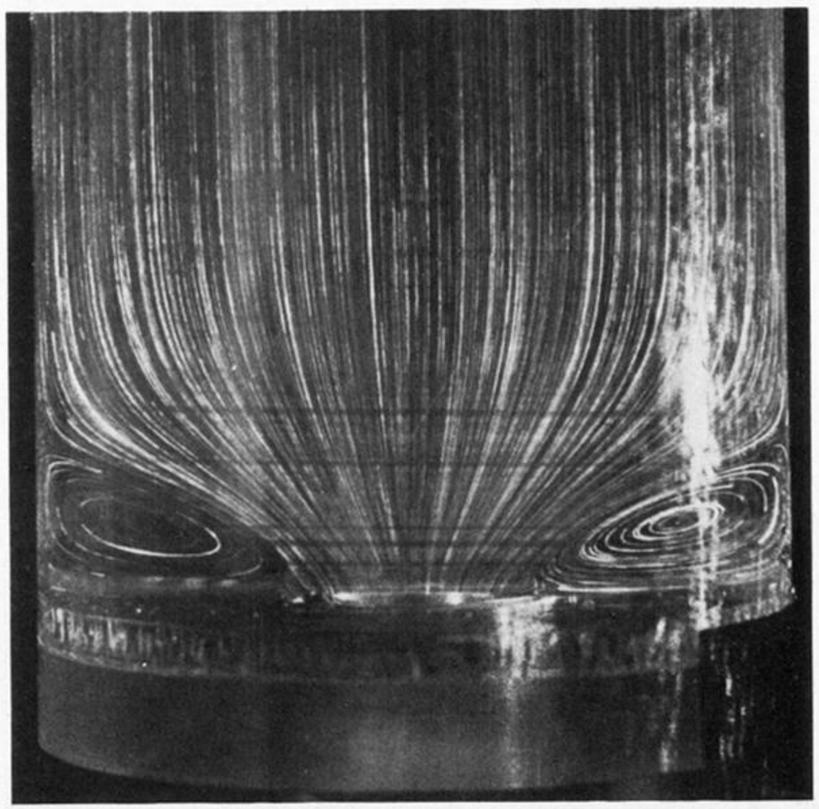

(*e*) $R = 0.19$, $W = 0.27$

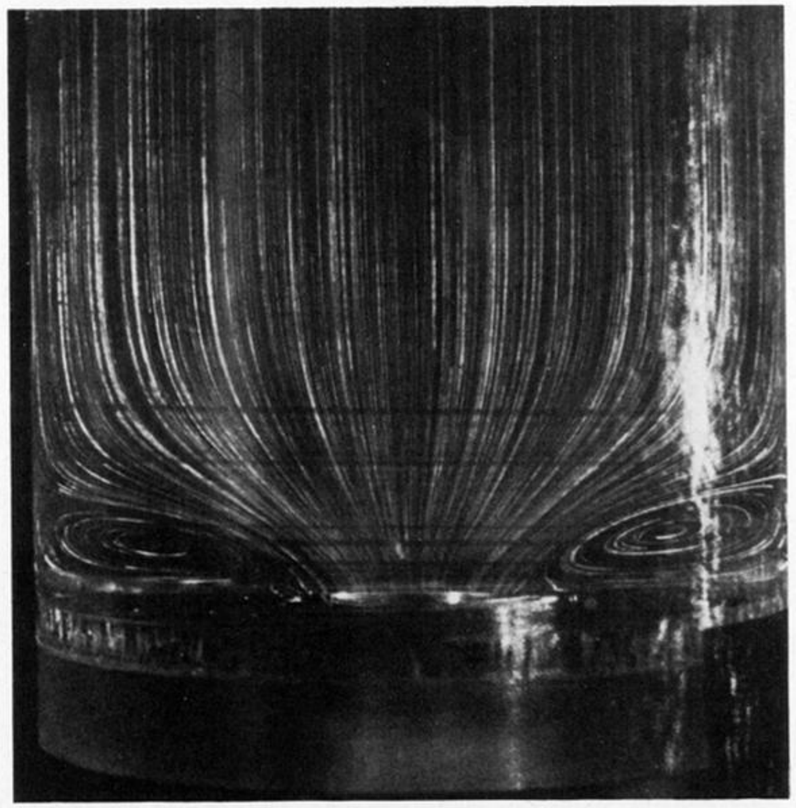

(*f*) $R = 0.21$, $W = 0.3$

FIGURE 24. Flow in the symmetrical circular contraction geometry (1*f*): liquid B10.

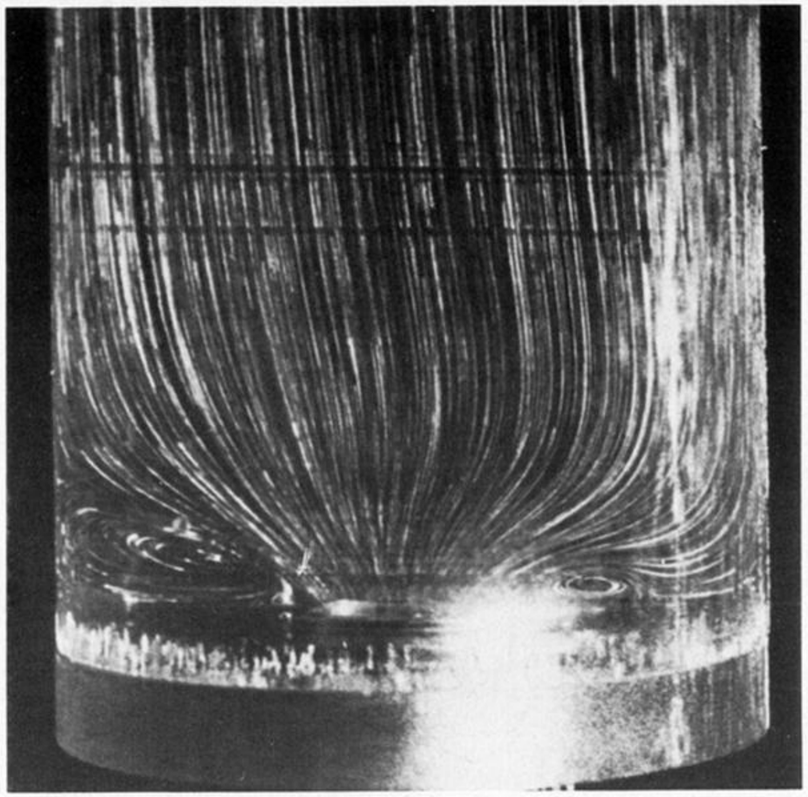

(*a*) $R = 0.08$, $W = 0.11$

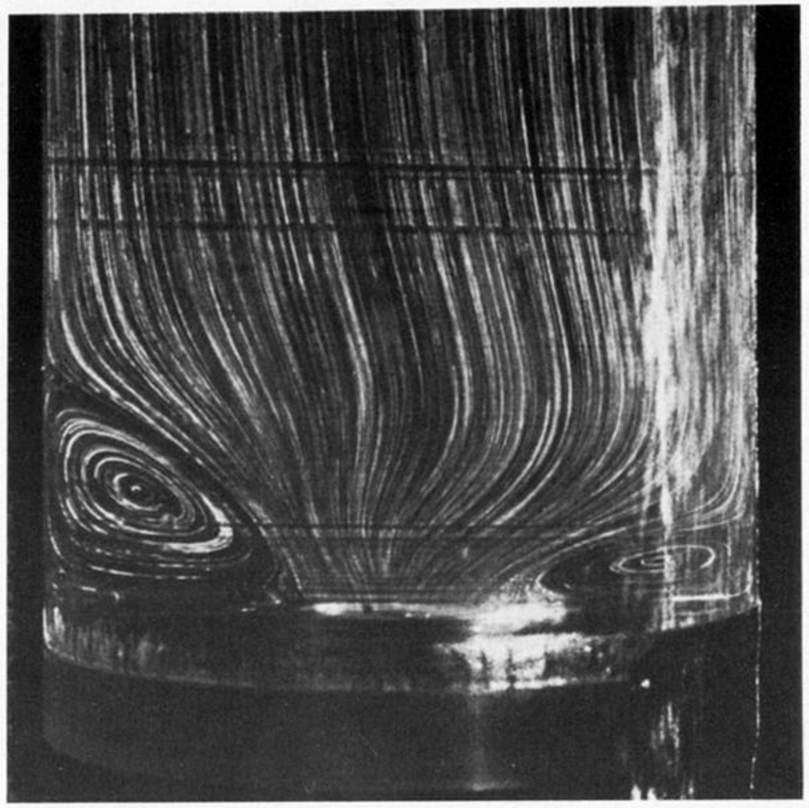

(*b*) $R = 0.13$, $W = 0.18$

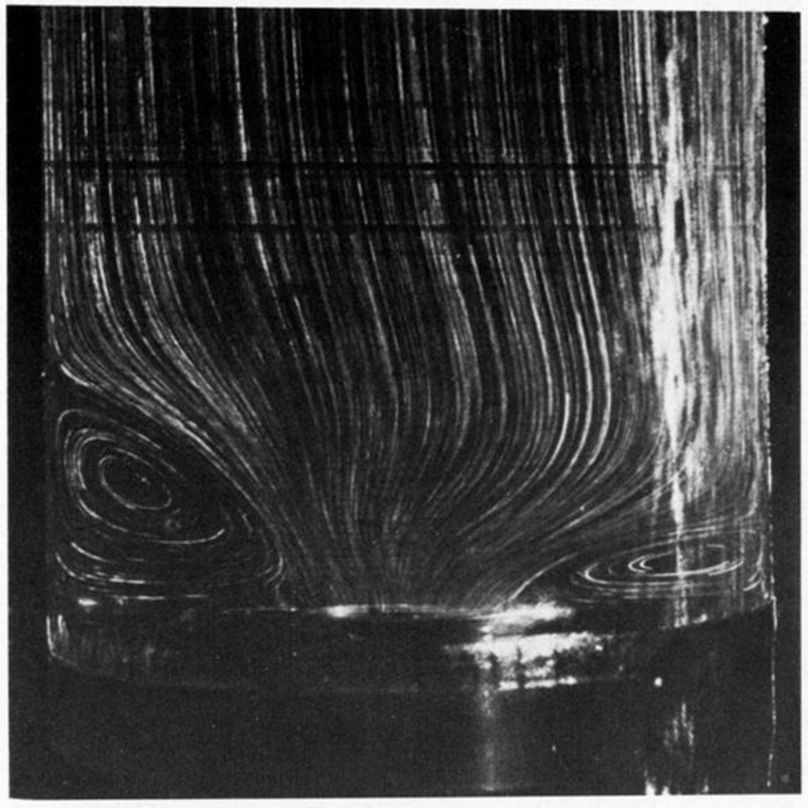

(*c*) $R = 0.15$, $W = 0.22$

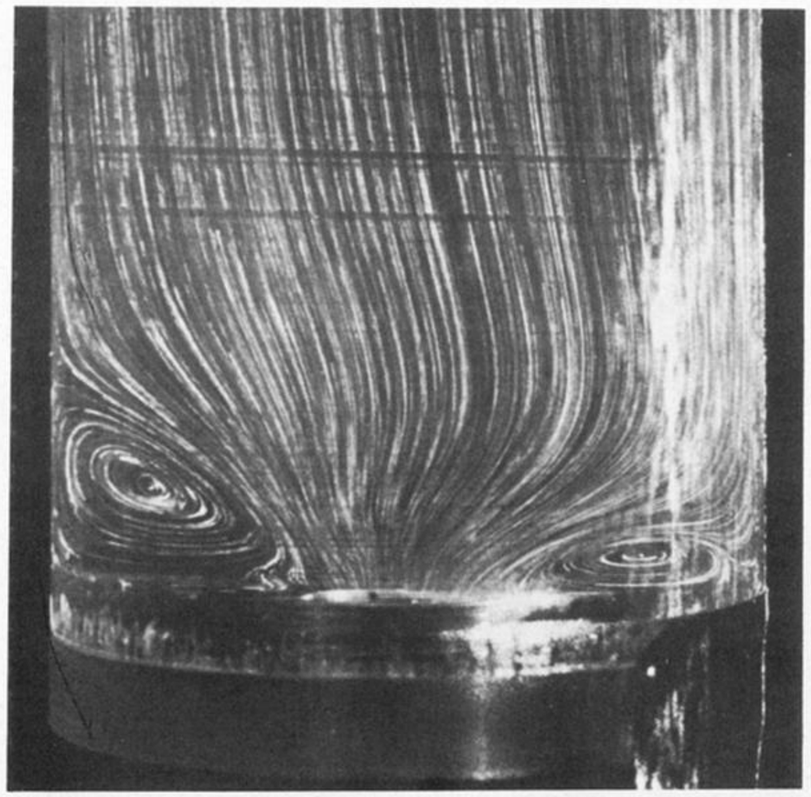

(*d*) $R = 0.17$, $W = 0.24$

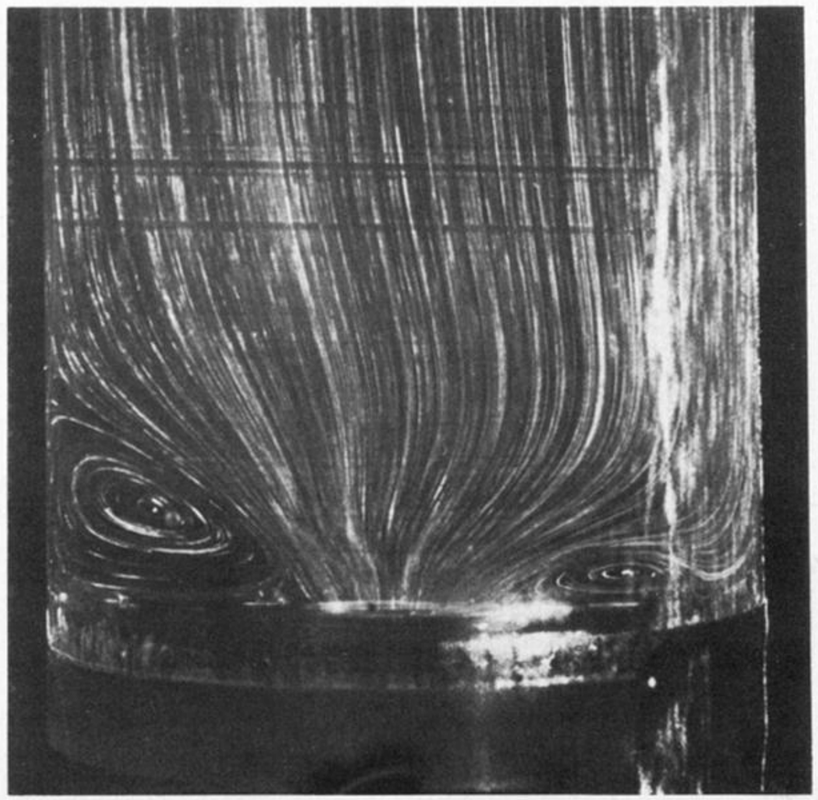

(*e*) $R = 0.19$, $W = 0.27$

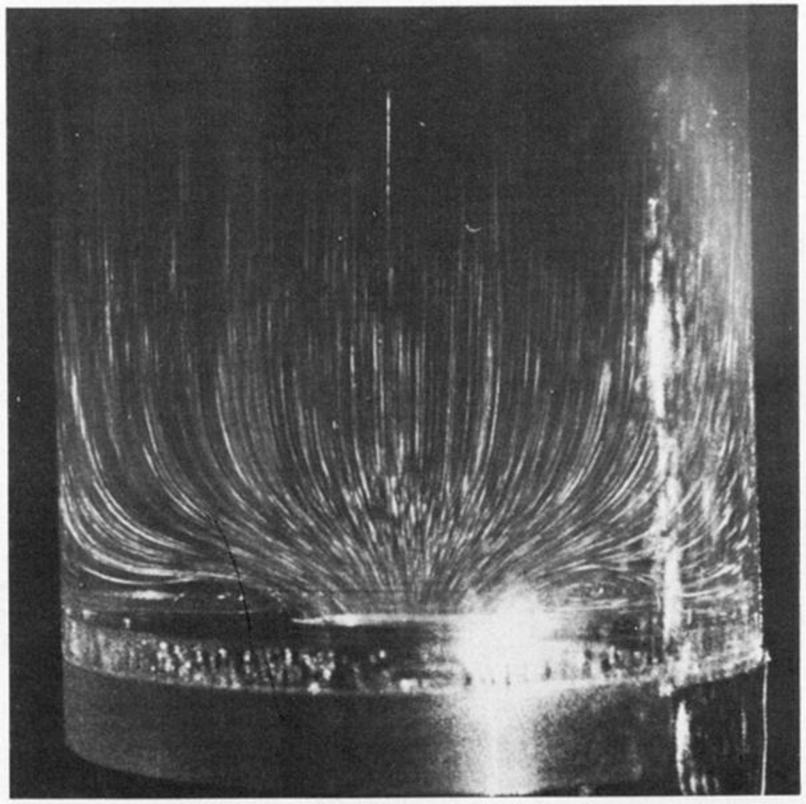

(*f*) $R = 0.19$, $W = 0.27$

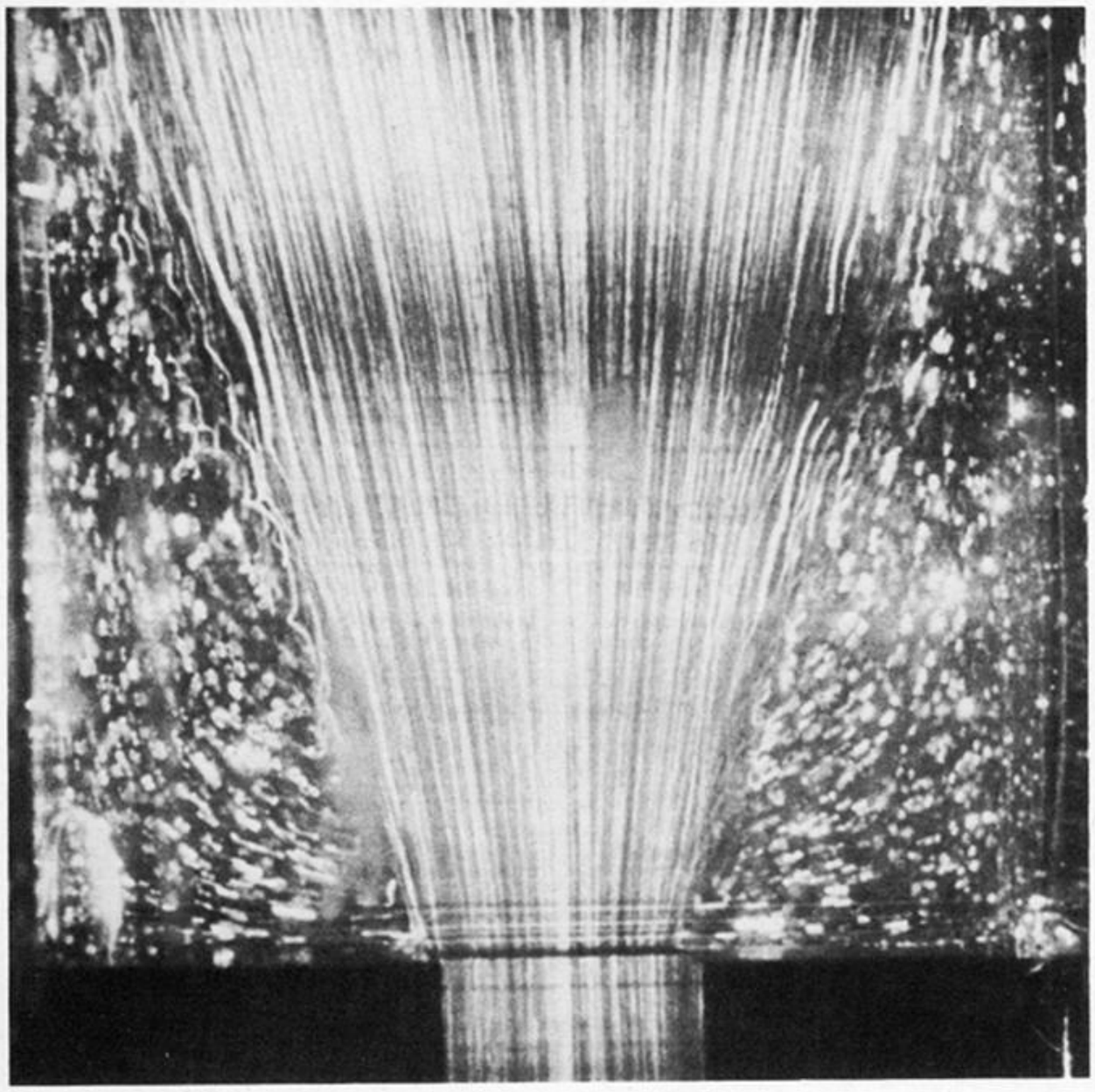

(*a*) geometry 1*d*, $Q = 0.5$ ml s^{-1}

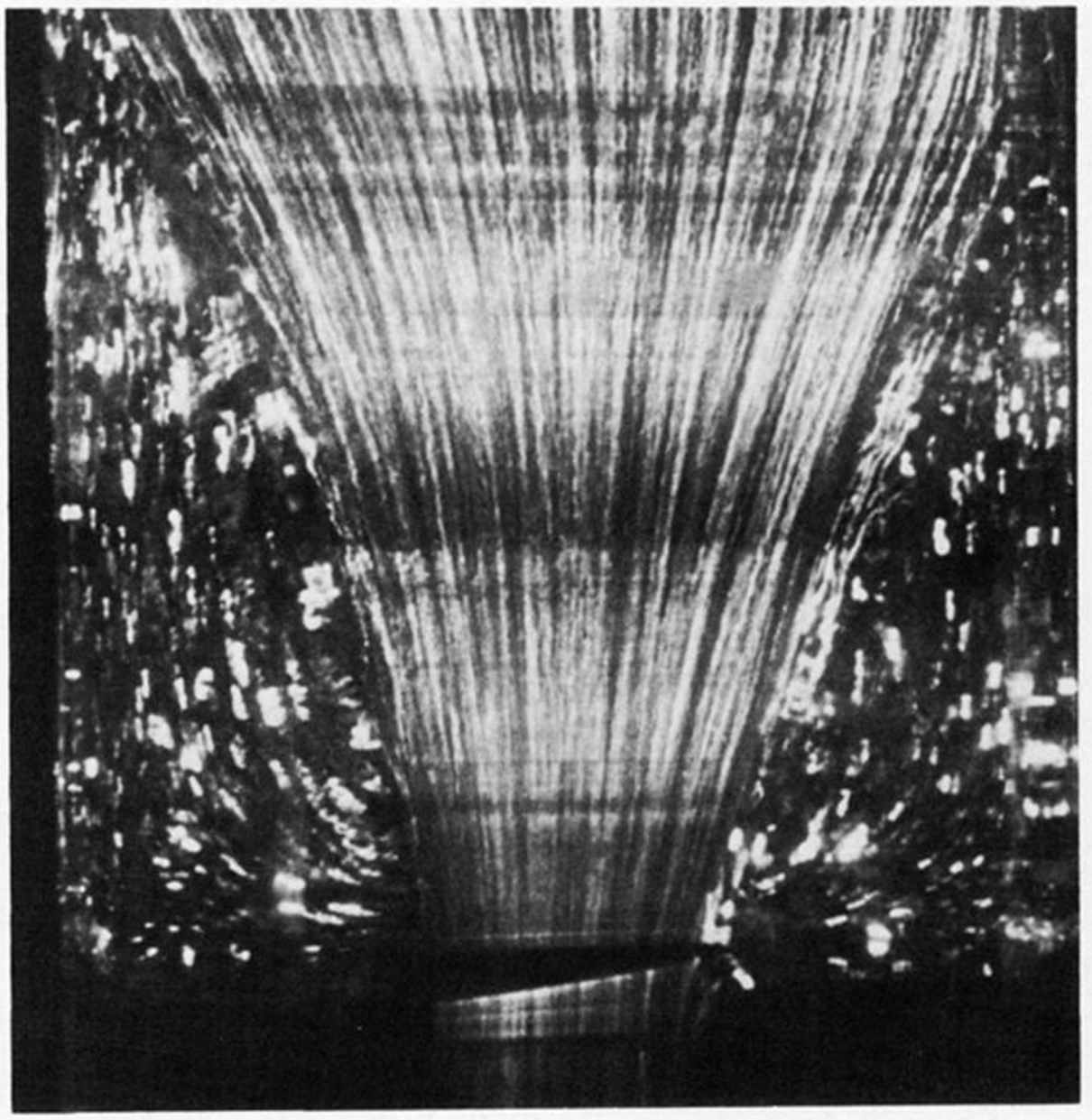

(*b*) geometry 1*e*, $Q = 1.67$ ml s^{-1}

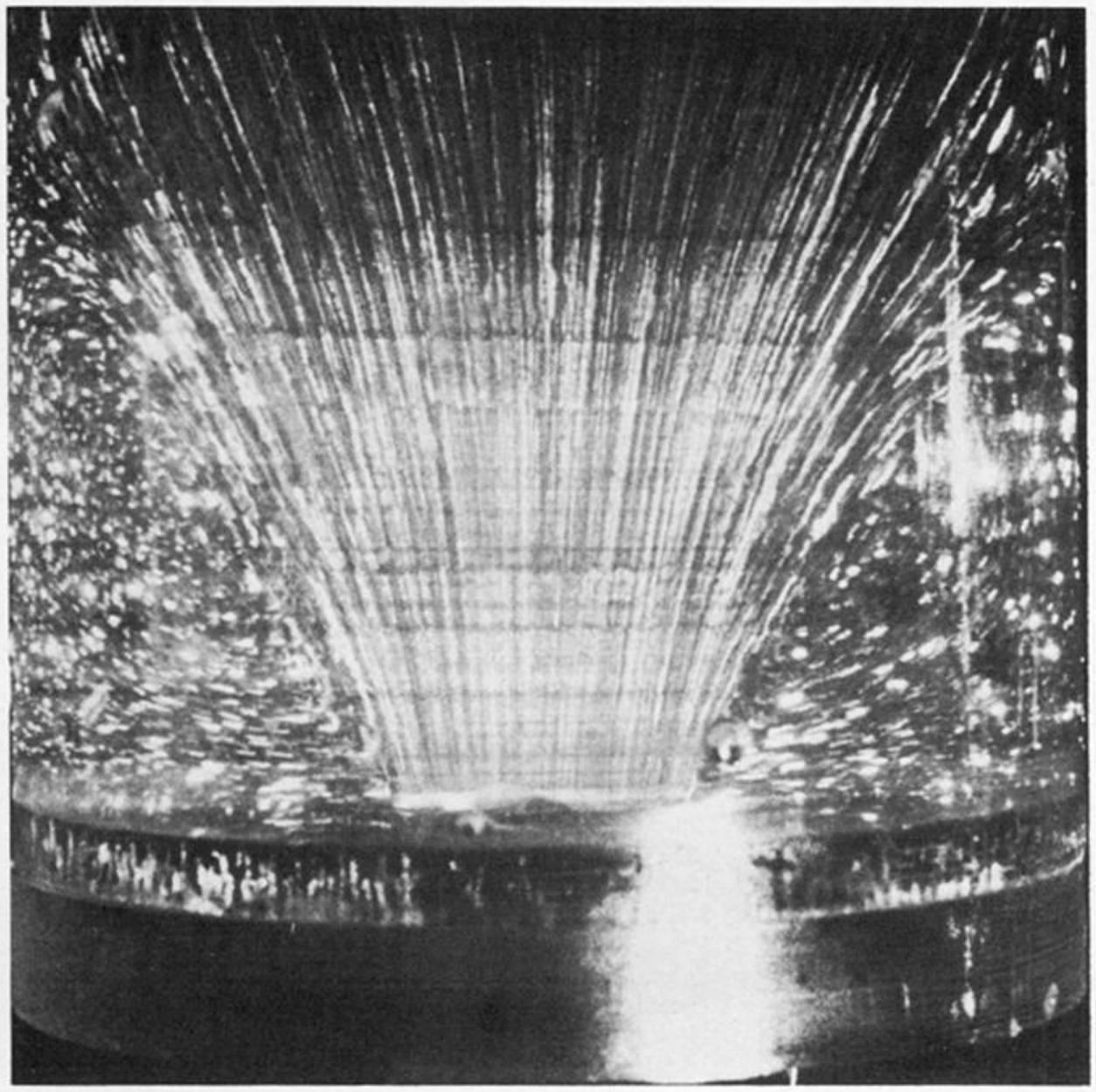

(*c*) geometry 1*g*, $Q = 0.5$ ml s^{-1}

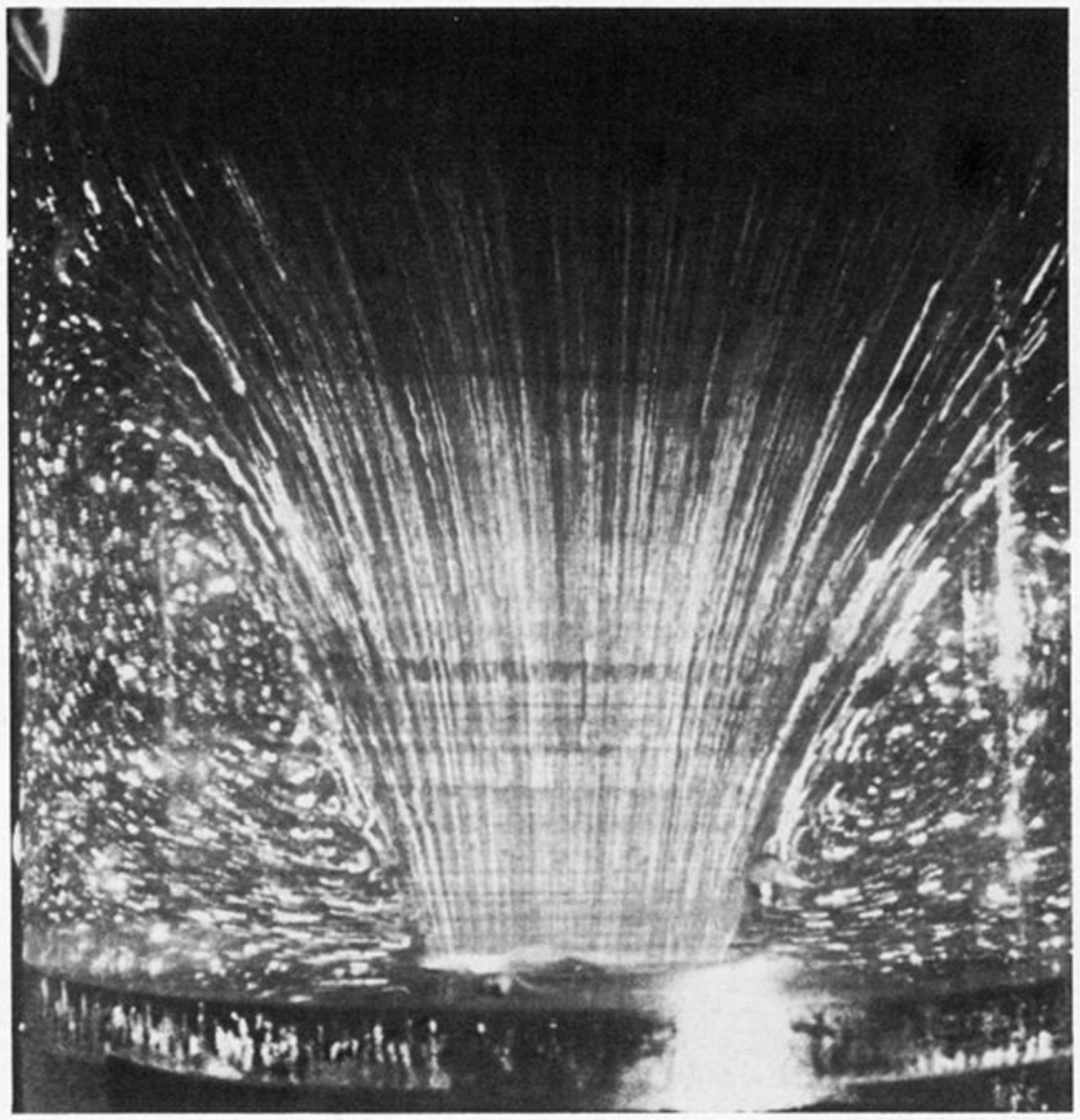

(*d*) geometry 1*g*, $Q = 0.83$ ml s^{-1}

FIGURE 26. Flow of liquid C1 in various contraction geometries: (*a*) geometry (1*d*), flow rate $Q = 0.5$ ml s^{-1}; (*b*) geometry (1*e*), flow rate $Q = 1.67$ ml s^{-1}; (*c*) geometry (1*g*), flow rate $Q = 0.5$ ml s^{-1}; (*d*) geometry (1*g*), flow rate $Q = 0.83$ ml s^{-1}. There is some evidence of camera shake in (*b*).

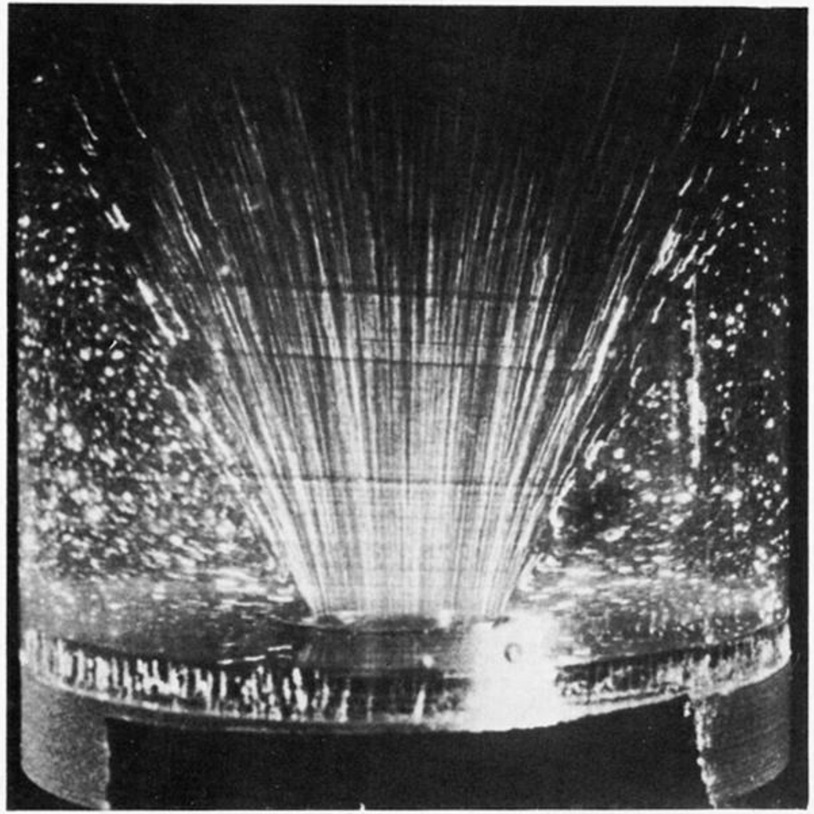

(*a*) $Q = 0.5$ ml s^{-1}

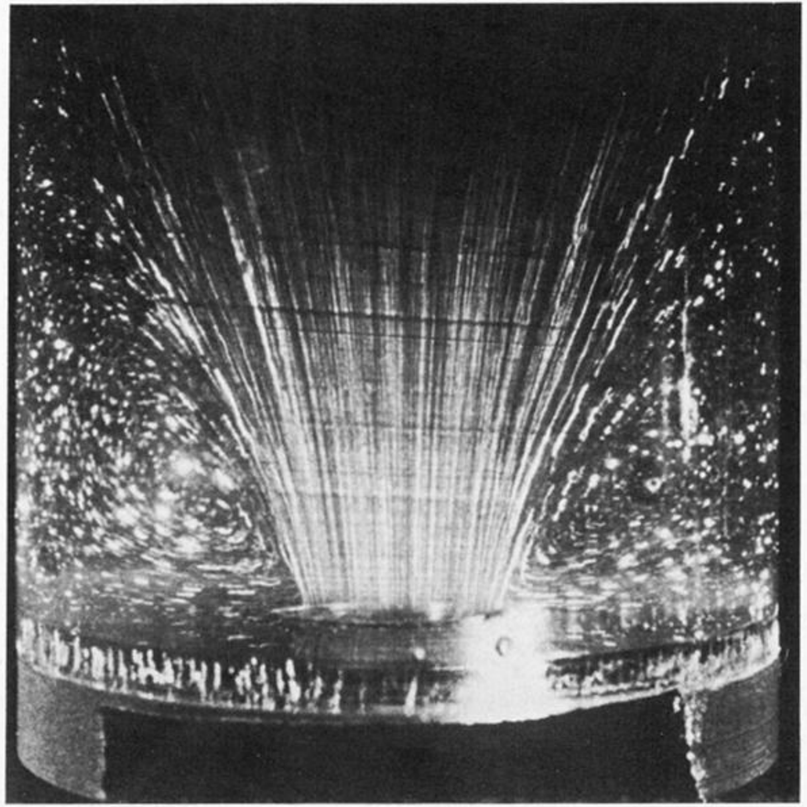

(*b*) $Q = 0.83$ ml s^{-1}

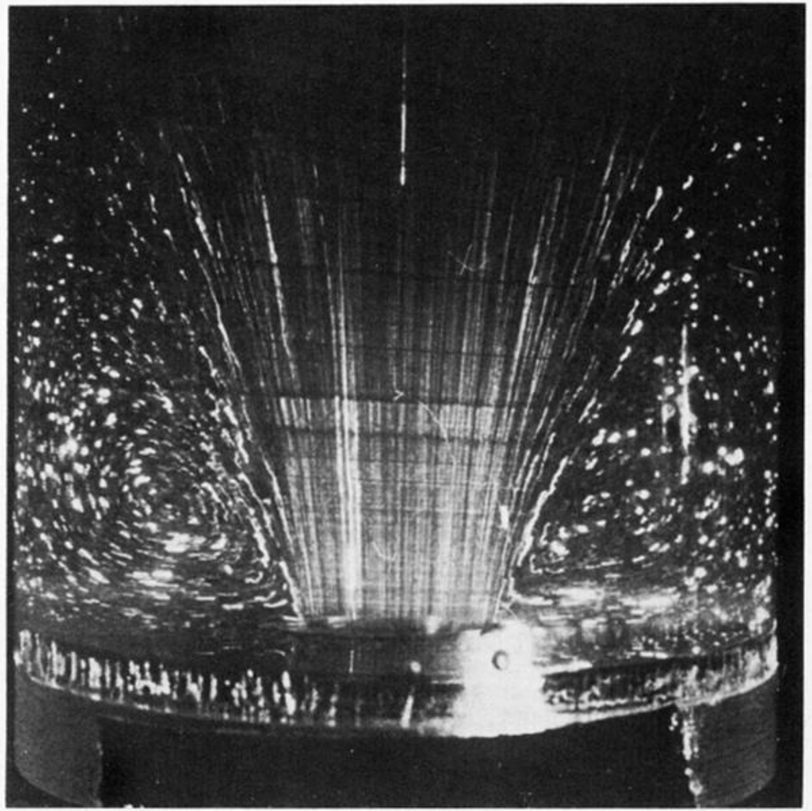

(*c*) $Q = 1.67$ ml s^{-1}

FIGURE 27. Flow of liquid C1 in symmetrical circular contraction geometry (1*f*): (*a*) $Q = 0.5$ ml s^{-1}; (*b*) $Q = 0.83$ ml s^{-1}; (*c*) $Q = 1.67$ ml s^{-1}.